Velocity Field Measurements of a Jet Confined to a Swirling Flow Using Digital Particle Image Velocimetry Cinematography.

by

Federico Frigerio

B.S.E. Mechanical and Aerospace Engineering
Princeton University, 1995

Submitted to the Department of Mechanical Engineering
in Partial Fulfillment of the Requirements for the Degree of
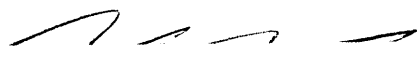Master of Science in Mechanical Engineering

at the

Massachusetts Institute of Technology

June 1997

Signature of Author . . . .
Department of Mechanical Engineering
May 28, 1997

Certified by . . . . : . . . .
Professor Douglas P. Hart
Department of Mechanical Engineering

Accepted by . . . .
Professor Ain A. Sonin
Chairman, Department Committee on Graduate Students
Department of Mechanical Engineering

Velocity Field Measurements of a Jet Confined to a Swirling Flow Using Particle Image Velocimetry Cinematography

by

Federico Frigerio

Abstract

The turbulent velocity and vorticity fields of a jet confined to a swirling flow incorporating a sudden expansion have been obtained by using Digital Particle Image Velocimetry Cinematography (DPIVC). This technique allows the resolution of the instantaneous velocity field of a planar cut in the flow over a long period of time, so that temporal variations can be investigated. DPIVC movies of longitudinal cuts intersecting the tube axis were taken at three successive axial locations, so that a total length of three tube diameters beyond the inlet was visualized. Experiments were performed with secondary Reynolds' numbers ranging from 11,000 to 35,000, with secondary swirl numbers ranging from 0 to 2, and with jet velocity ratios (defined as the velocity ratio of the jet to the secondary flow) ranging from 0 to 20.

The recorded velocity fields and the vorticity fields which were calculated from them indicate the presence of a central recirculation zone driven by a line of azimuthal vorticity spiraling up from the inlet. The strength of this recirculation zone was found to increase with swirl number and was found to decrease and finally disappear completely for a high enough jet velocity ratio. The jet was found to oscillate about the axis for high jet velocity ratios, and the frequency of this phenomena was measured.

Acknowledgments

I would first like to thank my advisor Professor Douglas Hart for his guidance and support during this project. Between 2.670, whose struggles and triumphs were truly character building, and this research project, it has been a real pleasure working with him over these last two years.

I would like to thank my colleagues in the Fluid Mechanics Lab for their help and support. I would especially like to acknowledge the assistance given by Hugo Ayala, Youssef Marzouk and Hayden Huang; the completion of this thesis would not have been possible without their excellent work and good advice. Furthermore, their good cheer helped turn the "Pit of Despair" into a happy-go-lucky place.

I would like to thank Richard Fenner and Norm Berube in the Pappalardo Lab, as well as Kevin Baron, Fred Cote and Gerry Wentworth in the Lab for Manufacturing and Productivity, for all their help and advice in the re-machining of the swirler. Their expertise and kindness were instrumental in the completion of the apparatus.

I would like to thank my family for all their love and encouragement. Their confidence in me helped me through the difficult times, and their love helped me remember all that is truly important in life.

Finally, I would like to dedicate this thesis to Dr. Anne Baker and to Meghan Baker. They have been inspirational role models for me over this past year, and I will carry with me always their strength, thoughtfulness, and love.

Table of Contents

List of Figures

List of Tables

CHAPTER 1
Introduction

1.1 Importance of Swirling Flows and Motivation

Swirling flows have long been studied as a way to improve combustion efficiency and emission characteristics in industrial burners and gas turbine engines. Swirl stabilizes combustion by creating a recirculation zone in which fuel/air mixing is increased. Certain swirl strengths have been found to reduce harmful NOx emissions by shortening the flame length, thereby reducing the residence time of products of reaction within the high temperature regions of the flow (cf. Takagi and Okamoto [1]). Conversely, it has also been found that too much swirl can actually increase NOx emissions by making the products follow such a tightly wound helical path that their residence time within the hottest part of the flow is actually increased (Gupta et al. [2]). These findings suggest that for a given combustion regime, there exists an optimum level of swirl which will minimize NOx production.

Current knowledge of both the combustion and fluid dynamic processes involved in swirling combustors is too limited to allow designers to reliably predict emission characteristics without building and testing expensive prototypes. Though computer models aimed at aiding the designer are improving constantly, present computational limits force these codes to rely on simplified fluid dynamics and combustion models (such as the k-e model for turbulence) which require the use of constants which can only be obtained from actual experiments.

Part of the motivation behind this research is to obtain further velocity measurements in non-reacting, swirling flows to help calibrate these computer models. More importantly, however, very little data describing the temporal and non-axisymmetric characteristics of these types of flows has been compiled, since most experimental investigations have relied on time-averaged velocity measurement techniques. The use of Digital Particle Image Velocimetry Cinematography in the experiments reported here is a distinct innovation since this measurement technique allows the determination of instantaneous two dimensional velocity fields over a prolonged period of time.

8

1.2 Physical Insights into the Onset of Vortex Breakdown

The creation of the recirculation region is a vortex breakdown phenomena, a complex three-dimensional and unsteady flow which was first discovered in the leading edge vortices trailing from delta wings (Peckham and Atkinson [3]). As described by Althaus et al. [4], a good understanding of this phenomena can be gained by examining its development in a simplified flow field: an incompressible, axisymmetric, inviscid swirling flow confined in a tube. In the pre-breakdown region of such a flow, the axial, radial and circumferential components of the momentum equation in cylindrical coordinates are:

$$\frac{\partial u}{\partial t} + (\vec{v} \cdot \nabla)u = -\frac{1}{\rho}\frac{\partial p}{\partial z} \tag{1}$$

$$\frac{\partial v}{\partial t} + (\vec{v} \cdot \nabla)v - \frac{w^2}{r} = -\frac{1}{\rho}\frac{\partial p}{\partial r} \tag{2}$$

$$\frac{\partial w}{\partial t} + (\vec{v} \cdot \nabla)w + \frac{vw}{r} = -\frac{1}{\rho r}\frac{\partial p}{\partial \theta} \tag{3}$$

Assuming that the vortex is slender and axi-symmetric, one can state the following:

$$v \ll u, w \tag{4}$$

$$\frac{\partial}{\partial \theta} = 0 \tag{5}$$

Applying these assumptions to equations 1-3 then leads to:

$$\frac{\partial u}{\partial t} + u\frac{\partial u}{\partial z} = -\frac{1}{\rho}\frac{\partial p}{\partial z} \tag{6}$$

$$\frac{\rho w^2}{r} = \frac{\partial p}{\partial r} \tag{7}$$

$$u\frac{\partial w}{\partial z} + v\frac{\partial w}{\partial r} + \frac{vw}{r} = 0 \tag{8}$$

Differentiating (7) with respect to z and integrating with respect to r gives:

$$\frac{\partial p}{\partial z}(z,r) = \frac{\partial p}{\partial z}(z,r \to \infty) - 2\rho\int_{r}^{\infty}\frac{w}{r}\frac{\partial w}{\partial z}dr \tag{9}$$

Meanwhile, equation (8) can be written as:

$$\frac{\partial w}{\partial z} = -\frac{v}{u}\frac{1}{r}\frac{\partial}{\partial r}(rw) \tag{10}$$

and can be replaced into (9) to yield:

$$\frac{\partial p}{\partial z}(z,r) = \frac{\partial p}{\partial z}(z,r \to \infty) + 2\rho \int_r^\infty \frac{w}{r^2} \frac{v}{u} \frac{\partial(rw)}{\partial r} dr \qquad (11)$$

To find the integral in equation (11), one can use a Rankine vortex model defined by:

$$w = k \cdot r, \text{ for } r \le R \qquad (12)$$

$$w = \frac{kR^2}{r}, \text{ for } r \ge R \qquad (13)$$

where R is the characteristic vortex core size, and where $k = \frac{\Gamma_\infty}{2\pi R^2}$. Replacing these values

for the tangential velocity in the integral, one obtains:

$$\int_0^R \frac{w}{r^2} \frac{v}{u} \frac{\partial(rw)}{\partial r} dr = 2k^2 \int_0^R \frac{v}{u} dr \approx 0 \qquad (14)$$

$$\int_R^\infty \frac{w}{r^2} \frac{v}{u} \frac{\partial(rw)}{\partial r} dr = \int_R^\infty \frac{R^4 k}{r^3} \frac{v}{u} \frac{\partial k}{\partial r} dr = 0 \qquad (15)$$

Equation (14) is approximately zero since $v \ll u, w$, and equation (15) is zero since

$k = \frac{\Gamma_\infty}{2\pi R^2}$ is a constant. Therefore,

$$\frac{\partial p}{\partial z}(z,r) = \frac{\partial p}{\partial z}(z,r \to \infty) \qquad (16)$$

Equation (16) shows that the axial pressure gradient at the axis is equal to the far-field axial pressure gradient (i.e.: the pressure gradient at the wall). Replacing this equation into (6) gives:

$$\frac{\partial u}{\partial t} + u\frac{\partial u}{\partial z} = \frac{Du}{Dt} = -\frac{\partial p}{\partial z}(z,r \to \infty) \qquad (17)$$

$$u = u_0 - \frac{\partial p}{\partial z}(z,r \to \infty) \cdot t \qquad (18)$$

These two equations show that a stagnation point will develop in time if a positive pressure gradient is present at the boundary. Once this stagnation point has formed, it will cause the main flow to bend around it causing the radial velocity to increase substantially. The ratio of the radial velocity to the axial velocity is no longer negligible under such conditions,

$$\frac{v}{u} \ne 0 \qquad (19)$$

10

and the integral in (14) can no longer be considered to be zero. Instead, a series expansion of both the axial and radial velocities can be performed to yield:

$$v(z,r) \cdot r = a_0(z) + a_1(z)r + a_2(z)r^2 + \dots$$

$$u(z,r) = b_0(z) + b_1(z)r + b_2(z)r^2 + \dots \qquad (20)$$

From the continuity equation for axisymmetric flows,

$$r\frac{\partial u}{\partial z} + \frac{\partial(rv)}{\partial r} = 0, \qquad (21)$$

one can see that

$$\lim_{r \to 0} \frac{\partial(rv)}{\partial r} = 0 \qquad (22)$$

and this can be used as a boundary condition in the expansion of the radial velocity. The other boundary condition is $v = 0$ at r=0, and the application of these two conditions yields

$$v(z,r) = a_2(z)r$$

(neglecting orders two and higher). For the axial velocity, the boundary conditions at r=0 are $\frac{\partial u}{\partial r} = 0$ and $u = u_0(z)$ and they can be applied to the expansion to yield

$$u(z,r) = u_0 + b_2(z)r^2 \qquad (23)$$

(neglecting orders of three and higher). At the edge of the vortex core, the axial and radial velocities are therefore:

$$u_R = u_0 + b_2(z)R^2$$

$$v_R = a_2(z)R \qquad (24)$$

Replacing these expressions into the integral in (14) yields:

$$\int_0^R \frac{v}{u}dr = \int_0^R \frac{a_2 r}{u_0 + b_2 r^2}dr = \frac{a_2}{2b_2}\ln\left(1 + \frac{R^2}{u_0/b_2}\right)$$

$$\approx \frac{a_2}{2b_2}\frac{R^2}{u_0/b_2} = \frac{1}{2}R\frac{v_R}{u_0} \qquad (25)$$

One can make the approximation that $v_R/u_o \approx v_r/u_r$, and the latter expression can be considered to be the growth rate of the vortex core, dR/dz.

Replacing this relation in (25) allows one to rewrite (11) as

$$\left.\frac{\partial p}{\partial z}\right|_0 = \left.\frac{\partial p}{\partial z}\right|_\infty + \frac{2\rho}{R^3}\left(\frac{\Gamma_\infty}{2\pi}\right)^2 \frac{dR}{dz} \tag{26}$$

Equation (26) states that the pressure gradient along the axis is equal to the pressure gradient along the wall plus a term involving the circulation, the size of the vortex core and the vortex core growth rate [4].

Interestingly, the size of the core has been found to be related to the *Re* of the flow. In fact, Harvey [5] observed that the size of the vortex core is determined by the thickness of the boundary-layer shed from the center body of the swirl apparatus, which is inversely related to the *Re* number of the flow.

As has been mentioned above, the formation of a stagnation point at the axis of the tube leads to radial outflow. If one looks at the flow of a fluid material line initially parallel to the axis, (line A-B in Figure 1.1) one can see that the line is forced to bend outward when it reaches the stagnation point (line A'-B' in Figure 1.1).
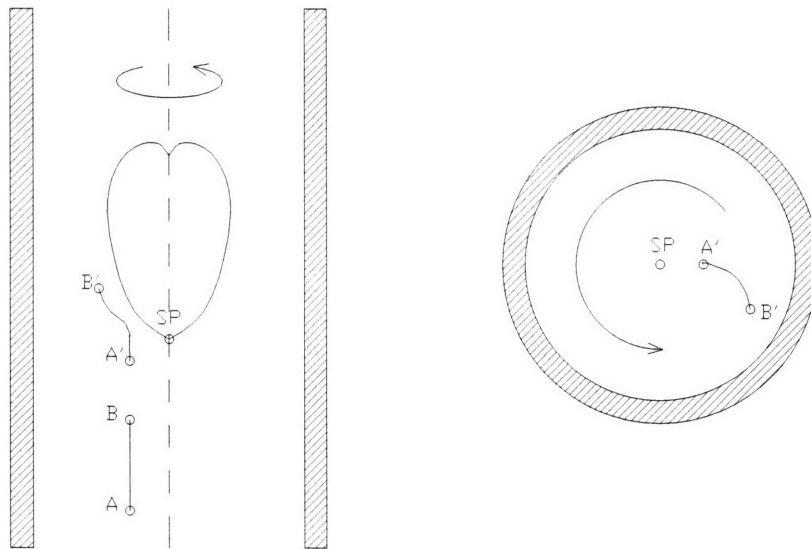
Figure 1.1. Bending of Axial Vorticity due to Stagnation Point. *SP= Stagnation Point*

Because of the conservation of angular momentum, this bending causes the point B' to lag behind A' in the azimuthal plane. Since vorticity is a property which follows material lines, the original axial vorticity of the line A-B is bent along with the fluid line and

12

therefore gains an azimuthal component (see Fig. 1.1). By the Biot-Savart law[1], this azimuthal component of vorticity convects the fluid in the central part of the tube against the main flow direction, thereby increasing the strength of the adverse pressure gradient at the axis. This increase in the adverse pressure gradient at the axis moves the stagnation point upstream and increases the size of the recirculation region (breakdown bubble). A positive feedback loop (first described by Brown and Lopez, 1990 [6]) is set up as the growth of the bubble strengthens the azimuthal component of the vorticity by increasing the deformation of the axial component, which then causes even more fluid to be convected against the main flow direction.

This positive feedback loop can be used to explain the formation and migration upstream of the bubble, but it alone cannot explain the formation of a bubble having a stable size and axial location. A negative feedback loop is therefore necessary to counteract the growth of the bubble. This loop (first described by Althaus et al. [4]) consists in the weakening of the far field adverse pressure gradient by the increased flow velocities found outside the bubble boundaries. More specifically, the growth of the recirculation zone decreases the area through which the main flow can travel, thereby increasing the velocity of the flow near the wall of the tube. This increased velocity directly decreases the adverse pressure gradient at the wall and indirectly decreases the adverse pressure gradient at the axis (see equation (26)). This in turn reduces the size of the bubble and the strength of the azimuthal component of vorticity. Stability of both the axial location and of the radial dimension is achieved when these two opposing feedback loops cancel each other out exactly.

1.3 Previous Experimental Investigations

The first visualizations of vortex breakdown were performed in low Re, incompressible pipe flow by Harvey [5], who found that increasing the amount of swirl in the flow would cause a transition from a standard Burger's vortex to a bubble type recirculation breakdown. By increasing the swirl even further, Harvey found that the bubble breakdown turned into a columnar vortex flow with a core region characterized by a back-flow along the entire axis of the tube. Later, Sarpkaya [7] described the occurrence of

---

[1] $\vec{U}(\vec{r}) = -\dfrac{1}{4\pi} \displaystyle\int \dfrac{\vec{s} \times \omega(\vec{r}')}{s^3} dV$ where $\vec{s} = \vec{r} - \vec{r}'$.

several different breakdown modes (bubble, spiral, and double helix). He found that all three forms were stable in certain regions of the parameter space defined by Reynolds number and by the circulation number, and that there were also certain bistable regimes under which an apparently spontaneous transition from one form of breakdown to another would occur. Sarpkaya ([8]) also investigated the effect of an adverse pressure gradient on vortex breakdown by using a series of tubes having different divergence angles. These experiments showed that increasing the adverse pressure gradient would allow a certain kind of breakdown to exist at a lower swirl number than normal, or, for a constant swirl number, would allow the same breakdown to move further upstream.

Because the vortex breakdown flow field is extremely sensitive to external disturbances, all early attempts to measure velocity and pressure fields using hot wire probes or Pitot tubes proved to be unsuccessful. In fact, Sarpkaya ([7]) reported that, under certain conditions, the insertion of a probe on the centerline of the tube would actually precipitate a breakdown immediately behind it. These difficulties prevented the extraction of very much quantitative information from vortex breakdown phenomena until Faler and Leibovich [9] used Laser Doppler Anemometry (LDA) to measure time-averaged axial velocities in a bubble type breakdown in a pipe flow having a Re of about 3,000 and a S of 0.4. LDA is a non intrusive measurement method which measures the velocity of seed-particles passing through a small interrogation area defined by the intersection of two laser beams. Several thousand particle velocities are measured in each location and an average value is calculated from them. Using this technique, Faler and Leibovich [9] found that though the external appearance of the breakdown bubble is axisymmetric, the internal structure is highly asymmetric and time-dependent. Their results showed a bubble composed of a two cell structure, with the mean velocities in the inner cell being about a third smaller than those found in the outer cell. The maximum mean velocity found was about 15% of the maximum axial velocity of the upstream flow. These experiments also revealed the occurrence of a spiral breakdown downstream of the main bubble breakdown, followed by the apparition of a regular turbulent wake profile.

In a landmark study, Brücker and Althaus [10] used a quasi three-dimensional technique combining Particle Tracking Velocimetry (PTV) and light sheet scanning to obtain the velocity and vorticity fields of the entire breakdown bubble in a pipe flow having a Re of 840. Their experiments revealed the presence of a single tilted vortex ring

structure in the downstream part of the bubble, with reversed axial velocities as large as the mean flow velocity itself.

Other flows more complex than simple low Re, swirling pipe flows have been investigated in the combustion community. Various simulated gas turbine combustors have been analyzed using LDA techniques to obtain the velocity fields for non-reacting, homogeneous coaxial-jet flows. Habib and Whitelaw [11] performed experiments at a secondary flow Re of 77,000, with a primary to secondary jet velocity ratio of 3, and with a swirl number of 0.23. They were not able to find any flow reversals under these conditions, but they did report a decrease of the axial velocity several tube diameters downstream of the jet. Vu and Gouldin [12] described the formation of a recirculation bubble driven by a single toroid of azimuthal vorticity in co- and counter-swirling flows having a Re of about 250,000 and a swirl number of less than 1.0 (see Figure 1.2). Gouldin, Depsky and Lee [13] investigated the effect of swirling both the primary
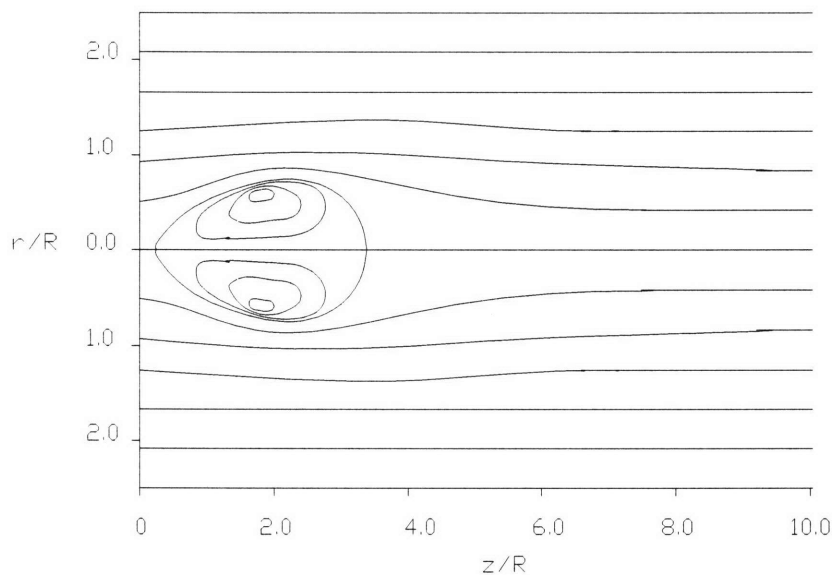
Figure 1.2. Schematic of Stream Function Contours Obtained by Vu and Gouldin [12]. R is the primary jet radius.

and secondary jets under a secondary Re number regime of 75,000, and found recirculation zones occurring for counterswirl conditions only. (Si=0.5; So=+-0.56). Ramos and Somer [14], on the other hand, showed that recirculation can occur under both co- and counterswirl conditions, and also described a bubble shaped recirculation zone being driven by a single toroid of azimuthal vorticity. Their experiments were performed in the ranges Re~10^4-10^5, S~0.6. The researchers So, Ahmed and Mongia [15] performed experiments in air at a Re of 55,000 and with a secondary swirl number of 2.25 for several different primary to secondary jet velocity ratios. In the absence of any flow through the central jet, they discovered the presence of two recirculation zones on the axis. With the central jet turned on, they found that the axial momentum addition from the jet caused these recirculation regions to disappear.

1.4 Previous Numerical Simulations

Until recently, numerical simulations of the vortex breakdown phenomena were restricted to axisymmetric, steady, incompressible flows (Grabowski and Berger [16]). These early simulations showed the creation of recirculation zones, but led to the conclusion that the numerical prediction of vortex breakdown requires the solution of the complete Navier-Stokes equations for time-dependent, three-dimensional flow. These complex simulations were first performed by Spall and Gatski (1987 [17]), Hänel and Breuer [18], and Spall et al. (1990 [19]), and showed the time dependent evolution of the bubble interior for a flow having a Reynolds number, Re=200.

Numerical investigations aimed at making engineering predictions of both the fluid dynamics and the temperature and emission characteristics of actual combustors have also been performed (Haynes [20]). Due to the enormity of the computational problem, however, the simulations of these high Re reacting flows have been forced to rely on turbulence and reduced chemical kinetics models in order to be practical.

1.5 Experiments Reported Here:

In an attempt to learn more about the temporal effects occurring in swirling flows, the experiments reported here were performed using Digital Particle Image Velocimetry Cinematography (DPIVC). This is a new measuring technique which incorporates the

principles of Digital Particle Image Velocimetry (Adrian 1991 [21]) into a motion picture format. Like DPIV, DPIVC is a means of instantaneously and non-invasively measuring velocities in an entire plane within a flow field seeded with tracer particles; unlike DPIV, however, DPIVC also allows the investigator to analyze the flow continuously over a long period of time, so that the flow's time dependent effects can be resolved. Both DPIVC and DPIV are in sharp contrast to LDA, where only the time averaged velocity at one particular point in the flow can be measured.

Typically, DPIVC and DPIV utilize either cross-correlation or auto-correlation methods. Both methods involve double-pulsing a laser light sheet to illuminate tracer particles in the flow. In cross-correlation, the two exposures of the tracer particles are recorded on two successive frames; in auto-correlation, the two exposures are recorded on the same frame. The minimum time difference between the exposures using the cross correlation technique is limited by the frame rate of the camera (typically 30 Hz), and this interval is often too large to correlate successive images taken from high speed flows (Willert and Gharib 1991 [22]). The use of auto correlation techniques, on the other hand, is limited only by the pulse rate of the laser (which is often on the order of microseconds). Though auto correlation allows much shorter time intervals between exposures, directional ambiguities are introduced into the analysis since it is impossible to tell the order of the exposures from an auto correlated image.

Because the direction of the recorded speeds are very important in characterizing the recirculation region of a vortex breakdown phenomena, only cross correlation techniques were used in the experiments reported in this thesis.

CHAPTER 2

Experimental Setup

2.1 Swirl Chamber

A very detailed description of the theoretical considerations that went into the design of the swirl chamber can be found in Danitz's thesis [23]. The following section gives a brief description of the swirl chamber, as well as a more detailed account of the modifications which were made to it by the author.

The main components of the swirl chamber (see Figure 2.1) are a toroid shaped settling chamber, an array of swirl vanes, an aluminum converging nozzle step insert, an acrylic test section, and a primary jet stainless steel tube. Water was used as the working fluid for both the primary and secondary flows.

The secondary water flow was pumped into the toroidal settling chamber, where any vortical disturbances imparted to the flow by the 5000 W pump were damped out. To clean up the secondary flow further, it was passed through a pair of flow straighteners before entering the swirl compartment. The first straightener consisted of 500 half-inch holes drilled along the periphery of the central rib; the second straightener consisted of a gauze pad annulus located just ahead of the swirl vanes. This gauze pad also served as a filter for any large particles or debris in the flow.

The swirl compartment consisted of a circular array of 36 swirl vanes evenly spaced on a 17 inch diameter circle in the azimuthal plane. The amount of swirl imparted to the secondary flow was controlled by adjusting the angle of the guide vanes, which had a rectangular cross section and measured 2 in. x 4 in. x 1/8 in. The secondary flow's swirl number was varied by adjusting the angle of each swirl vane. This involved accessing the swirl compartment by removing the test section and the top aluminum and PVC plates from the settling chamber. The required angle was marked onto the PVC plate supporting the vanes using a Magic Marker, and these marks were used to align the swirl vanes. The swirl numbers that could be achieved by this setup ranged from 0 to 3.5.

To prevent separation ahead of the test section, the shapes of the aluminum nozzle and of the bell shaped swirl cone were selected so that the secondary flow was always under a state of axial acceleration. At the same time, the sudden expansion at the end of the
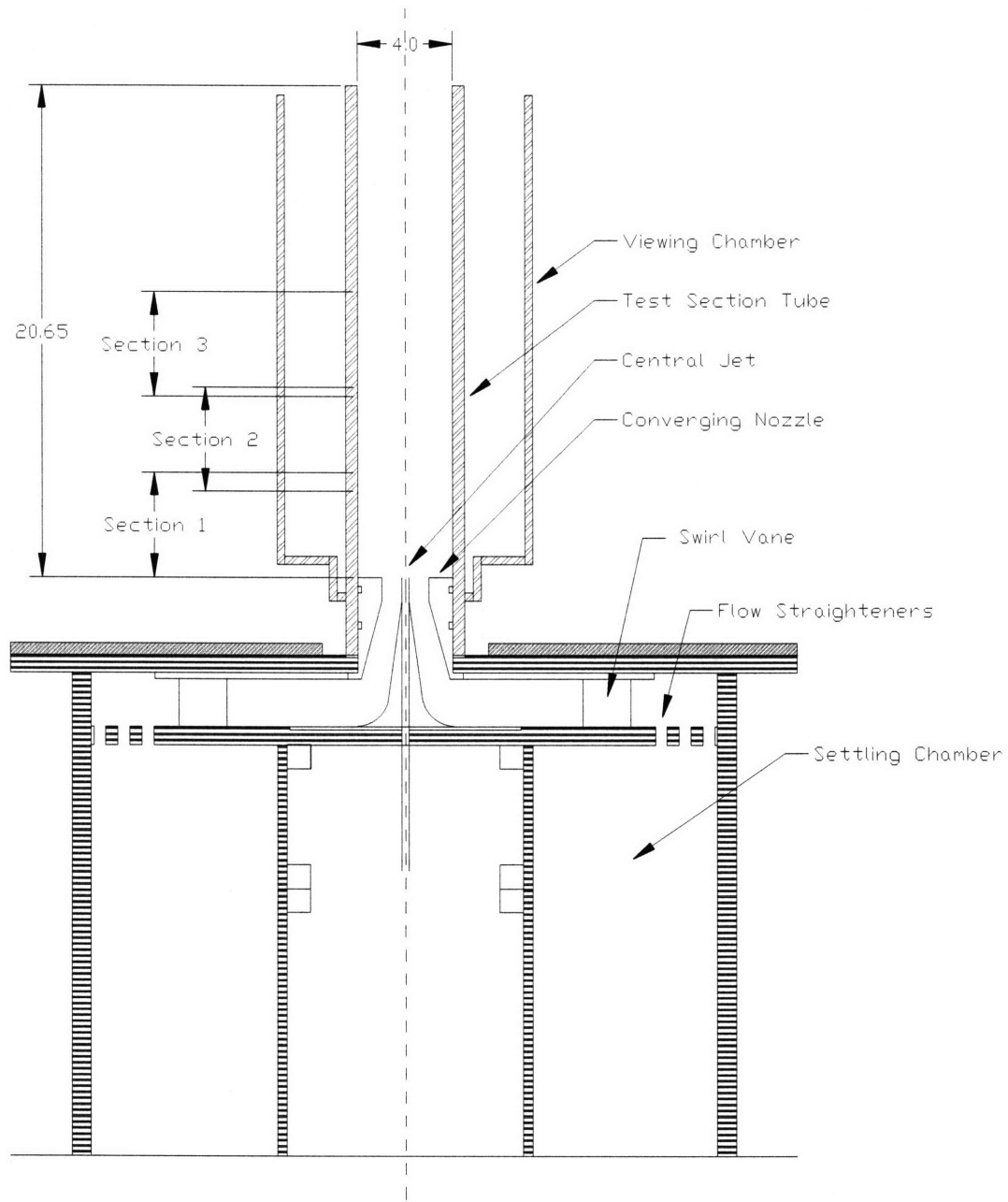
Figure 2.1. Cross Section of Swirler Apparatus.

aluminum nozzle was included to help precipitate the occurrence of vortex breakdown. This idea is based on the fact that a sudden expansion creates a very strong adverse pressure gradient in the flow, and this was shown to be critical to the formation of a breakdown in Section 1.3. This aluminum nozzle provided an expansion ratio of 2.0 between the test section and the incoming flows.

The acrylic test section had an inner diameter of 4 in. and was 24 in. in length. To remove the optical distortion caused by its circular shape, the test section was surrounded by a square acrylic viewing chamber filled with water. The similarity between the index of refraction of water and that of acrylic plastic thus insured that the optical distortion was kept to a minimum.

The water for the primary jet was pumped from the primary flow holding tank through a set of float meters to the .30 in. diameter stainless steel tube located on the axis of the test section. The ratio of the primary and secondary flow velocities was varied by way of the float valve which could produce jet flow rates from 0.75 to 5 gallons per minute (gpm).

The mixed primary and secondary flows traveled downstream from the test section into an elbow joint which incorporated a transparent horizontal porthole at its highest point. This porthole allowed the CCD camera to record images of azimuthal cross sections. Vortices in general and breakdowns in particular have been found to be very sensitive to the downstream flow conditions, and this angled elbow was included to minimize any such disturbances. From the elbow, the flow discharged back into the main holding tank.

The *Re* was varied from one experiment to another by varying the position of the back-flow valve immediately downstream of the test section. This butterfly valve can be rotated to assume several angles and several calibration runs were performed to insure that the achieved flow speeds were repeatable and consistent. The total water flow rate was calculated from pressure transducer readings across a calibrated orifice plate located downstream of the test section, as well as by a set of calibration runs which measured the time rate of change in water level in the main holding tank for each flow setting.

2.2 Modifications Made to the Swirl Chamber:

As was shown in Section 1.3, the amount of swirl (or circulation) imparted to the flow is an extremely important parameter in determining if a certain kind of breakdown will take place. Unfortunately, it was found that the original swirl compartment was not able to impart enough swirl to the secondary flow to precipitate vortex breakdown. In fact, the highest swirl number reported in Danitz's thesis (1995 [28]) was about 0.82, and his LDA velocity measurements showed that a recirculation zone was not present under this condition. A control volume analysis was therefore performed on the swirl compartment
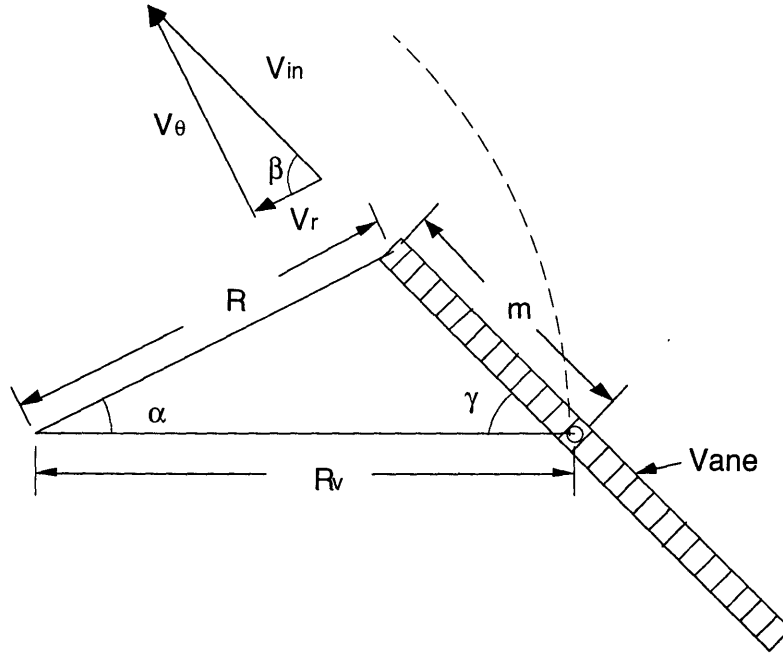
Figure 2.2. Geometry of Swirl Section [24]

in order to find the critical parameters which should be modified to improve its performance.

The first assumption that this analysis makes is that the circulation, Γ, is conserved throughout the swirl compartment. This allows the calculation of the non dimensional circulation number, Ω, based upon three parameters: the circulation in the swirl compartment of the apparatus, Γ, the average axial velocity in the test section, $\overline{u}$, and the diameter of the test section, D:

$$\Omega \equiv \frac{\Gamma}{\overline{u}D} \tag{27}$$

Looking at Figure 2.2, the volume flow rate through the test section and through the swirl compartment are equal and are given by:

$$Q = \pi \frac{D^2}{4}\overline{u} \tag{28}$$

$$Q = 2\pi R h v_{in} \cos\beta, \tag{29}$$

where h is the height of the swirl compartment, v_{in} is the fluid velocity component parallel to the vane, β is the vane angle, and R is the radius of the vane circle.

21

The tangential velocity of the flow as it passes by a swirl vane is easily calculated from Figure 2.2:

$$v_\theta = v_{in}\sin\beta = \frac{Q}{2\pi Rh}\tan\beta,$$

(30)

The circulation, Γ, in the swirl compartment can therefore be calculated:

$$\Gamma = 2\pi Rv_\theta$$

(31)

and this is equal to the circulation in the test section (as per the assumption made above). With the average axial flow velocity in the test section given by:

$$\bar{u} = \frac{4Q}{\pi D^2}$$

(32)

the circulation number can be calculated:

$$\Omega = \frac{2\pi Rv_\theta}{\bar{u}D} = \frac{2\pi R}{D}\cdot\frac{Q}{2\pi Rh}\tan\beta\cdot\frac{\pi D^2}{4Q}$$

(33)

$$\Omega = \frac{\pi}{4}\frac{D}{h}\tan\beta$$

(34)

Now, from Figure 2.2, the angle β is given by :

$$\beta = \gamma + \alpha$$

(35)

where

$$\alpha = \tan^{-1}\left(\frac{m\sin\gamma}{R_v - m\cos\gamma}\right)$$

(36)

Since the circulation is conserved, it is also given by:

$$\Gamma = \frac{\pi D\bar{v}_{\theta S}}{\bar{u}D} = \frac{\pi\bar{v}_{\theta S}}{\bar{u}}$$

(37)

where $\bar{v}_{\theta S}$ is the average tangential velocity in the test section [24].

Now, to determine the relationship between the circulation number, Ω, and the swirl number, S, one can perform the following calculations:

$$S = \frac{\int_0^{\frac{D}{2}}(v\cdot r)\rho u2\pi rdr}{\frac{D}{2}\int_0^{\frac{D}{2}}u\rho u2\pi rdr} = \frac{\rho\bar{v}_{\theta S}\bar{u}\frac{\pi D^3}{12}}{\rho\bar{u}^2\frac{\pi D^3}{8}} = \frac{2}{3}\frac{\bar{v}_{\theta S}}{\bar{u}}$$

(38)

where $\bar{v}_{\theta S}$ and $\bar{u}$ are respectively the mean tangential and axial velocities in the test section.

22

Combining equations (38), (27) and (37) leads to a final expression for the swirl number:

$$S = \frac{2}{3}\frac{\Omega}{\pi} = \frac{1}{6}\frac{D}{h}\tan\left[\gamma + \tan^{-1}\left(\frac{m\sin\gamma}{R_v - m\cos\gamma}\right)\right] \qquad (39)$$

Equation (39) shows that the swirl number is strongly dependent on the diameter of the test section, the height of the swirl vanes, and the angle at which the swirl vanes are set.

Originally, the swirl compartment had the following characteristics: a swirl vane height, h, of 8 inches, a length m equal to 1.25 inches, and a maximum achievable angle γ of 75 degrees. Replacing these dimensions into (39) reveals that the highest swirl number which could be achieved was about 0.72^2, and Danitz [23] reports that no recirculation zone was found at this value.

It was therefore decided to increase the achievable swirl number by decreasing the vane height by a factor of 4, and by decreasing the length m (which also allowed the maximum swirl angle to be raised to 80 degrees). Based on equation (39), these modifications increased the upper swirl limit to a value of about 3.5.

The reduction of the swirl vane height to 2 inches from 8 inches involved the re-machining of all 36 swirl vanes, as well as the re-machining of the mandrel, the vane cover and the upper flow contour. An extension to the small cylinder was also manufactured so that the 6 inch gap caused by the shortening of the swirl vanes could be breached.

2.3 Laser System and Data Acquisition

A schematic of the entire experimental system can be seen in Fig. 2.3. The illuminating light sheet was produced by a Q-switched, 15 Watt Nd:YAG pulsed laser, frequency doubled to emit visible light at a wavelength of 532 nm[3].

---

[2] The difference between this value and that mentioned by Danitz (1995) is due to the latter's use of a less rigorous swirl number calculation.

[3] A Q switch is a device which can selectively transmit or absorb light within the laser cavity. When the laser is fired, the Q switch is set to absorb light so as to prevent the laser from oscillating. This has the effect of creating a much larger population inversion within the lasing medium than normally necessary for laser action. The Q switch is then triggered to transmit light and stimulated emission quickly drains the laser cavity of its stored energy in a short pulse whose peak power is higher than that produced by normal laser operation.
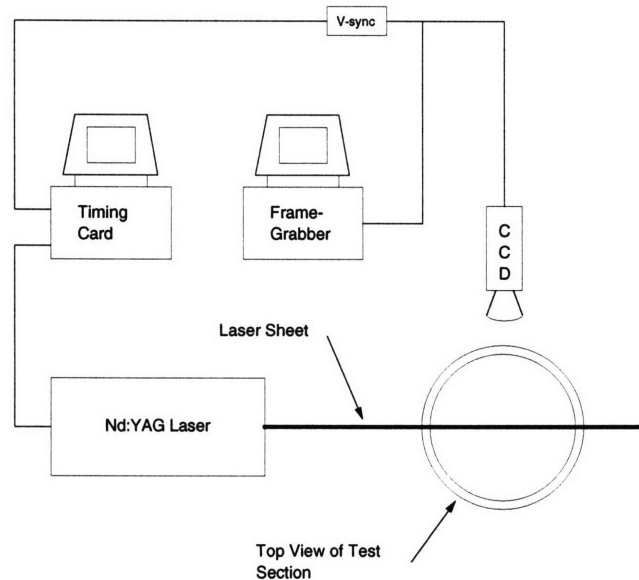
Figure 2.3. Schematic of Experimental Setup.
Imaging of Longitudinal Section is Shown

The Q switch was controlled by a programmable timing card incorporated into an IBM PS2 and could be triggered to create pulse separations as short as 20 micro seconds, though pulse intervals on the order of milliseconds were used in the experiments reported here. The Q switch timing control system was externally triggered to coincide with the occurrence of each laser pulse.

The timing of the laser pulses was controlled by a second programmable timing card in the IBM PS2, which allowed the specification of the laser pulse length as well as the interval between laser pulses. This system was externally triggered by the 30 Hz vertical sync signal isolated from the CCD camera by way of a VS-40 chip. This setup insured that the laser pulses always fell within the camera's active frames. A more detailed description of the circuitry of this system can be found in Marzouk's thesis [25].

Two timing patterns were used in the experiments to obtain closely spaced cross-correlating images. The first method was used in the investigation of high speed flows and involved firing a single 1400 microsecond laser pulse and Q-switching it twice. The 1400 microsecond laser pulse was timed so as to straddle the end of the first video frame and the beginning of the second video frame, and the first and second Q-switch pulses were timed to occur at the end of the first video frame and at the beginning of the second video frame, respectively. The second method was used to investigate slower flows and involved firing

24

two separate 0.5 ms laser pulses and Q-switching each of them as they ended. The first laser pulse was timed to occur near the end of the first frame, and the second pulse was timed to occur four or six milliseconds later, at the beginning of the second frame. It should be noted that both these timing schemes allowed a velocity field sampling rate of 15 Hz.

The laser beam was shone through a cylindrical lens to produce a 10mm thick light sheet which could be oriented vertically to obtain longitudinal cross sections or horizontally to obtain azimuthal cross sections. In order to visualize three successive sections of the tube, the laser was raised and lowered in the z-direction by way of mechanical rails. The spherical particles used to seed the flow were manufactured by the authors out of polyester resin, and ranged in size from 45 to 150 microns. The particles were made fluorescent by the incorporation of Rhodamine 6G dye, which has a maximum absorbtance at 524 nm and a maximum fluorescence at 555nm. A Pulnix TM9701 CCD black and white camera equipped with a 550 nm high-pass optical filter was used to record the 512x480 pixel images. The filter was used to isolate the light emitted from the particles from the background laser light and from the intense glare of the test section walls. This setup produced high contrast images with very good signal to noise ratios.

The DPIVC movies which were taken by the CCD camera were stored in an Apple Macintosh computer equipped with a frame grabbing card, and were subsequently correlated by a commercial program obtained from TSI Inc. The length of the DPIVC movies was limited to 90 frames because of the computer's RAM memory restrictions. In the future, the RAM memory restriction will be avoided by processing the raw images in real time and saving the compressed velocity vector files directly to hard disk. The high processing speeds required to correlate images at 15 Hz will be achieved by using such novel techniques as sparse image array correlation. A detailed description of this technique is given by Hart [26].

2.4 DPIVC Considerations:

Just as in the analysis of DPIV images, DPIVC images are processed by correlating the light intensity of the particle images from the first exposure to the light intensity of the particles in the second exposure. The image processing algorithm divides the image into many small interrogation areas and a correlation table including all possible

combinations of Δi and Δj displacements is set up for each one of these areas. The displacement with the largest correlation value is then chosen as the representative displacement for that entire section [26]. This correlation peak is found by comparing pixel by pixel light intensities in the displacement correlation window using either the statistical correlation function:

$$\Phi^S_{\Delta i,\Delta j} = \frac{\sum_{m=1}^{M}\sum_{n=1}^{N}\left[I_{m+\Delta i,n+\Delta j}\cdot I_{m,n}\right]}{\sqrt{\sum_{m=1}^{M}\sum_{n=1}^{N}I^2_{m,n}}\cdot\sqrt{\sum_{m=1}^{M}\sum_{n=1}^{N}I^2_{m+\Delta i,n+\Delta j}}} \tag{40}$$

or the error correlation function:

$$\Phi^e_{\Delta i,\Delta j} = \frac{\sum_{m=1}^{M}\sum_{n=1}^{N}\left[I_{m,n}+I_{m+\Delta i,n+\Delta j}-\left|I_{m,n}-I_{m+\Delta i,n+\Delta j}\right|\right]}{\sum_{m=1}^{M}\sum_{n=1}^{N}\left[I_{m,n}+I_{m+\Delta i,n+\Delta j}\right]} \tag{41}$$

$$\Phi^e_{\Delta i,\Delta j} = 1 - \frac{\sum_{m=1}^{M}\sum_{n=1}^{N}\left[\left|I_{m,n}-I_{m+\Delta i,n+\Delta j}\right|\right]}{\sum_{m=1}^{M}\sum_{n=1}^{N}\left[I_{m,n}+I_{m+\Delta i,n+\Delta j}\right]} \tag{42}$$

Both these functions amplify any difference in the light intensities and range in value from 1 for a perfect correlation to zero for no correlation at all. The error correlation function does not amplify the difference between light intensities as much as the statistical correlation, but it is much less expensive computationally than the latter [26].

The most important parameters influencing the quality of DPIV and DPIVC images are the physical properties of the tracer particles, their seeding density in the flow, the laser pulse spacing, and the size of the interrogation area.

The physical characteristics of the particles limit the flow scales which can be resolved (Crowe et al. [27]). The particle fluid interaction is described by the Stokes Number:

$$St = \frac{\rho_p d_p^2 U}{18\mu L} \tag{43}$$

where ρ_p and d_p are respectively the density and the diameter of the particle, μ is the viscosity of the fluid, and U and L are the velocity and characteristic length of the flow feature being resolved (i.e.: an eddy). The Stokes number is applicable under Stokes flow

26

conditions and is the ratio of the time it would take for a particle released from rest to achieve 63% of the free stream velocity of a flow to the characteristic time associated with the fluid motion. Particles with Stokes numbers much less than one will tend to follow the fluid, whereas those with Stokes numbers larger than one will be unaffected by the flow. Smaller, lighter particles are therefore able to resolve finer aspects of the flow, but their use is limited by the fact that the light intensity reflected by a particle is proportional to the cube of its diameter (Adrian 1991 [21]). The particle diameter must therefore be small enough to track flow patterns of interest yet must also be large enough to be "seen" by the CCD camera. Experience has shown that the best particle size for experiments in water lies in the 50-100 micron range.

The seeding density of the tracer particles, meanwhile, has a very large effect on the spatial resolution of the measurements (Willert and Gharib 1991 [22]) since the mean particle spacing limits the size of the flow features which can be resolved[4].

The length of the laser pulse spacing determines how far a particle will move in between exposures and thereby influences both the spatial resolution as well as the actual errors in the measurement. If the time interval is too long for a given flow regime, the particle may disappear from the second exposure because high in-plane or normal velocities have moved it out of the interrogation area. Furthermore, a time interval which is too long will also allow particles not present in the first exposure to move into the interrogation area and be seen in the second exposure. Both these effects reduce the number of correlating particle pairs and result in a lower signal to noise ratio. Experience has shown that the pulse interval should not exceed the time required by the flow to traverse a distance corresponding to half of the laser sheet thickness or half of the interrogation area size. Another aspect to consider is the fact that even if the particle does stay in the interrogation area in both frames, the large motions caused by a long pulse space will prevent the resolution of any flow curvature (since PIV is not able to visualize curved trajectories in between frames).

It is important to note that the laser pulse spacing has a lower limit, since the relative error increases as the distance traveled by the particles decreases. PIV can locate particle images to resolutions of about .1 pixels by interpolating the exact location of a

---

[4] Experiments using auto correlation techniques encounter a resolution limit when the seeding density is so high that the processing algorithm can no longer distinguish individual particles. This problem does not occur with cross correlation until much higher densities.

particle's center, so acceptable error levels (2% or less) can be achieved if the particles move by at least 5 pixels from one frame to the next.

The size of the interrogation areas also has an effect on spatial resolution and on measurement error. Only one average velocity is calculated for each area, so that the smallest possible interrogation areas should be used. An improvement in resolution is achieved by overlapping the interrogation areas (Willert and Gharib 1991 [22]). Having a small interrogation area is particularly important when investigating flows undergoing rotation, shear or expansion. The velocity field of such flows will vary substantially across the interrogation area if the latter is too large. This will result in a broadening of the velocity correlation distribution, or even in the formation of a number of peaks within that distribution, so that the picking of one distinct velocity value becomes difficult. An example of this effect can be found in the flow investigated in this report. In fact, if one looks at the high shear region surrounding the primary jet as it exits from the stainless steel tube, it can easily see that one side of an interrogation area might contain velocities several times larger than those found on the other side of the area. These substantial differences will obviously lead to a large systematic error.

It is important to note that the particle density, laser pulse spacing and the interrogation window size all have a strong influence on each other. For instance, there is a limit to how small the interrogation area can be made without increasing the seeding density since there must be enough particle pairs inside the sampling area to assure that the correlation peak representing the true velocity is not drowned out by random noise. This noise can be caused by stray light reflections or, if the laser pulse spacing is not short enough, by particles appearing and disappearing in between frames.

CHAPTER 3

Manufacture of Tracer Particles

As was discussed above, the tracer particles used in DPIVC applications must meet very specific size, shape, density, and fluorescence requirements. Because of this complexity, the few commercial manufacturers who make these particles charge as much as $250.00 per gram. Since a typical experiment in the swirl chamber requires about 250 g of particles, and since most of these are thrown away when the apparatus is disassembled to modify the swirl vane angle, it was quickly decided that the acquisition of such particles was not economically feasible. A significant effort was therefore put into the in-house manufacture of high quality tracer particles.

The general approach used to manufacture the particles was obtained from Frish and Webb [28], who used methylmethacrylate monomer as the particle material. This approach relies on the fact that the surface tension properties of the monomer make the plastic form spherical beads when it is poured into water. The addition of a catalyst then links the liquid monomer chains into solid plastic, and the use of anti-emulsants (ammonium thiocyanate and polyvinylalcohol) prevents the beads from amalgamating into each other.

Polyester resin[5] was used to make the particles used in this research. Heat was used to accelerate the hardening of the plastic, and this reduced the curing time from 5 days to less than one day. The sizing of the particles was more accurately controlled by using both a magnetic stirrer and the cavitation effects created by an ultrasound generator to shear and "hammer" apart the larger particles. The speed setting of the stirrer and the power level and total usage time of the sonicator were varied to produce the desired particle size distributions.

Once the process of reliably manufacturing spherical plastic particles had been ironed out, it was discovered that the incorporation of Rhodamine 6G dye into the plastic was an extremely problematic operation. This became apparent when the first batch of dyed particles was used in the swirl chamber, as the water clouded up 8-12 hours after the particles had been introduced. This cloudiness reduced the sharpness of the particle images and made it impossible to correlate them. Eventually, it was determined that the cause of

---

[5] Polyester has a specific gravity between 1.0 and 1.1, and is therefore almost neutrally buoyant.

this problem was the diffusion of the dye out of the particles and into the surrounding water.

An attempt was made to circumvent this problem by replacing the polyester particles with glass micro-spheres coated with dye-impregnated shellac [40 Hart Communication]. The use of shellac was motivated by the fact that it is impregnable to water, and might have therefore created a more secure barrier to the diffusion of the dye. Unfortunately, this approach proved to be very difficult as the shellac tended to amalgamate the micro balloons into large globs, and since the number of microspheres which actually became coated was extremely small.

A slightly more successful approach consisted in trying to form particles from the pure shellac itself. This involved pouring shellac into the same stirred solution of ammonium thiocyanate and polyvinyl alcohol used to make the polyester particles. Once the addition of the shellac was completed, the solution was heated up to a temperature of 78C at which point the alcohol solvent in shellac boiled away, leaving solid spheres behind. This technique did produce some high quality spherical particles, but most of the shellac actually ended up as large useless globs. In fact, the particle yield per batch was so small that the process was deemed impractical.

Finally, an attempt was made to reduce the diffusion rate of the dye through the original polyester particles by reducing the plastic's dye concentration. The dye-rich particles were "bleached" by immersing them in alcohol, which is a more powerful rhodamine solvent than water. Once the particle color was reduced from a bright red to a light pink, it was found that particles placed in water no longer leaked any significant amount of dye. Subsequent particle batches were therefore made using very little dye to begin with, but were still "washed" in alcohol when they were finished to remove any loose dye present on the particles' surface.

The experience gained from these and other experimental trials led to the development of the following particle-making procedure:

- 2 g of polyvinyl alcohol, 1 g of ammonium thiocyanate and 2 g of NaCl are dissolved in 1.8 L of distilled water in a 2000 mL beaker
- 250 mL of polyester resin (casting resin) is poured into a second 2000 mL beaker, and .75 g of Rhodamine 6G is stirred into it

- 20 mL of catalyst is stirred into the resin, and the PVA, ammonium thiocyanate and NaCl solution is quickly poured in thereafter
- the complete mixture is stirred using a magnetic stirrer spinning at full speed
- the mixture is sonicated for about 3 minutes at full power
- with the stirrer still spinning, the mixture is heated to 70 C and is then allowed to cool down (this heating/cooling process is repeated 3 times)
- the mixture is stirred for 5-10 hours

At this point, the particles should be cured and are ready to be separated by size:
- the beaker of particles is poured through a 45 micron sieve into a bucket (tap water is used to help drive the smaller particles through the sieve)
- the liquid in the bucket (containing smaller particles and the chemical residues) is poured into plastic jugs which are disposed of through the Chemical Hygiene Office
- to remove the oversized spheres, the particles remaining in the 45 micron sieve are passed through a 200 micron sieve into a (second) bucket, and they are then transferred to a beaker
- denatured alcohol is added to the particle suspension, and the mixture is stirred for 10-12 hours
- the particles are then re-filtered several times using the 45 micron sieve to remove all traces of alcohol and excess dye

At this point, the particles are ready for use and should be placed in a beaker full of water for storage.

Following this manufacturing procedure gave a useful particle yield of about 30%-40% by volume of plastic.

CHAPTER 4

Experimental Procedures

4.1 Flow Parameters

The three flow parameters which were varied during the course of the experiments were the secondary flow's Reynolds number, Re, the secondary flow's swirl number, S, and the ratio of the primary jet velocity to the secondary flow velocity, ϕ. Each run consisted in setting up the swirl chamber to achieve a certain swirl and Reynolds' number and in taking DPIVC movies of the flow for various values of ϕ.

4.1.1 Set 1: High Reynolds' Number and High Swirl Number; Re=34,000, S=2.0

This first set of experiments' secondary flow had an average axial velocity of about .34 m/s and an average tangential velocity of about .45 m/s. Four primary jet injection rates were analyzed: 0 gallons per minute (gpm), 1gpm, 3gpm, and 5gpm. These flow rates corresponded to ϕ=4.0, ϕ=12,0, and ϕ=20.0. The time interval between the laser sheet pulses was set to 800 ms for these experiments, so that a particles' average axial displacement in between correlating frames would be about .027 cm. With the 10 cm diameter of the test section being spanned by about 400 pixels, this axial displacement corresponded to about 1.1 pixels. The average tangential particle displacement was about .04 cm in between correlating frames, which is significantly less than the laser sheet thickness of 1.0 cm.

Due to the camera's 30 Hz frame rate, the particle's axial displacement in between correlating frame pairs (which were sampled at 15 Hz) was about 90 pixels and the tangential displacement was about 3.0 cm. Furthermore, the flow made 3 complete revolutions about the axis during the 3 second movie.

4.1.2 Set 2: High Reynolds' Number and Low Swirl Number; Re=35,000, S=0.5

This set of experiments' secondary flow also had an average axial velocity of about .35 m/s but had an average tangential velocity of about .12 m/s. Four primary jet injection rates were analyzed: 0 gpm, 1gpm, 3gpm, and 5gpm. These flow rates corresponded to ϕ=3.9, ϕ=11.6, and ϕ=19.3. The time interval between the laser sheet pulses was set to

800 ms for these experiments, so that a particle's average axial displacement would be about .03 cm, or about 1.2 pixels. The average tangential displacement was about .01 cm, which is significantly less than the laser sheet thickness of 1.0 cm.

Due to 15 Hz sampling rate, the particle's axial displacement in between correlating frame pairs was about 100 pixels and the tangential displacement was about .83 cm. Furthermore, the flow made 1 complete revolution about the axis during the 3 second movie.

4.1.3 Set 3: Low Reynolds' Number and Low Swirl Number; Re=11,000, S=0.5

This set of experiments' secondary flow had an average axial velocity of about .10 m/s and had an average tangential velocity of about .03 m/s. Two primary jet injection rates were analyzed: 0 gpm, and 0.7 gpm. These flow rates corresponded to velocity ratios of $\phi=0$ and $\phi=9.5$. The time interval between the laser sheet pulses was set to 4 ms for the first axial location, and to 6 ms for the second and third axial positions. These time intervals resulted in the particles having an average axial displacement of .04 cm (1.6 pixels) in the first section and .06 cm (2.4 pixels) in the second and third sections. The average tangential displacement in between individual frames was about .01 cm in the first section and .02 cm in the second and third sections, which is significantly less than the laser sheet thickness of .06 cm.

Due to 15 Hz sampling rate, the particle's axial displacement in between correlating frame pairs was about 27 pixels and the tangential displacement was about .17 cm. Furthermore, the flow made one third of a revolution about the axis during the 3 second movie.

4.2 Swirler Preparation
4.2.1 Tracer Particle Seeding Density

The amount of particles needed to seed the flow adequately was arrived at by trial and error. Various test images were filmed to determine the effect of particle seeding density on the quality of the correlated velocity fields. This series of tests showed that using a concentration of about 200 mL of (settled) particles per cubic meter of water produced images which could be correlated very well.

4.2.2 Alignment of Laser Sheet and Swirler

Before each run, several checks were performed on the swirl chamber and laser apparatus to insure that the laser sheet and the test section tube were oriented correctly. The test section tube was checked to see if it was perfectly vertical, while the laser sheet was checked to make sure that it was perfectly horizontal (for the azimuthal visualizations) or perfectly vertical (for the longitudinal visualizations) across the test section along the tube's axis. The orientation of the laser sheet and of the test section tube was checked by aligning them with a bubble level. If longitudinal visualizations were to be performed, the position of the vertical laser sheet was also checked to make sure that it crossed the tube at its axis. This was done by setting up the CCD camera above the top porthole so that it could record azimuthal cross sections of the tube. The laser was then pulsed and the location where the laser sheet cut through the tube was recorded. The position of the laser sheet was adjusted until it cut across the test section directly above the primary jet tube. This was done by varying the voltage going to the galvanometers which controlled the angle of the guiding mirrors in the laser.

4.3 Procedures Used to Visualize Azimuthal Sections

To obtain the azimuthal images of the flow, the CCD camera was mounted vertically above the porthole, and the laser's semi cylindrical lens was rotated so as to produce horizontal light sheets. The laser sheet could be raised vertically by raising the rail-mounted laser or by adjusting a pair of external mirrors which had been set up in a periscope geometry. The lens was focused on the laser sheet by firing the laser and observing the flickering images in real time on the monitor. Once the focus was established, the swirler was turned on and the flow was allowed to settle for a couple of minutes, at which point one 90 frame video was taken.

4.4 Procedure Used to Visualize Longitudinal Sections

To obtain the longitudinal images of the flow, the CCD camera was mounted horizontally on a tripod along side of the swirl chamber. The camera was oriented so as to be as perpendicular to the plane of the laser sheet as possible. By raising or lowering the tripod shaft, images were recorded at three adjacent axial locations along the tube. This allowed the visualization of a total length equal to three tube diameters downstream of the

sudden expansion. For the first section, the height of the camera was adjusted so as to capture the region of the tube just above the backward facing step, and the Toyo 12.5-75mm zoom lens was focused on the central jet tube so as to match the camera's focus plane with the plane of the laser sheet. The swirler was then turned on and the flow was allowed to settle for a couple of minutes, at which point one 90 frame video was taken for each of the investigated jet velocity ratios, ϕ.

Once all the jet velocity ratios were recorded at this first axial section of the tube, a 1/4 inch strip of tape was placed on the viewing chamber wall so as to just occupy the *uppermost* part of the camera's field of view. The tripod's camera support was then raised (without affecting the camera's distance to the axis of the test section tube) to the second axial location, defined by the position where the same piece of tape just occupied the *bottom* part of the camera's new field of view. The use of the tape therefore insured that there was a 1/4 inch overlap between the adjacent axial locations. Once the camera was ready in its new position, the tape was removed from the viewing chamber, and the same set of experiments as before were recorded. Finally, the 1/4 inch tape was used again to raise the camera up to the third axial location and the experiments were run.

This procedure resulted in the first section visualizing the flow in the range from the inlet to a distance downstream of 1.1 D, in the second section visualizing the flow in the range of .9 D to 2.0 D downstream of the inlet, and in the third section visualizing the flow in the range from 1.9 D to 3.0 D downstream of the inlet.

4.5 Image Processing

The recorded images were analyzed using a commercial package obtained from TSI Inc. Experimenting with interrogation area sizes revealed that a 32x32 pixel interrogation area was the smallest possible area that could be used without creating a lot of obviously incorrect vectors. Incorrect vectors were those which were either orders of magnitude larger than the surrounding flow or which were pointing in a highly unlikely direction. A 40x33 Cartesian grid was used to discretize the image files, and the correlation program's output were binary files containing vectors consisting of the x and y coordinates and the x and y velocities of the nodes on this grid.

The binary vector files were transferred to an SGI workstation where a Matlab script was used to create a quiver plot of the velocity field for each correlated image. The

velocity field was used to calculate the vorticity field of each frame by using second order finite difference methods to calculate the vorticity component normal to the plane of the light sheet:

$$\omega_z = \frac{\partial v}{\partial x} - \frac{\partial u}{\partial y}$$

The vorticity value at a point was therefore dependent on the velocity values of the 4 closest surrounding grid points. For the sake of comparison, the vorticity was also calculated by calculating the circulation around a point based upon a 3x3 square area and then dividing this value by the area of the square. This method was therefore dependent on the velocity values of the 8 closest grid points, potentially reducing the effect of an errant velocity vector on the vorticity value. However, it was found that both these methods gave substantially the same vorticity plots, and it was therefore decided to use the simpler second order difference method. For any given frame, the integral of the positive and negative vorticity (ie: the circulation) was calculated over three different areas of that frame: the entire frame, the left half of the frame, and the right half of the frame.

The complete series of 45 longitudinal velocity vector fields were also averaged to produce the kind of velocity field that an LDA measurement technique would have detected. For a given point in the grid, this averaging was accomplished by summing all 45 velocity values from the DPIVC movie at that point and dividing the sum by 45. A flow rate calculation was then undertaken by integrating these average velocities over the cross sectional area of the test section. More specifically, for a point at a given radial distance from the axis, an average of the velocity values on the left and right sides of the axis were taken and this new value was then integrated over the annulus area.

CHAPTER 5

Results

The detailed results are presented under two major headings corresponding to the experiments in which azimuthal cross sections were visualized and corresponding to the experiments in which longitudinal cross sections were visualized.

For reference purposes, a summary of the major results can be found at the end of this chapter.

5.1 Azimuthal Cross Sections

A typical velocity field plot obtained from these experiments can be seen in Figure 5.1. This plot shows that the DPIVC analysis program was not able to correlate the particle displacements in a large fraction of the flow field. Not enough vectors are present in the flow field to get an accurate picture of what is going on, but it can be seen from certain of the better correlated regions that a classic vortex structure is present.
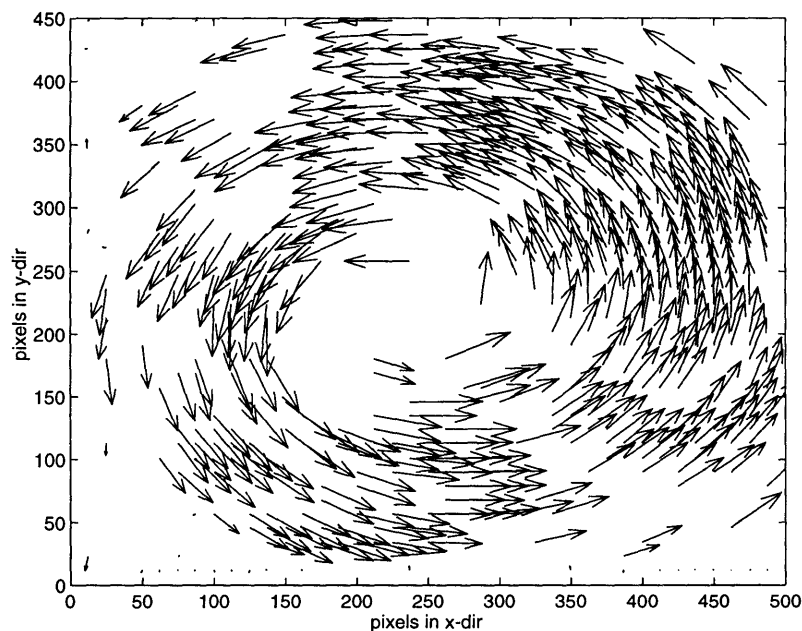
Figure 5.1. Velocity Field Obtained from an Azimuthal Cross Section of the Flow. The tube diameter ranges from 0 to 500 pixels. *Re=34,000, S=2.0.*

Figure 5.2 compares a raw image obtained from an azimuthal cross section to a raw image obtained from a longitudinal cross section and reveals that the former is much dimmer and much less sharp. This lack of clarity in the azimuthal image reduces the number of correlating pairs within each interrogation area, and the reduced contrast severely decreases the signal to noise ratio. The reasons for the azimuthal images' poor quality will be discussed in the next chapter.
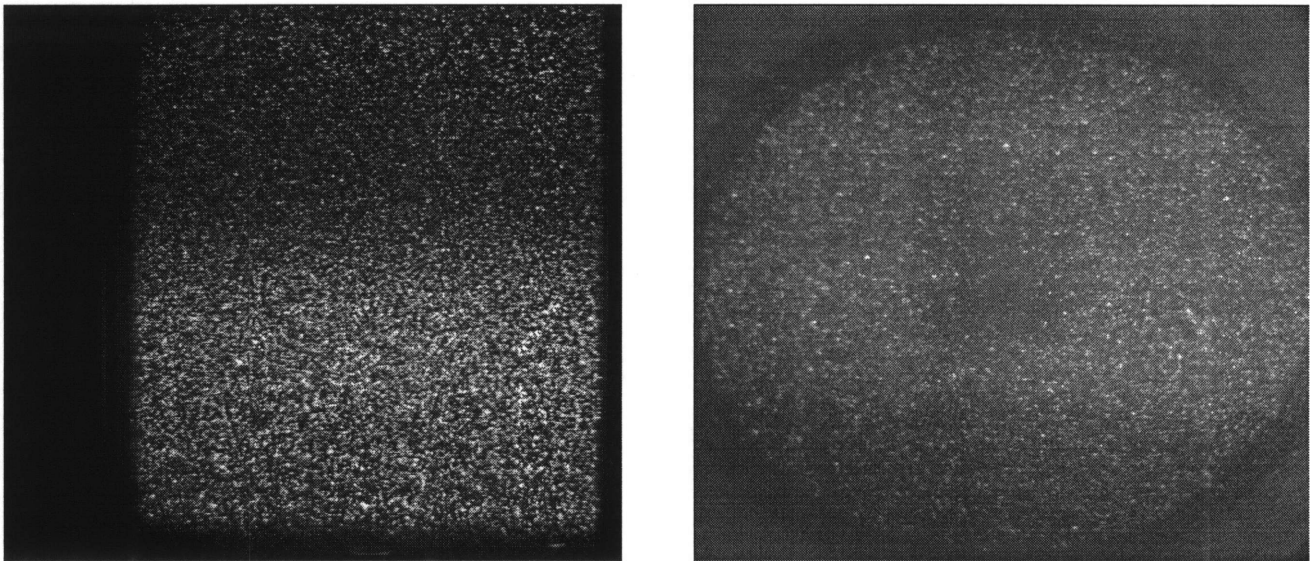
Figure 5.2. Comparison of Raw Longitudinal (left) and Azimuthal (right) Images.

5.2 Longitudinal Cross Sections

The results of these experiments are presented under four sub-headings: the first three of these correspond to the three investigated combinations of Reynolds' and swirl numbers, while the fourth corresponds to the calculated flow rate values obtained from the velocity plots.

The longitudinal velocity fields of the flows are represented in the form of quiver plots which span an area of 450X400 pixels. The images of the first axial section were recorded just downstream of the inlet, so that the presence of the backward facing step annulus can be imagined to be located directly under these plots at pixel locations between 0 and 100 and between 300 and 400. The primary jet tube can also be envisioned to be located directly below the 200 pixel location, and the secondary flow's entrance region is located in between the 100 and 300 pixel locations.

Another point to keep in mind is that the field plots have been presented in a vertical manner because of the test section's vertical orientation. In this context, the terms "above" and "below" are therefore equivalent to "downstream" and "upstream" in describing the location of flow features. **Furthermore, all lengths have been non- dimensionalized by the diameter of the test section tube, _D_.** Finally, a reference vector has been included on the left side of each velocity plot because the vector scaling changes from one plot to the next.

5.2.1 High Reynolds' Number and High Swirl Experiments, _Re=34,000_, _S=2.0_

5.2.1 A) Jet Velocity Ratio, $\phi=0.0$

A typical sampling of frames taken from the DPIVC movies of the high Reynolds' number and high swirl number flow with a jet velocity ratio of 0.0 can be seen in Figure 5.3. This figures displays the velocity field of the flow and the vorticity component normal to the plane of the light sheet for three successive axial locations in the tube.

The main observable characteristics of the flow field are the two eddies caused by the backward facing step annulus and the large columnar recirculation zone located along the entire axis of the tube.

The two eddies caused by the sudden expansion are clearly visible in the bottom corners of the velocity field plots in Figure 5.3. One can see that the area downstream of the left step is composed of a smaller eddy situated directly above the step and a much larger eddy $1/3$ D downstream of it, while the area downstream of the right step is composed of only one large eddy situated directly above the step. The complete, 45 frame DPIVC movie of this lowermost section shows the eddies above the step rising to a distance of about $1/3$ D and being replaced by another forming eddy just above the step (as is occurring in Figure 5.3). This phenomena can be seen to occur at each corner every 7-8 frames and this suggest that vortex shedding is occurring above the step. A 12 frame sequence showing this behavior can be found in Appendix A, Figure A.1.

The most striking feature of the entire flow field is the strong counterflow located on and around the centerline of the pipe. This counterflow has an axial velocity component whose order of magnitude is equal to that of the overall flow's
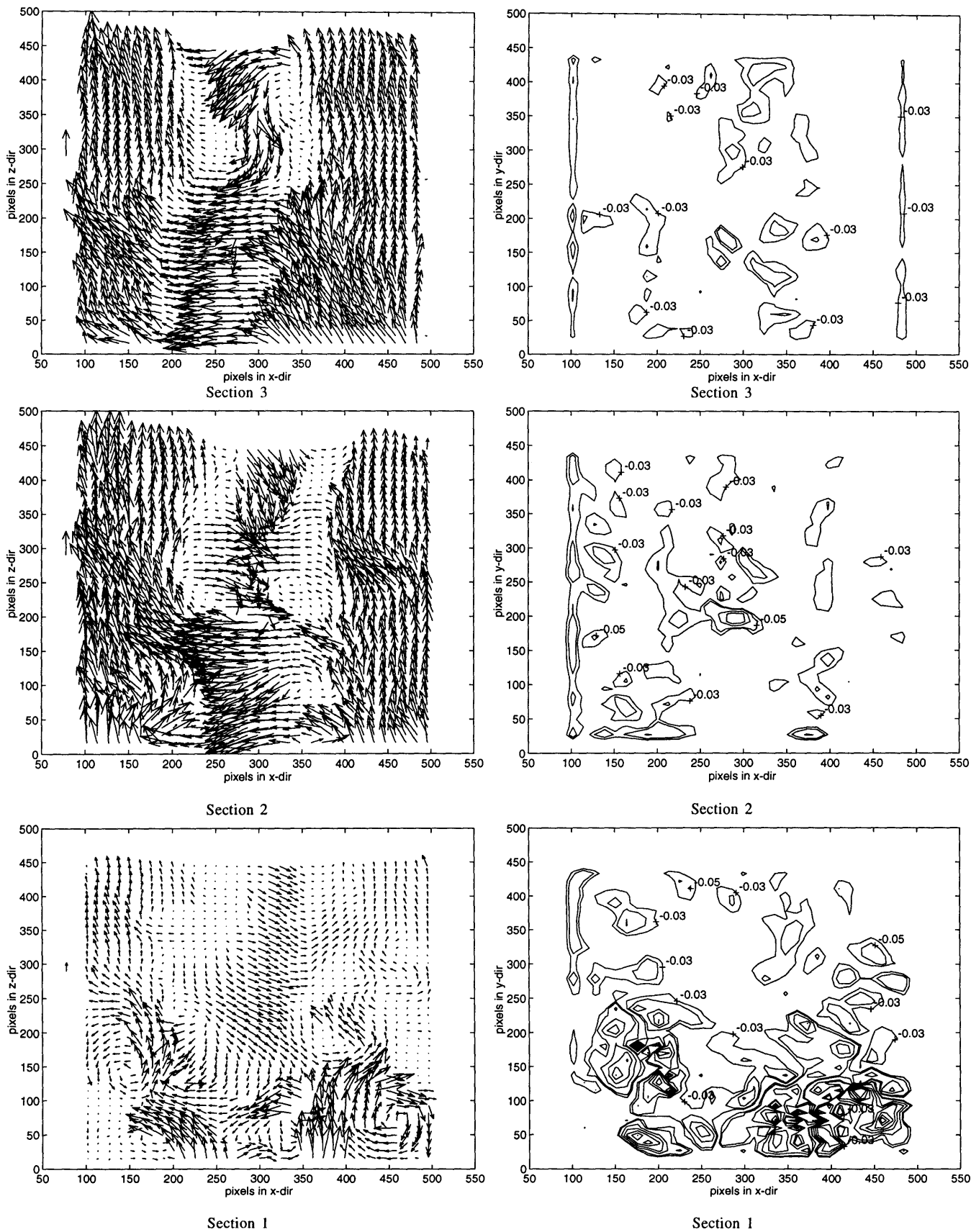
Figure 5.3. Instantaneous Velocity and Vorticity Plots; *Re=34,000; S=2.0; φ=0.0.* The left column displays the velocity field, the right column displays the vorticity field. All *unmarked* vorticity isocontours have a positive sign.

40
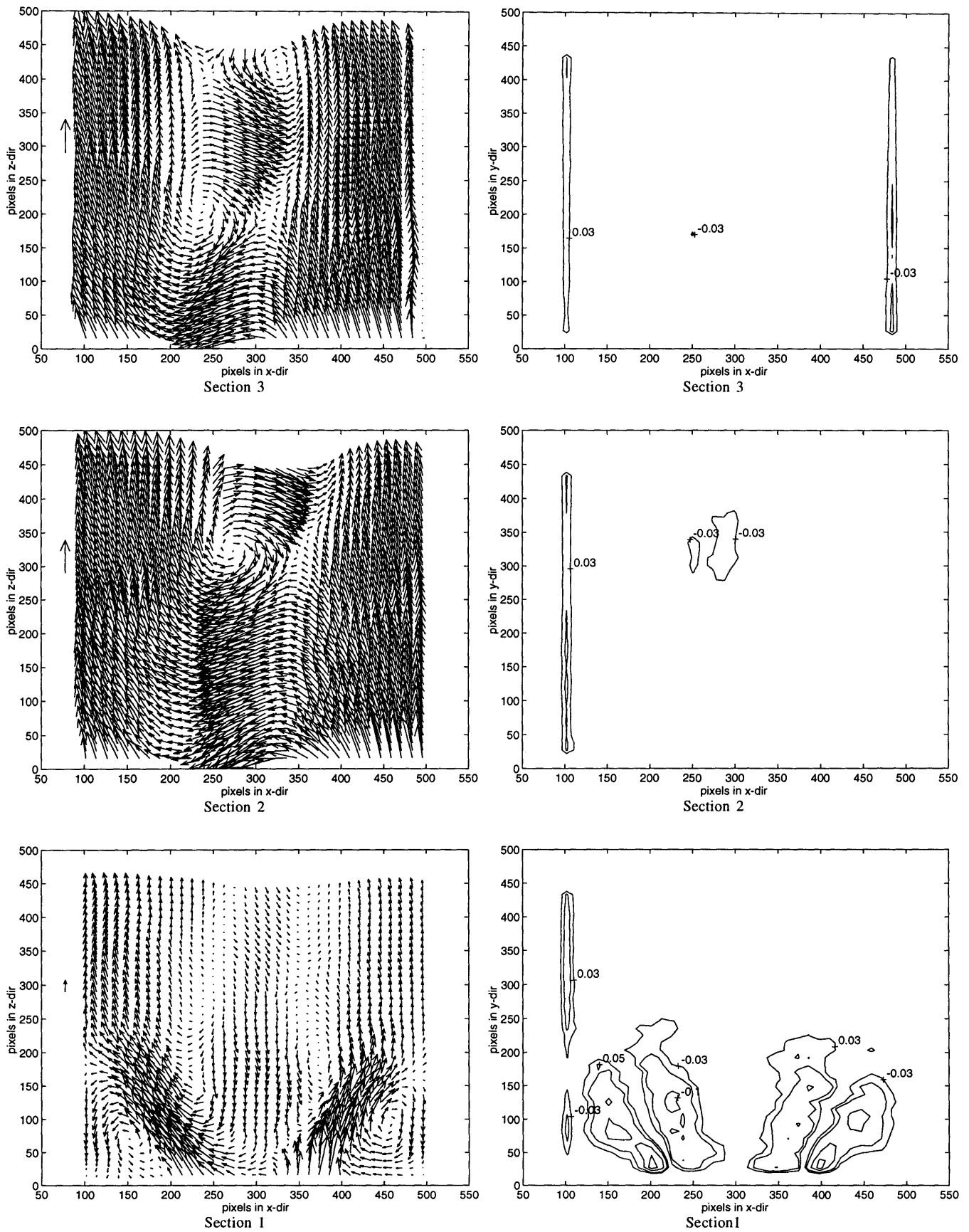
Figure 5.4. Averaged Velocity and Vorticity Plots; *Re=34,000;* *S=2.0; φ=0.0.* The left column displays the velocity field, the right column displays the vorticity field. All *unmarked* vorticity isocontours have a positive sign.

41

mean velocity. The counter-flowing column of fluid has a diameter ranging from a maximum of about 1/2 D near the inlet to a minimum of about 1/4 D at an axial location of 3.0 D. Flow visualizations using small air bubbles in the flow showed that the bubbles would travel along the axis from the very top of the tube all the way down to the inlet, suggesting that the recirculation column spans the entire length of the tube.

Though the column diameter seems to decrease as a function of height, it does so in an oscillating fashion. This suggests that the center of the column is moving in and out of the laser light sheet at several axial locations.

The vorticity plot of the lowermost section shows two regions of high vorticity located just above the inlet, in between the eddies created by the backward facing step annulus. Axially, these two regions of high vorticity stretch from just above the flow inlet to a downstream location of about 3/4 D. It is important to notice that these two main areas of vorticity actually have several vorticity peaks within them.

Areas of less intense vorticity also exist above these two main zones, and islands of moderately strong vorticity persist along the axis at least up to an axial height of 3.0 D. Looking closely at all these centrally located vorticity zones reveals that those located on the left of the centerline of the tube usually have a negative value, while those located on the right have a positive value. The complete 45 frame DPIVC movie of this flow shows that it is difficult to track these islands of vorticity from one frame to another since their shape is continually changing.

The values obtained from integrating the vorticity over various areas can be seen in Appendix B, Table B.1, where the mean values over 45 frames are listed for all three sections of the tube. The mean circulation's calculated over the entire section area show that the positive and negative components are practically equal to each other in all three axial locations. Furthermore, it can be seen from the data how the total circulation is twice as high in the first section as it is in the second and third sections. Comparing the circulation values of the left and right hand sides of each frame shows that there is a good correlation between the left side's positive and negative circulation with the right side's negative and positive
circulation, respectively. It can also be seen that, for all three axial locations, the left side has a net negative circulation while the right side has a net positive circulation.

The velocity and vorticity fields averaged over the entire 45 frame DPIVC movie can be seen in Figure 5.4. Considering the large asymmetries in each individual frame and the large variations from one frame to another, the averaged velocity and vorticity fields of the first section reveals a surprising amount of symmetry about the axis of the tube. A single, large eddy can be found above each step, and a straight column of counter flow can be seen at the center of the tube. One can also see that the secondary flow reattaches to the wall at an axial location of about $1/2$ D downstream of the inlet.

The averaged vorticity field of the first section shows that the central vorticity islands have only one peak value, while the fields of the second and third sections show greatly reduced vorticity values.

The velocity field of the second section, meanwhile, shows a large eddy just to the left of the tube axis driving a counter-flowing column of fluid. Finally, the third axial section shows two of these larger eddies, one on either side of the centerline, rotating in opposite directions.

5.2.1 B) Jet Velocity Ratio, $\phi=4.0$

The images taken of the $S=2.0$, $\phi=4.0$ case (not included in this thesis) show that there is very little difference between this case and the $\phi=0.0$ case discussed above. In fact, this flow regime is also characterized by the two recirculation zones caused by the backward facing step annulus, and the large counter flowing zone located along the axis of the tube.

The only difference between this flow and the $\phi=0.0$ case lies in the step vortex shedding frequency. Indeed, there are many sequences within the 45 frame DPIVC movie which suggest that these eddies are rising above the step, and this of course is consistent with vortex shedding. However, there are other sequences which suggest that some eddies might actually be stagnant in the axial direction, or even moving upstream slightly. These factors have combined to make it very difficult to calculate any consistent shedding frequency for this flow regime. There are also several frames where a very weak second eddy can be found directly downstream of the first eddy.

The values obtained from integrating the vorticity over various areas can be seen in Appendix B, Table B.2, where the mean values over 45 frames are listed for all three sections of the tube.

5.2.1 C) Jet Velocity Ratio, $\phi=12.0$

A typical sampling of frames taken from the DPIVC movies of the high Reynolds' number and high swirl number flow with a jet velocity ratio of 12.0 can be seen in Figure 5.5. This figure displays the velocity field of the flow and the vorticity component normal to the plane of the light sheet for the three successive axial tube locations.

The main observable characteristics of this flow field are the two eddies caused by the backward facing step annulus, the high velocity region near the axis caused by the jet, and the reduced counterflow region surrounding this jet.

The step-induced eddies can clearly be seen in the corners at the bottom of Figure 5.5. Looking at the entire 45 frame sequence shows that there is no clear vortex shedding frequency. In fact, some of the frame sequences show the eddies staying in the same axial position. On the other hand, other sequences show that the eddies move both downstream and upstream and have an amplitude of motion of about 1/8D, up to a maximum downstream location of about $0.38D$ Smaller eddies above the large ones do appear occasionally, but without any predictable pattern.

Looking at the axis region of the velocity fields reveals the presence of the high velocity jet. In fact, the velocities are so high in this region that the analysis algorithm, set up to capture displacements caused by the much slower mean flow, cannot track the particle movements reliably and produces obviously incorrect vectors or no vectors at all. This very high velocity central region has an axial length of about $1.0\,D$ in Figure 5.5, but this varies substantially from one frame to another.

In the first section of the tube, the region immediately on either side of the jet shows signs of very slow axial velocities and even flow reversals having the same order of magnitude as the mean flow. The flow reversal region is very small and extends for about $1/4\,D$ downstream of the backward facing step. The velocity fields for the second and third axial locations, meanwhile, show a much more uniform axial velocity across the entire diameter, though there are definitely pockets of decreased (but not reversed) axial flow velocities near the axis. Again, the appearance and disappearance of these pockets suggests that they are part of a core moving in and out of the light sheet.

The vorticity plots for the first section are quite different from those with $\phi=0.0$ and with $\phi=4.0$. Indeed, a prominent vorticity zone can be seen at the center of the frame, with positively valued contours located on the left of the axis, and with negatively valued
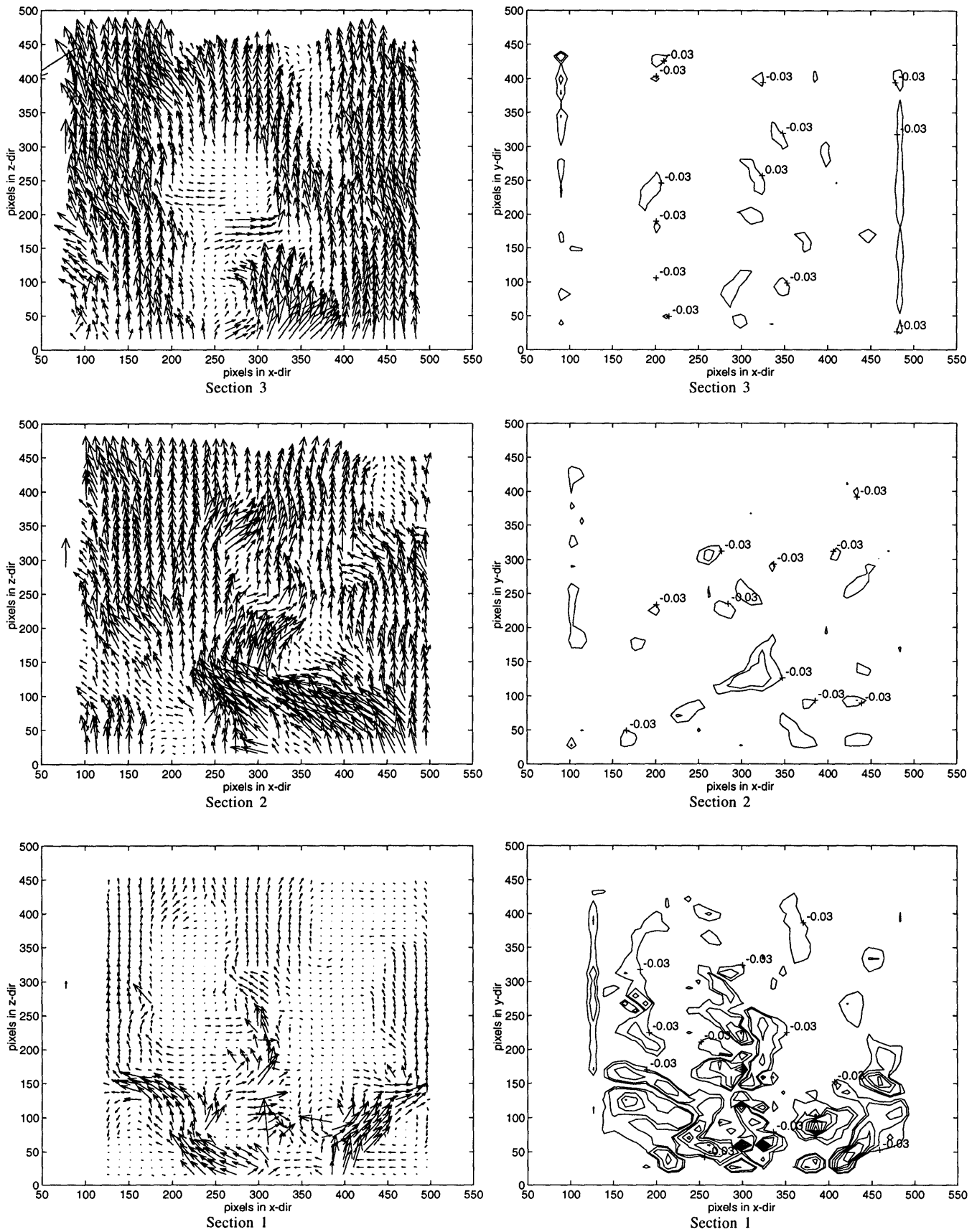
Figure 5.5. Instantaneous Velocity and Vorticity Plots; *Re=34,000; S=2.0; φ=12.0.* The left column displays the velocity field, the right column displays the vorticity field. All *unmarked* vorticity isocontours have a positive sign.

45
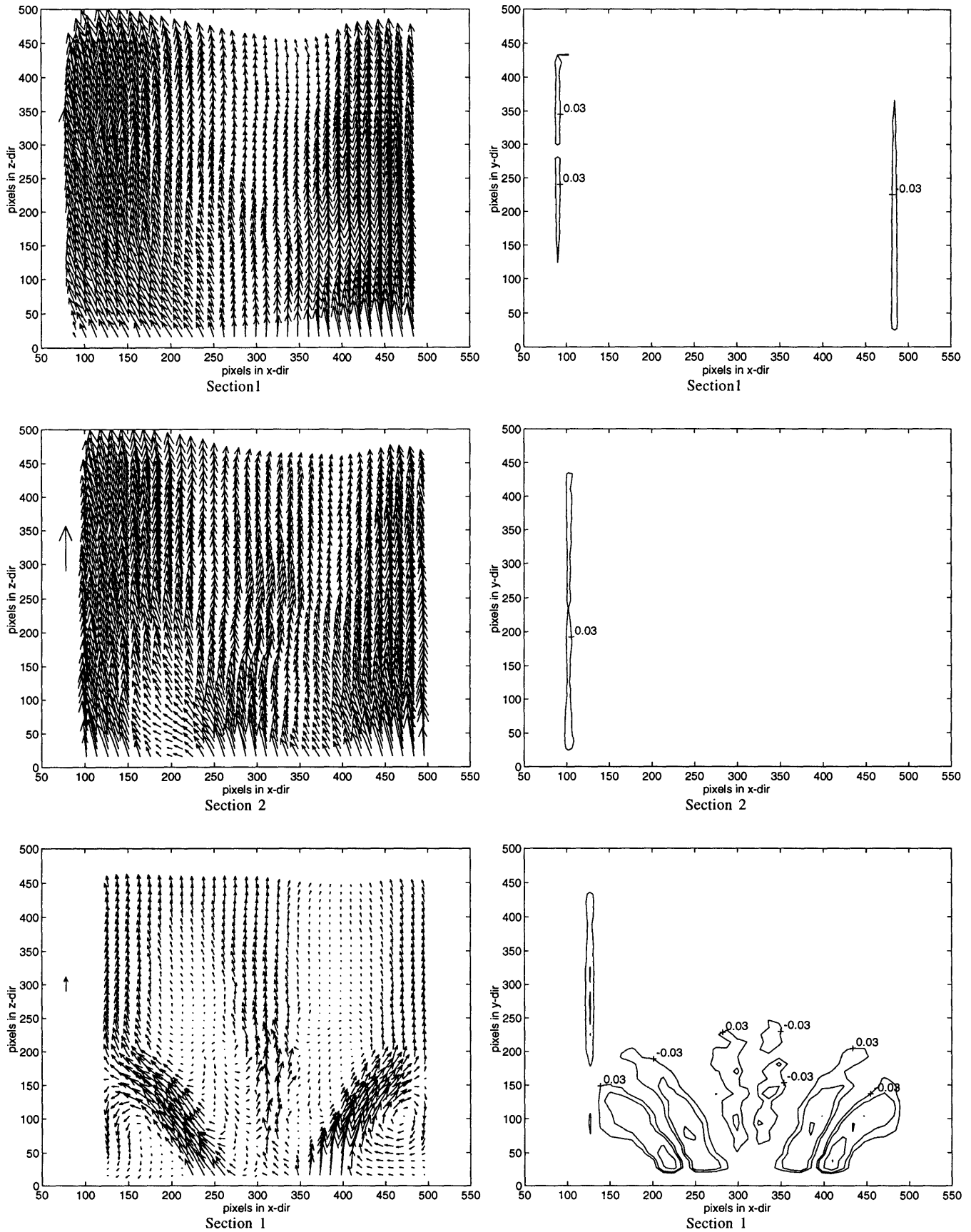
Figure 5.6. Averaged Velocity and Vorticity Plots; *Re=34,000; S=2.0; φ=12.0*.The left column displays the velocity field, the right column displays the vorticity field. All *unmarked* vorticity isocontours have a positive sign.

46

contours located on the right of the axis. Surrounding this central vorticity column are vorticity contours similar to those seen in the previous cases. The latter regions of vorticity stretch axially from just above the inlet to a downstream location of about 1/2 D, and areas of less intense vorticity can be seen to exist above these main zones.

The results obtained from integrating the vorticity over the three areas can be seen in Appendix B, Table B.3, where the mean values over 45 frames are listed for all three sections of the tube. Once again, the mean circulations calculated over the entire section area show that the positive and negative components are practically equal to each other in all three axial locations. Furthermore, it can be seen from the data how the total circulation is twice as high in the first section as it is in the second and third sections. Comparing the circulation values of the left and right hand sides of each frame shows that there is a good correlation between the left side's positive and negative circulation with the right side's negative and positive circulation, respectively. It can also be seen that, for the first axial location, the left side has a net positive circulation while the right side has a net negative circulation.

The velocity and vorticity fields averaged over the entire 45 frame DPIVC movie can be seen in Figure 5.6. These images show that this flow condition is completely different from the $\phi=0.0$ and $\phi=4.0$ cases. The important characteristics which can be seen in the first section are the high velocity zone created by the primary jet, the two step-induced eddies and the limited counter-flowing regions around the jet. One can also see that the secondary flow reattaches to the wall at an axial location of about 1/2 D downstream of the inlet. The second and third axial sections are characterized by a symmetric, plug like flow. Looking more closely, however, reveals that the upstream part of the second section's velocity field has a velocity peak near the axis due to the primary jet. The primary jet's influence can be seen to decrease as one travels downstream and it's presence can no longer be felt in the third section of the tube, where a small velocity deficit near the axis can be seen.

5.2.1 D) Jet Velocity Ratio, $\phi=20.0$

A typical sampling of frames taken from the DPIVC movies of the high Reynolds' number and high swirl number flow with a jet velocity ratio of 20.0 can be seen in Figure 5.7. This figure displays the velocity field of the flow and the vorticity component normal to the plane of the light sheet for the three successive axial tube locations.
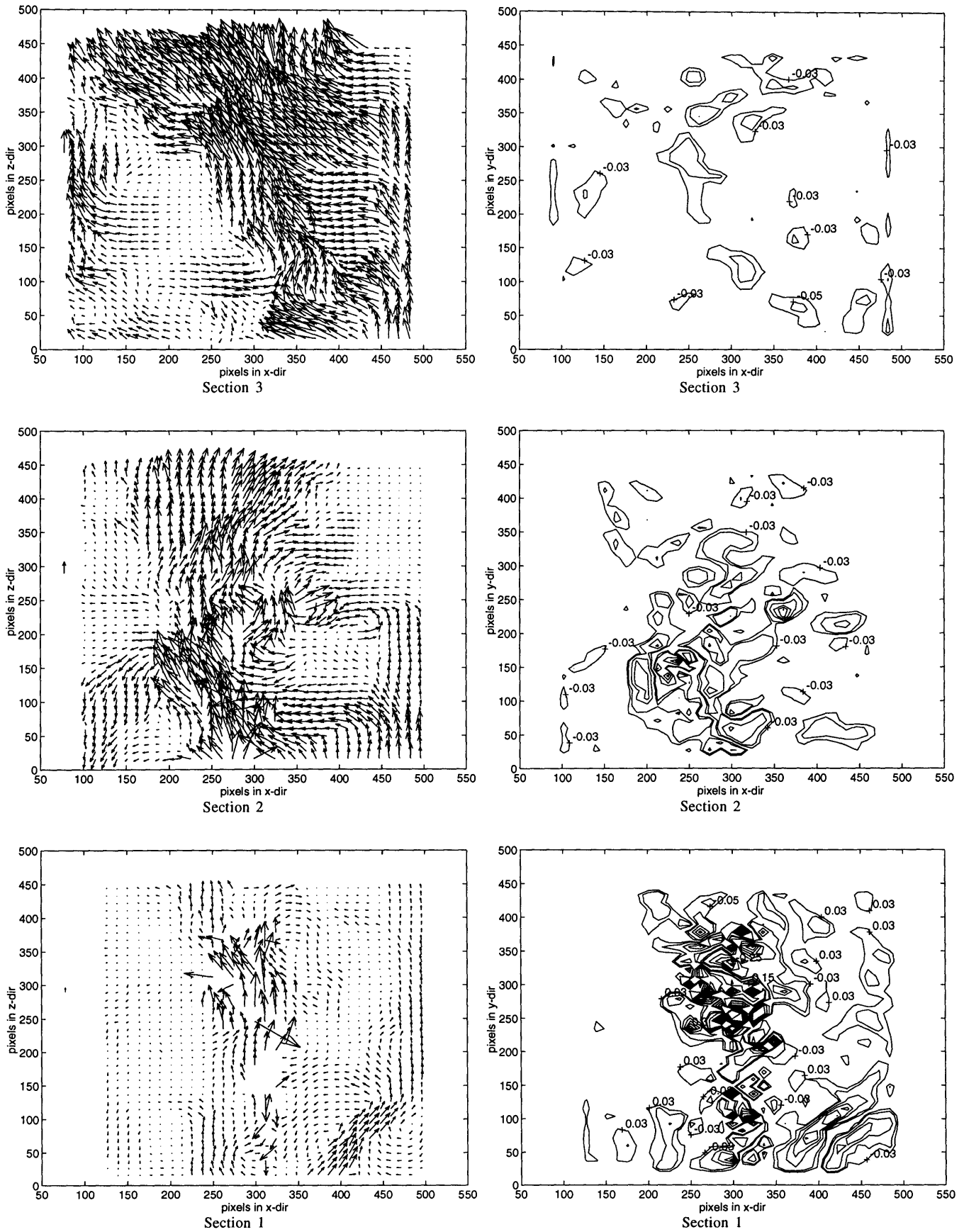
Looking at the velocity and vorticity fields for this flow reveals that it is significantly different from any described so far. The high velocity region defined by the jet assumes a dominant role, and both the step induced recirculation zones as well as the central recirculation zone have been modified completely.

The velocity plots show that the high velocity region surrounding the jet survives all the way up to the third section (and probably significantly further). The diameter of this high axial velocity core grows from about 1/8 D at an axial distance of 1/2D downstream of the step to a diameter of about 1/4 D at an axial distance of 3.0 D downstream of the step. Once again, many of the grid points inside the core are blank because of the analysis program's inability to accommodate the high velocities of the jet. Furthermore, some of the vectors which are present inside the core have questionable directions and magnitudes.

A particularly interesting aspect of this flow is the fact that the primary jet and the secondary flow wander together from one side of the tube to the other. This meandering occurs about 6 times during the three second movie, and the transition from one side of the tube to the other occurs quite smoothly. In fact, the 45 frame movie reveals that the jet stays in one side of the tube for about 5 frames and then travels through the center for about 2 frames before reaching the opposite side of the tube. The oscillatory behavior of the combined primary and secondary flow can also be seen in the velocity fields of the second and third sections as well. A 15 frame sequence taken from the DPIVC movie can be found in Appendix A, Figure A.2, and clearly displays the oscillatory behavior in the first axial section.

The presence of the high velocity jet has a profound effect on the surrounding velocity and vorticity fields. Looking at the frame from the first section, one can see that the central recirculation zone has all but disappeared. In its place is a flow structure which seems to divide the tube down the middle of the axis; one side contains the combined flow of the primary jet and the secondary flow and is characterized by large axial velocities while the other side is dominated by very low axial velocities and even has some counterflow regions along the tube wall. The size of these regions of counterflow varies greatly, and can reach an axial length of about 1/2D or more. Though no counterflow occurs downstream of an axial location of about 1.0D, regions of reduced velocity do exist beyond this point.

Figure 5.7. Instantaneous Velocity and Vorticity Plots; *Re=34,000; S=2.0; φ=20.0.* The left column displays the velocity field, the right column displays the vorticity field. All *unmarked* vorticity isocontours have a positive sign.

49
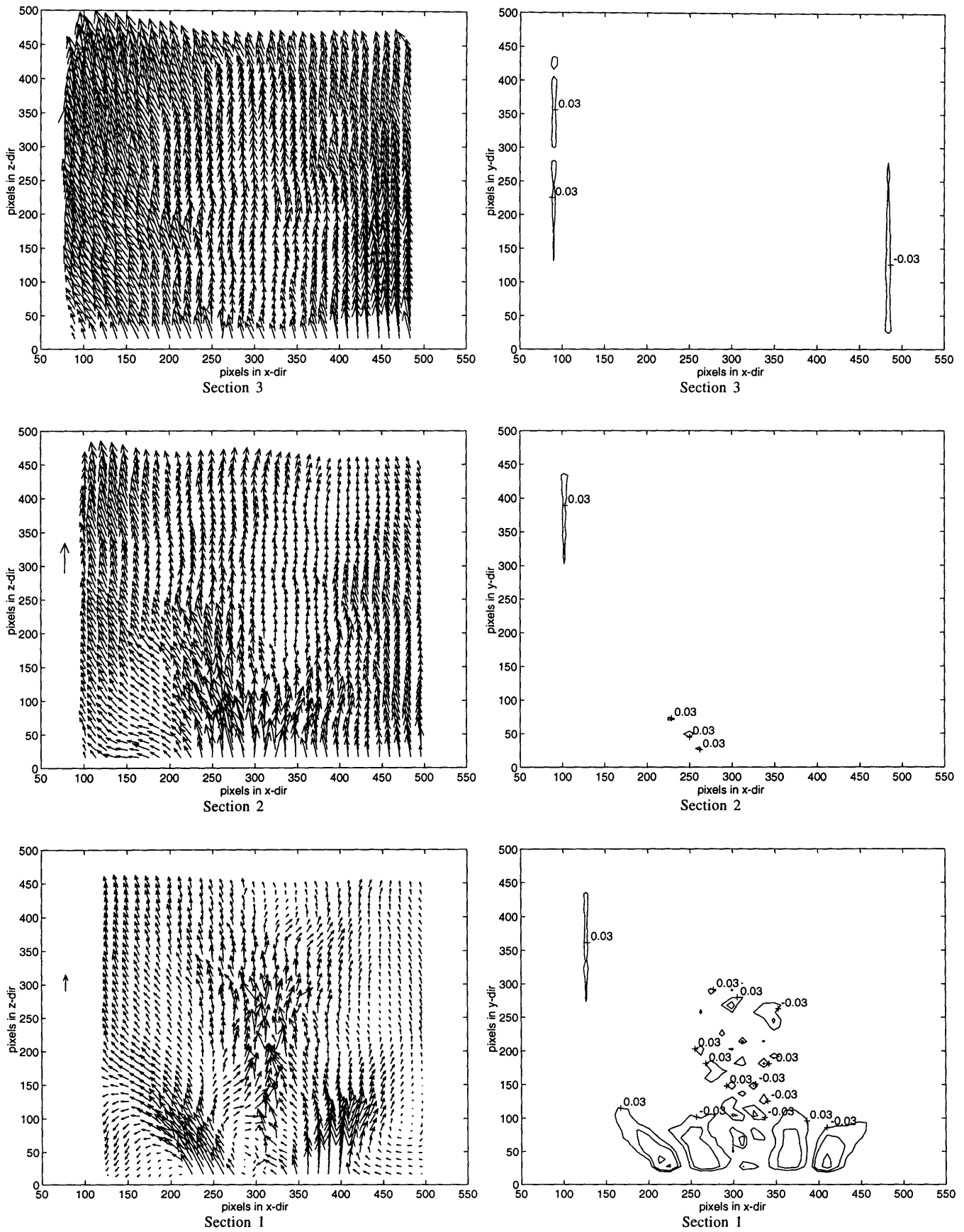
Figure 5.8. Averaged Velocity and Vorticity Plots; *Re=34,000;*
S=2.0; φ=20.0. The left column displays the velocity field, the right
column displays the vorticity field. All *unmarked* vorticity
isocontours have a positive sign.

50

When the combined jet and secondary flow are located in a given side of the tube, they reattach to the side's wall at a height of about $0.38D$ downstream of the inlet. This reattachment point then becomes the furthest point downstream that the single eddy shed from that side's step can reach. The opposite side, meanwhile, exhibits two or three weaker eddies shedding off of the jet and rising up to a distance of $1.1D$ downstream of the inlet. The vorticity plots show that the highest vorticity values occur in the region defined by the primary jet. The original vorticity structure from the previous cases is still present, but is reduced in strength and is completely overshadowed by the primary jet vorticity.

The results obtained from integrating the vorticity over the three areas show similar trends as the previous cases and can be seen in Appendix B, Table B.4. Once again, the mean circulations calculated over the entire section area show that the positive and negative components are practically equal to each other in all three axial locations. Interestingly, it can be seen from the data that the total circulation in the first section is about 1.6 and 2.0 times higher than it is in the second and third sections, respectively. Comparing the circulation values of the left and right hand sides of each frame shows that there is a good correlation between the left side's positive and negative circulation with the right side's negative and positive circulation, respectively. It can also be seen that, for the first axial location, the left side has a net positive circulation while the right side has a net negative circulation.

The velocity and vorticity fields averaged over the entire 45 frame DPIVC movie can be seen in Figure 5.8. These images show that this flow condition is most similar to the $\phi=12.0$ case. One can see that the high velocity zone created by the primary jet is larger than in the $\phi=12.0$ case and can be seen all the way up to the top of the second section. Interestingly, practically all signs of counterflow have disappeared from the flow. The symmetry of the velocity field is also evident in all three axial sections, and this is surprising since the flow is so very asymmetric on a frame by frame basis. One can also see that the secondary flow reattaches to the wall at an axial location of about $1/2\ D$ downstream of the inlet, just above the step induced eddies.

5.2.2 High Reynolds' Number and Low Swirl Experiments, $Re=35,000$, $S=0.5$
5.2.2 A) Jet Velocity Ratio, $\phi=0.0$

A typical sampling of frames taken from the DPIVC movies of the high Reynolds' number and high swirl number flow with a jet velocity ratio of 0.0 can be seen in Figure
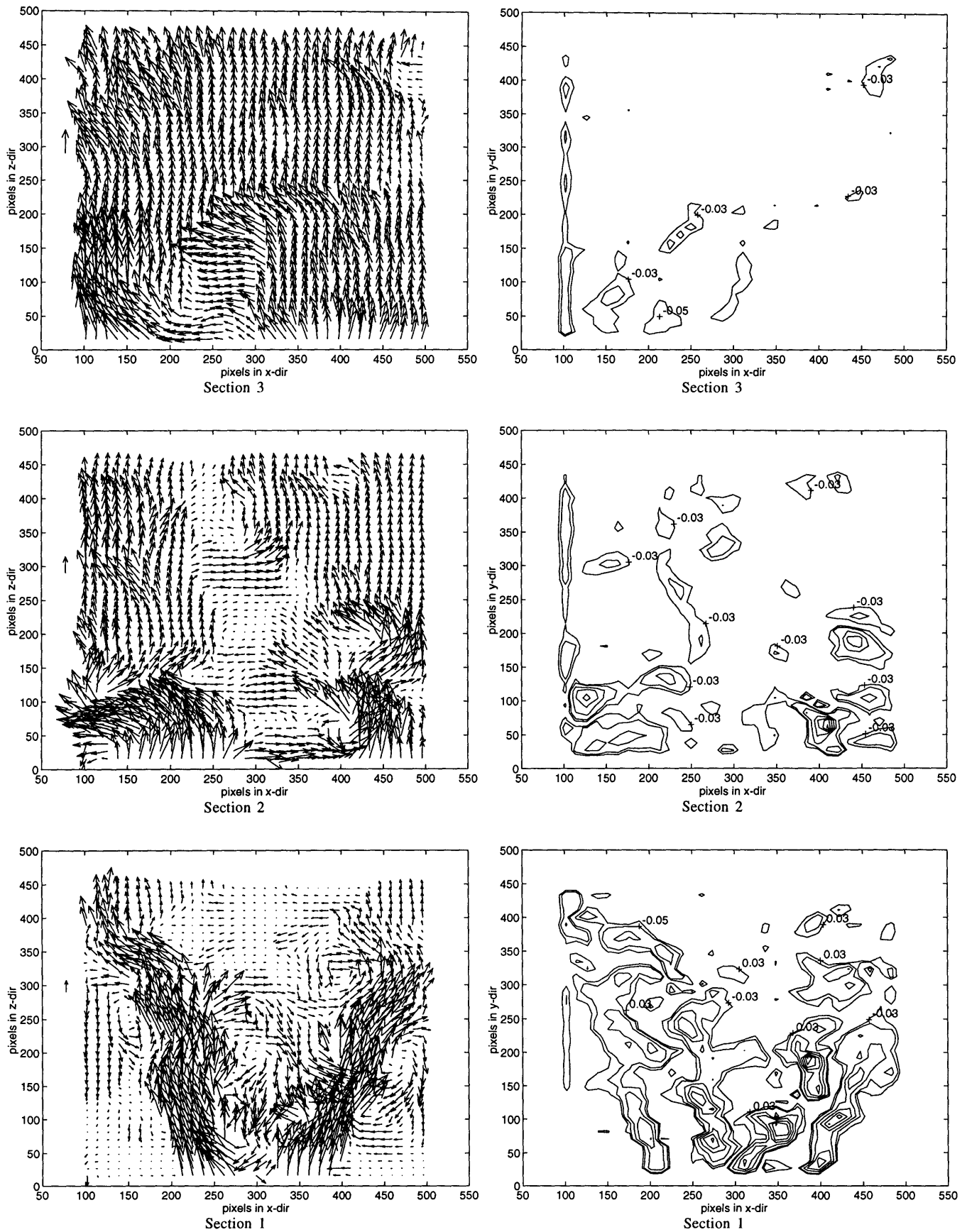
5.9. This figure displays the velocity field of the flow and the vorticity component normal to the plane of the light sheet for three successive axial locations in the tube.

The velocity fields taken at the first section reveal that the eddies above the step rise up to a height of almost $1.0D$ downstream of the inlet. Interestingly, the eddies on the left travel further downstream than those on the right. The reattachment point of the main flow with the walls occurs at a distance just downstream of these eddies. This is significantly further downstream than in the runs with $Re=38,000$ and $S=2.0$. It can also be seen that in most frames, the recirculation region above the step is made up of one single eddy located at the top of the region and of an extensive, very low velocity zone just beneath it.

The entire DPIVC movie shows that the main step induced eddy on the left side of the tube travels from a low point of about $0.5D$ above the step to a high point of about $.75D$ above the step. The eddy takes about 8 frames to travel this distance, though there is some variation from one sequence to another. Once the eddy reaches its highest point, it begins to dissipate while the main flow breaks into the long stagnant region beneath it to create an upstream eddy. On the right hand side, the rise and fall of the eddy is not as structured but it seems to travel from a low position of $0.25D$ above the step to a high position of $0.6\ D$ above the step.

The central recirculation zone can be seen to have an axial extent of about 1.3D, starting from just above the primary jet position. Certain counter-flowing regions sporadically appear and disappear from the frames, so that it is possible that the core is entering and leaving the plane of the light sheet. The back-flowing column has a diameter of about $0.25D$ just above the jet, and the stagnant zone (where the velocity is very small but not negative) grows to a size of about $0.5D$ by the top of the first section.

The vorticity plots show patterns similar to those found in the case of high Re and high swirl, though the second and third axial locations show reduced vorticity magnitudes. In fact, the central recirculation zone is again characterized by long areas of high negative vorticity on the left side of the axis and long areas of positive vorticity on the right side of the axis. One can see that these two zones have a length of about $0.7D$ It is important to notice that these two main areas of vorticity actually have several vorticity peaks within them. The complete 45 frame DPIVC movie of this flow shows that it is difficult to track these islands of vorticity from one frame to another since their shape is continually changing. The outer step recirculation zone, meanwhile, is characterized by regions of

Figure 5.9. Instantaneous Velocity and Vorticity Plots; *Re=35,000; S=0.5; ϕ=0.0.* The left column displays the velocity field, the right column displays the vorticity field. All *unmarked* vorticity isocontours have a positive sign.

53
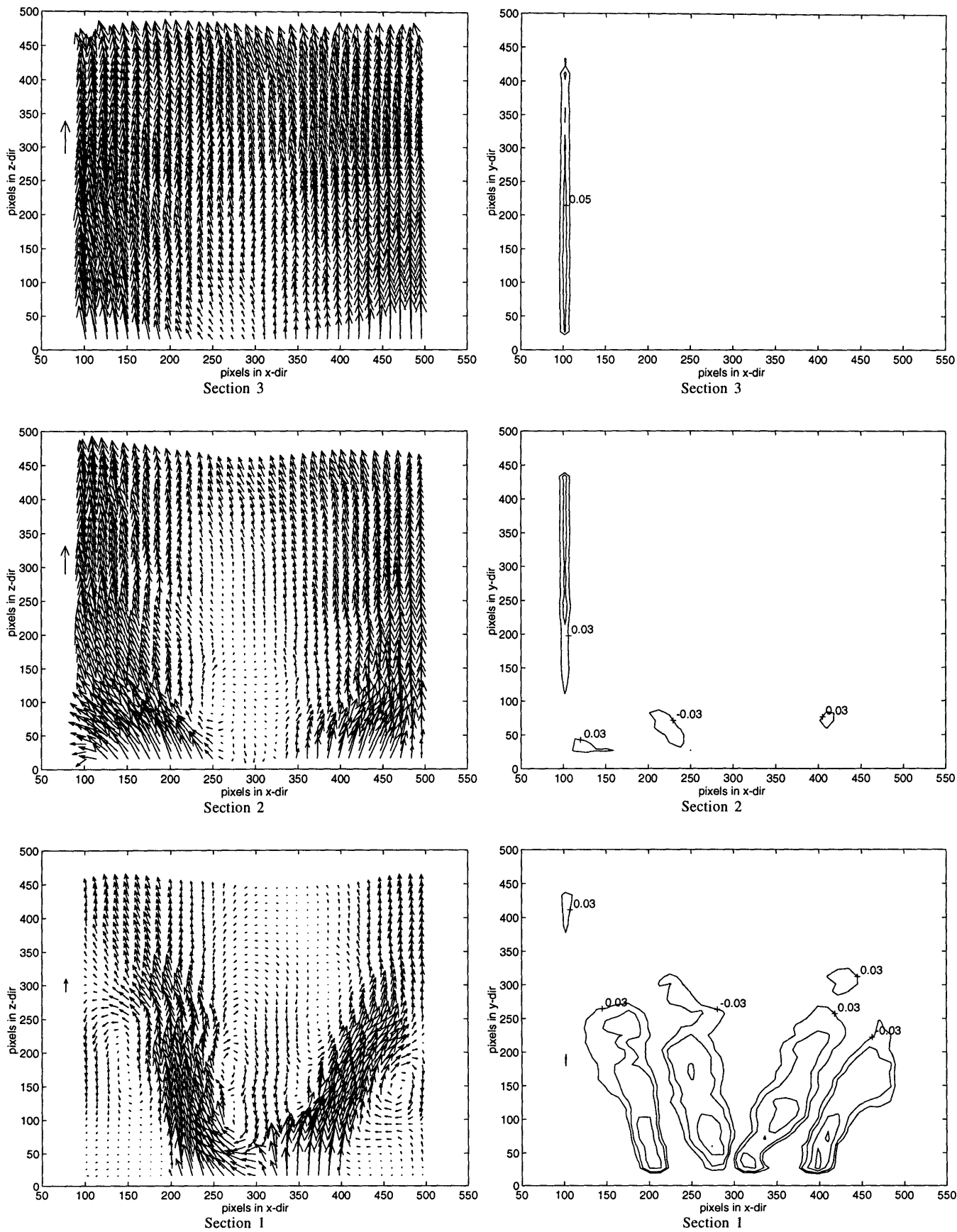
Figure 5.10. Averaged Velocity and Vorticity Plots; *Re=35,000;*
S=0.5; φ=0.0. The left column displays the velocity field, the right
column displays the vorticity field. All *unmarked* vorticity
isocontours have a positive sign.

54

positive vorticity on the left side (with a length of about 0.75D) and by regions of negative vorticity on the right side (with a length of about 0.5D).

The values obtained when integrating the vorticity in all three axial sections can be seen in Appendix B, Table B5. The total positive and negative vorticity integrated over the entire frame have very close absolute values at all three axial locations. It can also be seen that the vorticity in the first section is about twice and three times as high as in the second and third sections, respectively. Finally, comparing the circulation values of the left and right hand sides of each frame shows that there is a good correlation between the left side's positive and negative circulation with the right side's negative and positive circulation, respectively. It can also be seen that, for all three axial locations, the left side has a net negative circulation while the right side has a net positive circulation.

The velocity and vorticity fields averaged over the entire 45 frame DPIVC movie can be seen in Figure 5.10. The first section's velocity field clearly shows a slight asymmetry in the reattachment points of the left and right secondary flow branches as well as in height reached by the step induced recirculation zones. This fact correlates well with the patterns observed in the individual movie frames.

A straight column of counter flow about 1.3D in length can be seen at the center of the tube, starting from a height of about 1/8 D above the inlet. One can also see that the secondary flow reattaches to the wall at an axial location of about 0.5D downstream of the inlet. Interestingly, the vorticity field of this first section shows that the central vorticity islands have only one or two peaks. Looking closely at the velocity field of the second section, one can see a wake like velocity deficit at the center of the tube. This deficit becomes smaller in the flow direction and has practically disappeared by the top of the third section.

5.2.2 B) Jet Velocity Ratio, ϕ=3.9

The images obtained for the ϕ=3.9 case (not displayed in this thesis) show that there is very little difference between this case and the ϕ=0.0 case discussed above. In fact, this flow regime is also characterized by the two recirculation zones caused by the backward facing step annulus, and the limited counter flowing zone located along the axis of the tube.

The DPIVC movie of the first section's velocity fields reveals that, once again, the formation of a second upstream eddy seems to occur when the first one travels so far downstream that the secondary flow breaks into the stagnant zone. It is difficult to calculate a precise frequency for this phenomena, but several frame sequences suggest that it occurs every four to eight frames or so.

The values obtained when integrating the vorticity in all three axial sections can be seen in Appendix B, Table B6.

5.2.2 C) Jet Velocity Ratio, $\phi=11.6$

A typical sampling of frames taken from the DPIVC movie of the high Reynolds' number and high swirl number flow with a jet velocity ratio of 12.0 can be seen in Figure 5.11. This figure displays the velocity field of the flow and the vorticity component normal to the plane of the light sheet for the three successive axial locations in the tube.

Looking at the velocity and vorticity fields of this flow reveals that it is significantly different from the one with a jet velocity ratio $\phi=3.9$. In the first axial section of the tube, the primary jet completely destroys the central recirculation zone and modifies the step induced recirculation as well.

The velocity fields for this axial section suggest that the primary jet and the secondary flow oscillate around the axis together. In fact, the complete DPIVC movie shows the high velocity region created by the combination of the primary jet and the secondary flow oscillating from one side of the tube to the other. This meandering occurs about 4 times during the 3 second movie, and the transition from left to right occurs quite smoothly. Indeed, the 44 recorded frames show the combined jet and secondary flow residing in the left side of the tube for about 6 to 10 frames, then moving through the center of the tube for 1 to 4 frames, and finally residing in the right side for 5 to 6 frames. A 22 frame sequence taken from the DPIVC movie can be found in Appendix A, Figure A.3, and clearly displays the oscillatory behavior in the first axial section.

When this high velocity flow is located in a given side of the tube, it reattaches to that side's wall at a height of about $0.5D$ above the inlet. This reattachment location then becomes the furthest point downstream reached by the eddies shed from that side's step. The opposite side, meanwhile, exhibits eddies shedding off of the jet itself and these eddies tend to create a recirculation zone along the wall. These eddies can be seen to be much
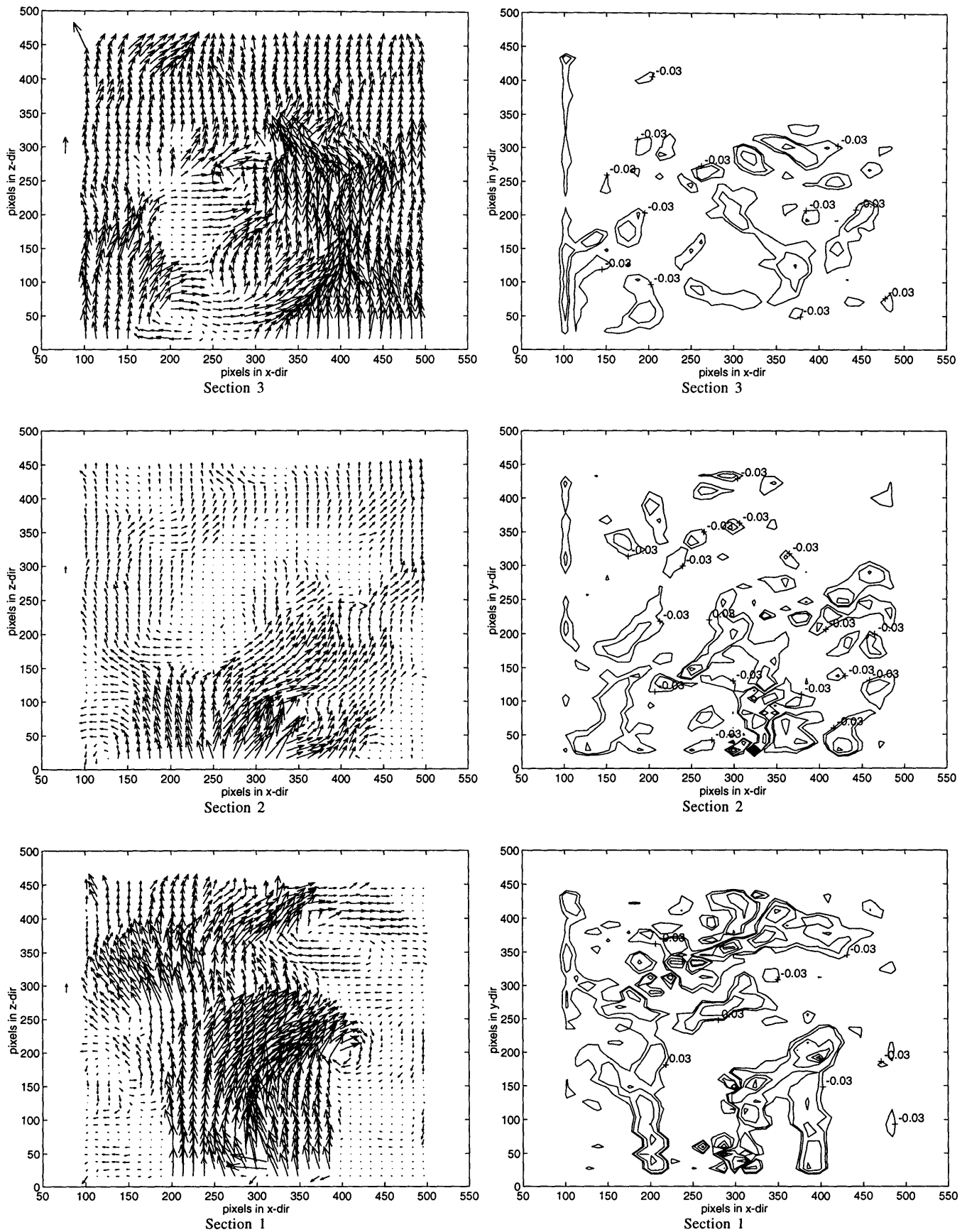
Figure 5.11. Instantaneous Velocity and Vorticity Plots; Re=35,000; S=0.5; φ=11.6. The left column displays the velocity field, the right column displays the vorticity field. All *unmarked* vorticity isocontours have a positive sign.

57
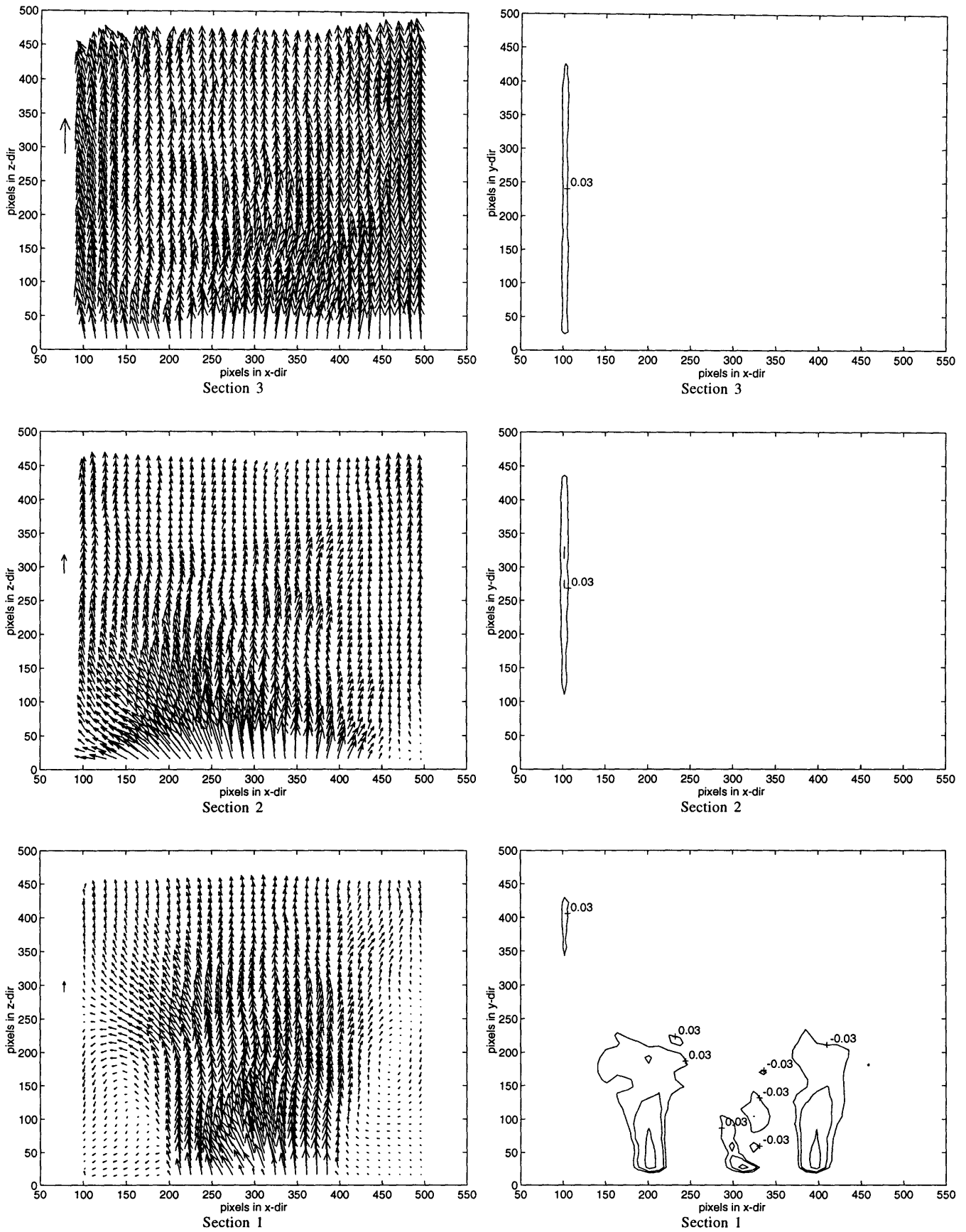
Figure 5.12. Averaged Velocity and Vorticity Plots; Re=35,000; S=0.5; φ=11.6. The left column displays the velocity field, the right column displays the vorticity field. All *unmarked* vorticity isocontours have a positive sign.

58

weaker than their counterparts on the side with the jet and can travel up to a distance of 0.8-1.0D before disappearing.

The vorticity plots show that the highest vorticity values occur in the region defined by the primary jet. The vorticity structure of the central recirculation zone present in previous cases has completely disappeared, having been dominated by the effect of the jet. The integrated vorticity values for all three axial sections can be seen in Appendix B, Table B.7. These figures show that there is a good correlation between the total positive and negative vorticities, and that the total vorticity in the flow decreases by about 25% from the first to the second section, and by about 41% from the first to the third section. It can also be seen that, for all three axial locations, the left side has a net negative circulation while the right side has a net positive circulation.

The velocity and vorticity fields averaged over the entire 45 frame DPIVC movie can be seen in Figure 5.12. The velocity field of the first section shows that this flow is completely dominated by the primary jet. All signs of counterflow have completely disappeared from the flow, and the high velocity zone created by the primary jet is felt by the flow all the way up to the top of the third section. The symmetry of the velocity field is also evident in all three axial sections, and this is again surprising since the flow is so very asymmetric on a frame by frame basis. One can also see that the secondary flow reattaches to the wall at an axial location of about .75D on the left wall and at a distance of about 400 pixels on the right wall.

5.2.2 D) Jet Velocity Ratio, ϕ=19.3

A typical sampling of frames taken from the DPIVC movie of the high Reynolds' number and high swirl number flow with a jet velocity ratio of 19.3 can be seen in Figure 5.13. This figure displays the velocity field of the flow and the vorticity component normal to the plane of the light sheet for the three successive axial locations in the tube.

Looking at the velocity and vorticity fields of this flow reveals that it is substantially similar to the case where ϕ=11.6. Just as in that previous case, the velocity fields of the first axial section suggest that the primary jet and the secondary flow meander together from one side to the other and that this meandering occurs about 4 times during the 3 second movie. The transition from one side to the next occurs quite smoothly, with the flow residing on the left side for about 5-9 frames, in the center of the tube for about 2-3 frames, and then in the right side of the tube for about 9 frames.

59
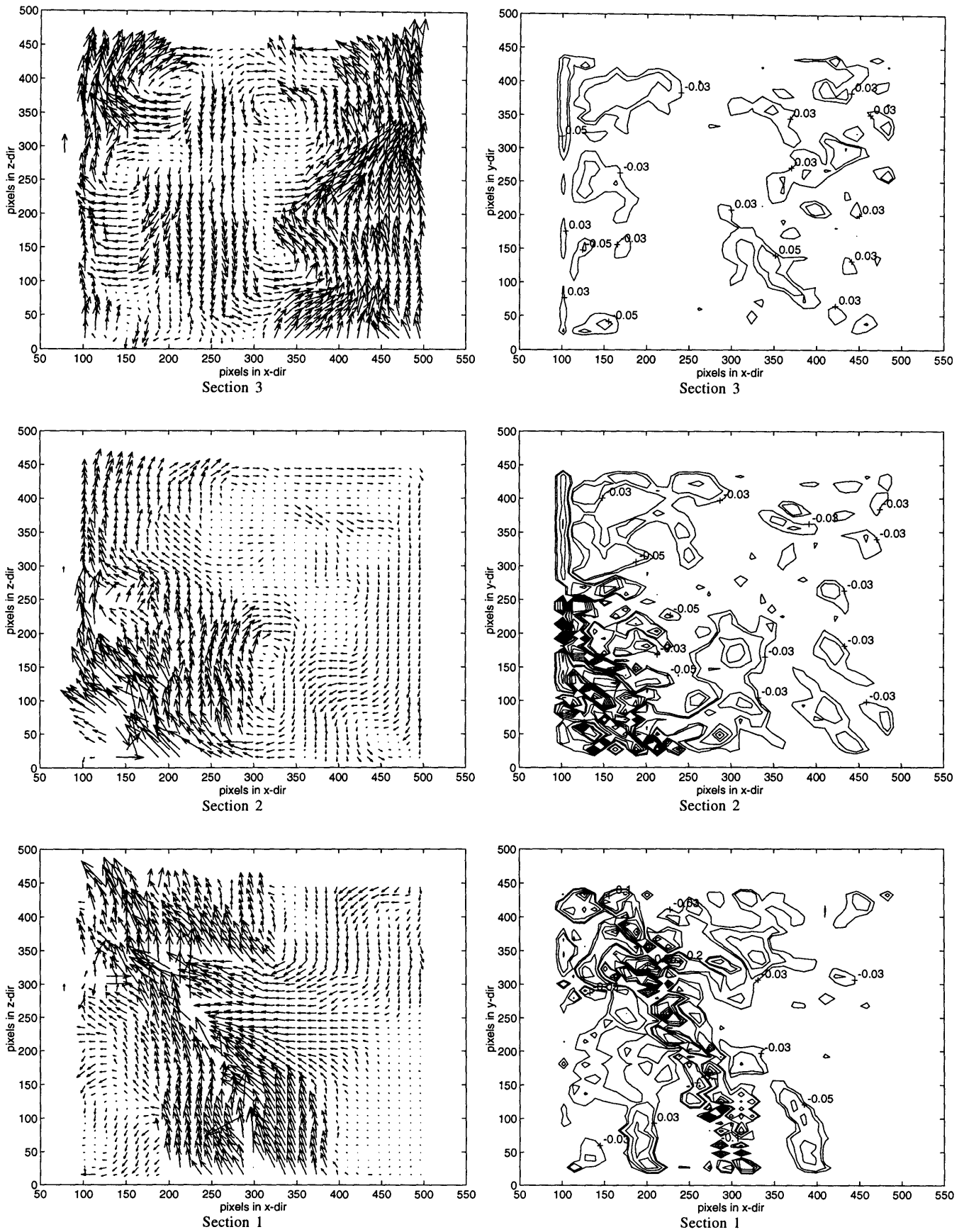
Figure 5.13. Instantaneous Velocity and Vorticity Plots; Re=35,000; S=0.5; φ=19.3. The left column displays the velocity field, the right column displays the vorticity field. All *unmarked* vorticity isocontours have a positive sign.

60
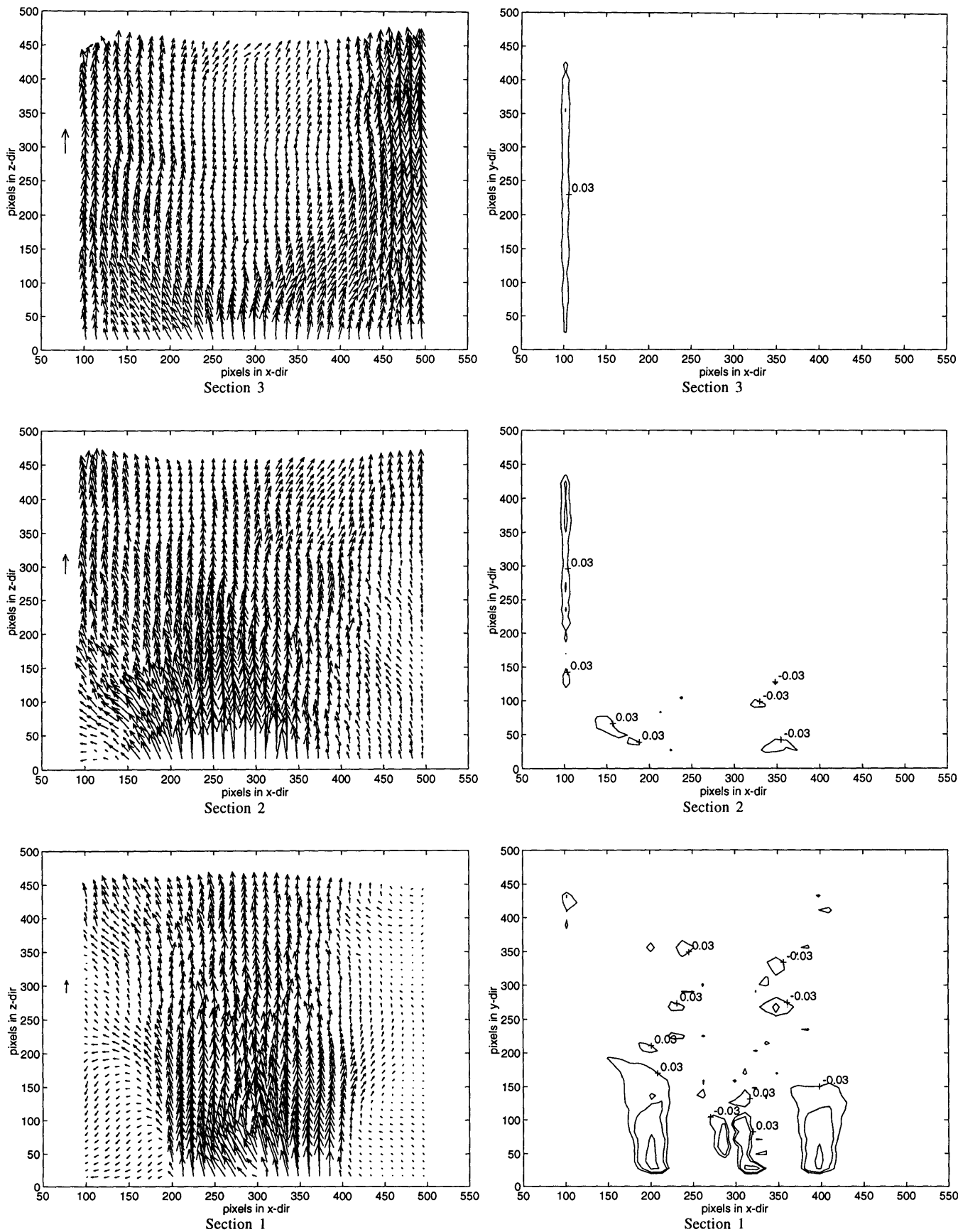
Figure 5.14. Averaged Velocity and Vorticity Plots; Re=35,000; S=0.5; φ=19.3. The left column displays the velocity field, the right column displays the vorticity field. All *unmarked* vorticity isocontours have a positive sign.

61

Once again, the standard recirculation structure is replaced by a structure which seems to divide the tube down the middle of the axis: on one side is the high velocity main flow, and on the other is a low velocity flow which has some counterflow along the walls.

It can be seen that the side of the tube on which the main high velocity flow is predominantly located tends to have a single recirculation zone above the backward facing step. This eddy travels to a maximum axial displacement of about $0.5D$ and this height also corresponds to the reattachment point of the flow. Meanwhile, the side of the tube which is characterized by the low velocity field has several recirculating eddies shedding off of the high speed flow.

The vorticity plots show that the highest vorticity values occur in the region defined by the primary jet. The vorticity structure of the central recirculation zone present in previous cases has completely disappeared, having been dominated by the effect of the jet. The integrated vorticity values for all three axial sections can be seen in Appendix B, Table B.8. These figures show that there is a good correlation between the total positive and negative vorticities, and that the total vorticity in the flow decreases by about 25% from the first to the second section, and by about 40% from the first to the third section. It can also be seen that, in the first section, the left side of the tube is dominated by the positive vorticity while the right side of the tube is dominated by the negative vorticity.

The velocity and vorticity fields averaged over the entire 45 frame DPIVC movie can be seen in Figure 5.14. One can easily see that, just as in the $\phi=11.6$ case, the flow is completely dominated by the jet. All signs of counterflow have completely disappeared from the flow, and the high velocity zone created by the primary jet is felt by the flow all the way up to the top of the third section. The symmetry of the velocity field is also evident in all three axial sections, and this is again surprising since the flow is so very asymmetric on a frame by frame basis.

### 5.2.3 Low Reynolds' Number and Low Swirl Experiments, $Re=11,000$, $S=0.5$
5.2.3 A) Jet Velocity Ratio, $\phi=0.0$

A typical sample of frames taken from the DPIVC movie of the low Reynolds' number and low swirl number flow with a jet velocity ratio of 0.0 can be seen in Figure 5.15. This figure displays the velocity field of the flow and the vorticity component normal to the plane of the light sheet for three successive axial locations in the tube.

The first thing to notice is that the velocity fields obtained from the DPIVC frames have many obviously incorrect vectors as well as many vectors which are missing altogether. These errors seem to be concentrated in areas of high velocities and in areas of large velocity gradients.
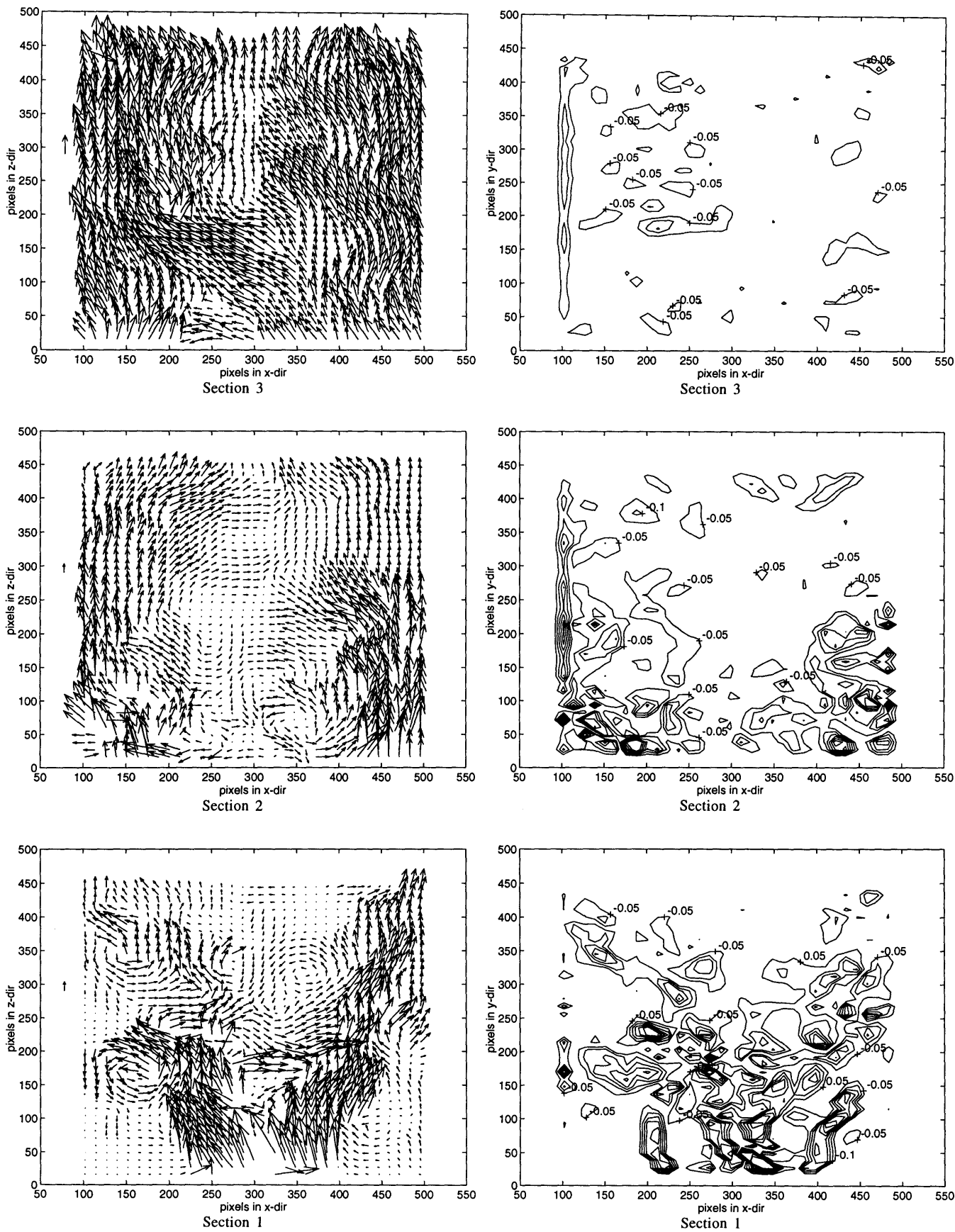
Both the velocity and vorticity fields of this flow show that it is very similar to the equivalent high Re and low swirl number case. In fact, this flow shows the same central recirculation zone and step induced recirculation as that shown by the high Re flow.

The DPIVC movie of the velocity fields taken at the first section reveals that the eddies rising above the left step often rise up to a height of more than 1 D downstream of the inlet before dissipating. Meanwhile, those rising above the right step only rise up to a height of about 3/4 D before disappearing. Both the eddies above the left and the right step seem to form at a height of about $0.25D$. Interestingly, it seems that the only one eddy at a time exists above the right step, while two eddies can often be seen above the left step. The series of frames also suggest that the single eddy on the right remains stable while those on the left rise up and dissipate.

The behavior of the recirculation zone above the right side makes it difficult to describe a shedding frequency for it. On the other hand, a shedding frequency of about once every 7-10 frames can be deduced from the eddies above the left step.

This asymmetric behavior in the step induced shedding results in the secondary flow on the left hand side having a higher wall reattachment point than the secondary flow on the right. In fact, the left hand side reattachment occurs at a height of about $1.0D$ while the reattachment on the right occurs at a height of about $0.6-0.75D$.

The central recirculation zone can be seen to be similar to that of the high Re and low swirl number case. It is difficult to measure the axial extent of this zone in many of the frames due to the fact that the area just above the jet is missing many vectors. However, it nonetheless seems that the central recirculation zone extends from a height of about $1/8-1/4D$ to a height of about $1.2D$ above the flow inlet. This zone varies from one frame to the next, as regions of large horizontal velocities occasionally cut bands across the counter-flowing velocity column. This suggests that the core of the recirculation zone might be moving in and out of the light sheet.

Figure 5.15. Instantaneous Velocity and Vorticity Plots; *Re=11,000* ; *S=0.5; φ=0.0*. The left column displays the velocity field, the right column displays the vorticity field. All *unmarked* vorticity isocontours have a positive sign.

64
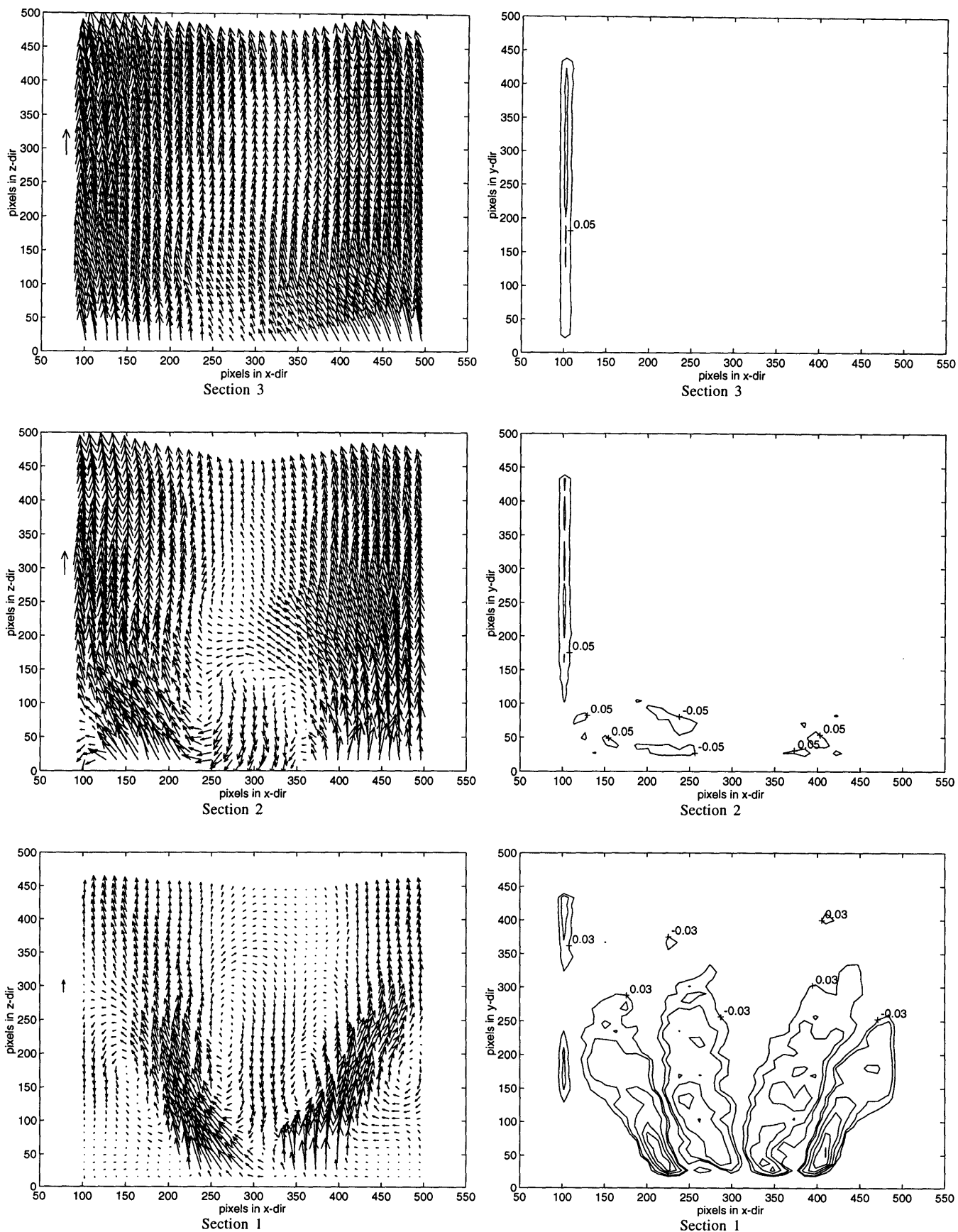
Figure 5.16. Averaged Velocity and Vorticity Plots; Re=11,000 ;
S=0.5; φ=0.0. The left column displays the velocity field, the right
column displays the vorticity field. All *unmarked* vorticity
isocontours have a positive sign.

65

The diameter of the back-flowing column is about 3/16 D just above the jet and the stagnant velocity zone grows to a size of about 1/2 D in the second section. The diameter of this zone then falls until it reaches a size of about 1/4 -1/8 D in the third section.

The vorticity plots of this flow show very similar patterns to the previous cases without any primary jet flow. Once again, the central recirculation zone is characterized by long areas of high negative vorticity on the left side of the axis and long areas of positive vorticity on the right side of the axis. One can see that these two areas have an axial length of about 250-300 pixels. It is also important to notice that these two main areas of vorticity actually have several vorticity peaks within them. The outer step induced recirculation zone, meanwhile, is characterized by regions of positive vorticity on the left side and negative vorticity on the right side. The length of these two areas can be seen to be about 0.5-0.6D.

The values obtained from integrating the vorticity over various areas can be seen in Appendix B, Table B.9, where the mean values over 45 frames are listed for all three sections of the tube. The total positive and negative vorticity integrated over the entire frame have very close absolute values at all three axial locations. It can also be seen that the vorticity in the first section is about 40% larger than in the second section and 64% larger than in the third section. Finally, comparing the circulation values of the left and right hand sides of each frame shows that there is a good correlation between the left side's positive and negative circulation with the right side's negative and positive circulation, respectively. It can also be seen that, for all three axial locations, the left side has a net negative circulation while the right side has a net positive circulation.

The velocity and vorticity fields averaged over the entire 45 frame DPIVC movie can be seen in Figure 5.16, which shows that all three sections show a remarkable amount of axial symmetry. The first section's velocity field clearly shows the reattachment points of the left and right secondary flow branches as well as the height reached by the step induced recirculation zones. This height is about .44D for both the left and the right sides of the tube.

A straight column of counter flow about 1.3 D in length can be seen at the center of the tube, starting from a height of about 1/8 D above the inlet. Interestingly, the vorticity field of the first section shows that the central vorticity islands have 4 peaks. Looking closely at the velocity field of the second section, one can again see a wake like velocity

66
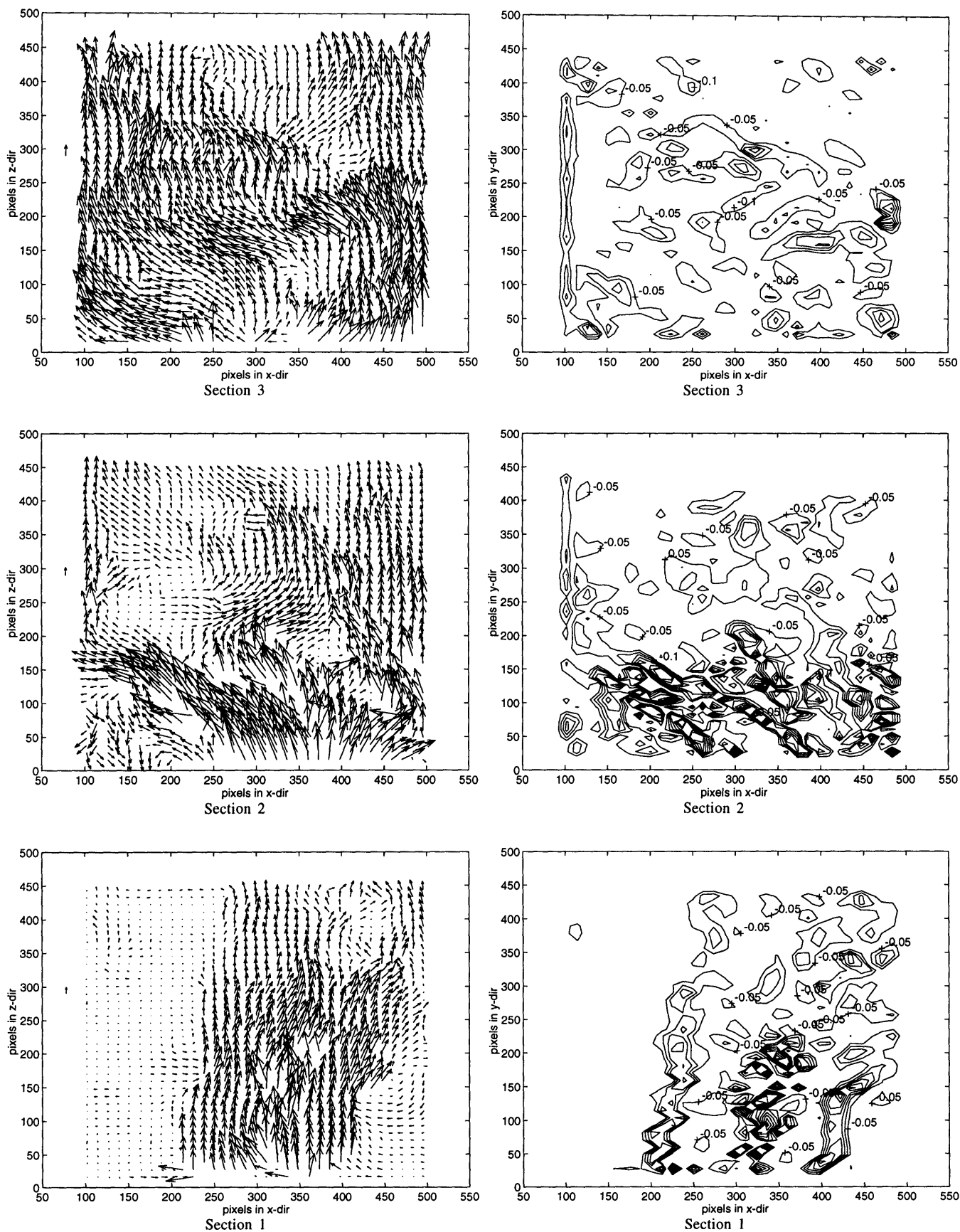
Figure 5.17. Instantaneous Velocity and Vorticity Plots; *Re=11,000* ; *S=0.5; φ=8.6.* The left column displays the velocity field, the right column displays the vorticity field. All *unmarked* vorticity isocontours have a positive sign.

67
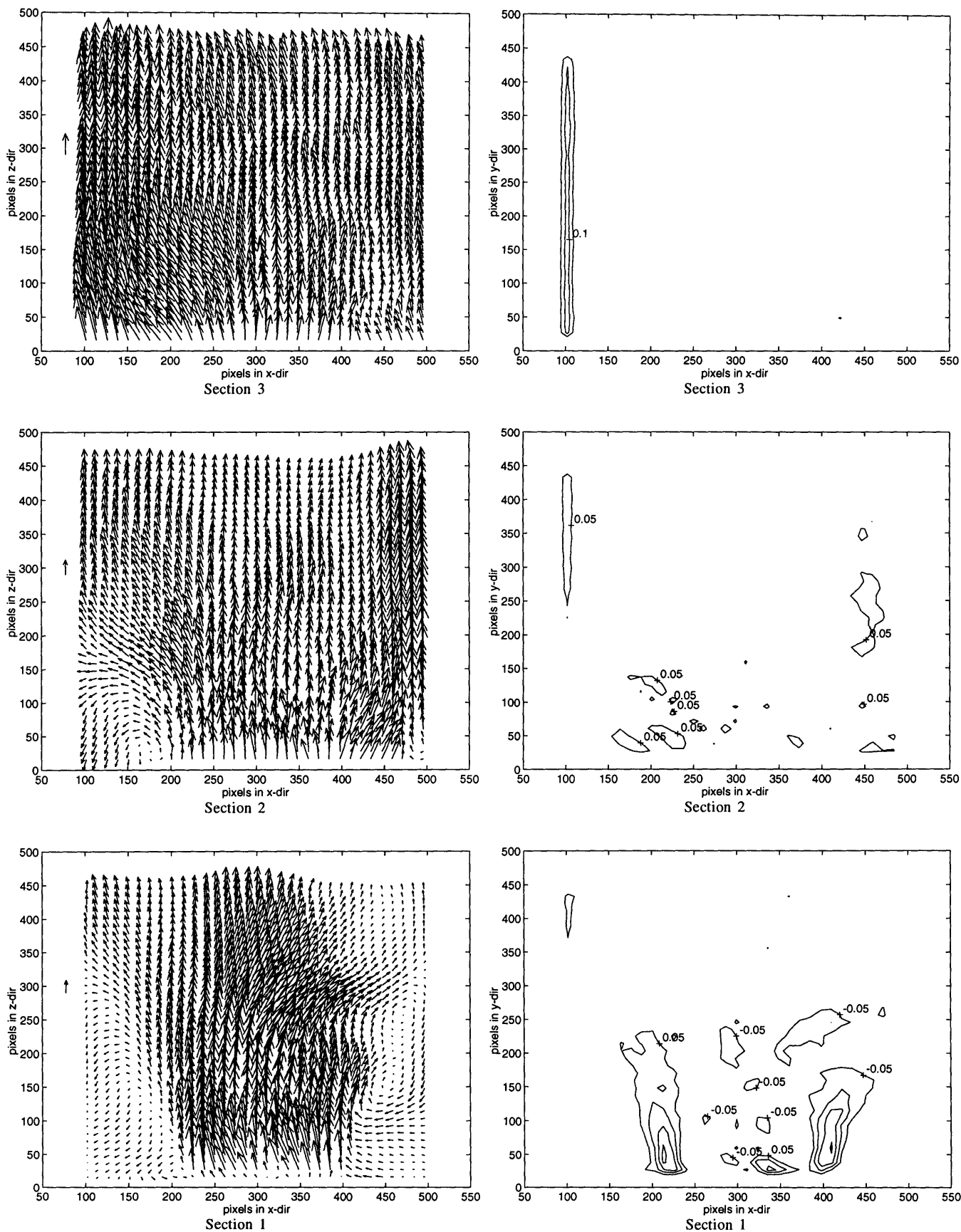
Figure 5.18. Averaged Velocity and Vorticity Plots; Re=11,000 ; S=0.5; φ=8.6. The left column displays the velocity field, the right column displays the vorticity field. All *unmarked* vorticity isocontours have a positive sign.

68

deficit at the center of the tube. This deficit becomes smaller in the flow direction and has practically disappeared by the top of the third section.

5.2.3 B) Jet Velocity Ratio, ϕ=8.6

A typical sampling of frames taken from the DPIVC movies of the low Reynolds' number and low swirl number flow with a jet velocity ratio of 8.6 can be seen in Figure 5.17. This figure displays the velocity field of the flow and the vorticity component normal to the plane of the light sheet for the three successive axial locations in the tube.

Looking at the velocity and vorticity fields of this flow reveals that it is substantially similar to the high ϕ cases seen previously. In fact, the velocity fields of the first axial section suggest that the jet entrains the secondary flow with it. The complete 45 frame DPIVC movie shows that this combined high velocity flow oscillates from one side of the tube to the other and that this meandering occurs only once. The transition from one side to the next occurs quite smoothly, with the flow residing on the right side for about 24 frames, in the center of the tube for about 4 frames, and then in the left side of the tube for about 17 frames.

The presence of this meandering high velocity flow has a profound effect on the surrounding velocity and vorticity fields. The frames taken in the first section show that the flow structure composed of a central recirculation zone and of a step induced recirculation zone has all but disappeared. In its place is a structure which seems to divide the tube down the middle of the axis: on one side is the high velocity main flow, and on the other is a low velocity flow which even has some counterflow along the walls.

It can be seen that the side of the tube on which the main high velocity flow is predominantly located tends to have at most two recirculation zones above the backward facing step. It can also be seen that these eddies are directly adjacent to the wall and that they travel to a maximum axial displacement of about .88D, which is also the height of the reattachment point of the high speed flow. Meanwhile, the side of the tube which is characterized by the low velocity field has several recirculating eddies as well as a counter-flowing region adjacent to the wall.

The vorticity plots show that the highest vorticity values occur in the region defined by the primary jet. The vorticity structure of the central recirculation zone present in previous cases has completely disappeared, having been dominated by the effect of the jet.

The integrated vorticity values for all three axial sections can be seen in Appendix

B, Table B.10. These numbers show that there is a good correlation between the total positive and negative vorticities, and that the total vorticity in the flow remains constant or actually increases slightly from the first section to the second. The circulation in the third section is about 30% less than the circulation in the first section. It can also be seen that, in all three sections, the left hand side is dominated by the positive vorticity while the right hand side is dominated by the negative vorticity.

The velocity and vorticity fields averaged over the entire 45 frame DPIVC movie can be seen in Figure 5.18. One can easily see that, just as in the previous high ϕ experiments, the flow is completely dominated by the jet. All signs of counterflow have completely disappeared, and the high velocity zone created by the primary jet is felt by the flow all the way up to the bottom of the third section. The symmetry of the velocity field is also evident in all three axial sections, and this is again surprising since the flow is so very asymmetric on a frame by frame basis.

5.2.4 Flow Rate Calculations Based on Velocity Plots

The actual flow rates and those calculated from the velocity plots for two flow conditions are shown in Table 5.1. It can be seen that the calculated flow rates are of the same order of magnitude as the actual values, but are consistently lower than the latter. In fact, the deficit between the calculated values and the actual flow rates ranges from 15% to 50%.

Looking at the calculated flow rates for each of the three sections reveals an interesting trend: for a given actual flow rate, the calculated flow rate increases from the first to the third section. Indeed, for the two cases investigated, the difference between the calculated flow rate in the first and third sections is 31% and 60%.

	Calculated Flow Rate for Re=34,000, S=2.0 (m³/s)	Actual Flow Rate for Re=34,000, S=2.0 (m³/s)	Calculated Flow Rate for Re=35,000, S=0.5 (m³/s)	Actual Flow Rate for Re=35,000, S=0.5 (m³/s)
Section 1	1.30×10^{-3}	2.74×10^{-3}	1.50×10^{-3}	2.85×10^{-3}
Section 2	1.60×10^{-3}	2.74×10^{-3}	1.90×10^{-3}	2.85×10^{-3}
Section 3	1.70×10^{-3}	2.74×10^{-3}	2.40×10^{-3}	2.85×10^{-3}

Table 5.1. Comparison of Calculated and Actual Flow Rates for Two Base Flows.

5.3 Summary of Major Results

The major quantifiable results are summarized in this section. Table 5.2 lists the main results obtained from the basic flows (ie: those in which the primary jet was turned off), and Table 5.3 lists the main results for the flows in which a primary flow was present.

	$S=2.0$; $Re=34,000$	$S=0.5$; $Re=35,000$	$S=0.5$; $Re=11,000$
Axial Extent of Central Recirculation Zone (in Tube Diameters))	~6	1.3	1.3
Average Reattachment Point of Secondary Flow (in Tube Diameters)	0.5	0.5	0.44
Step Vortex Shedding Frequency (Hz)	2	2	1.5
Number of Vorticity Peaks in Central Recirculation Zone of Instantaneous Fields (in the First Axial Section)	6-7 pairs	5-6 pairs	5-6 pairs
Number of Vorticity Peaks in Central Recirculation Zone of Averaged Fields (in the First Axial Section)	2-3 pairs	1-2 pairs	1-2 pairs

Table 5.2. Summary of Major Results for Flows Without a Primary Jet

	Effect On CRZ	**Oscillation Frequency (Hz)**
$Re=34,000$, $S=2.0$		
$\phi= 4.0$	None	-
$\phi=12.0$	Strongly Modified	-
$\phi=20.0$	Eliminated	1
$Re=35,000$, $S=0.5$		
$\phi= 3.9$	None	-
$\phi=11.6$	Eliminated	0.6
$\phi=19.3$	Eliminated	0.6
$Re=11,000$, $S=0.5$		
$\phi= 8.6$	Eliminated	0.3

Table 5.3. Summary of Major Results for Flows With a Primary Jet.

71

CHAPTER 6

Discussion

This chapter begins with a quick explanation of why the experiments involving the azimuthal cross sections did not work very well. The major part of the chapter, however, involves using the two dimensional velocity and vorticity plots obtained from the longitudinal cross sections (and the calculations based on them) to construct a three dimensional model of the vortex breakdown phenomena encountered in the investigated flows. Finally, an estimation of the major sources of error in the experiment is also presented.
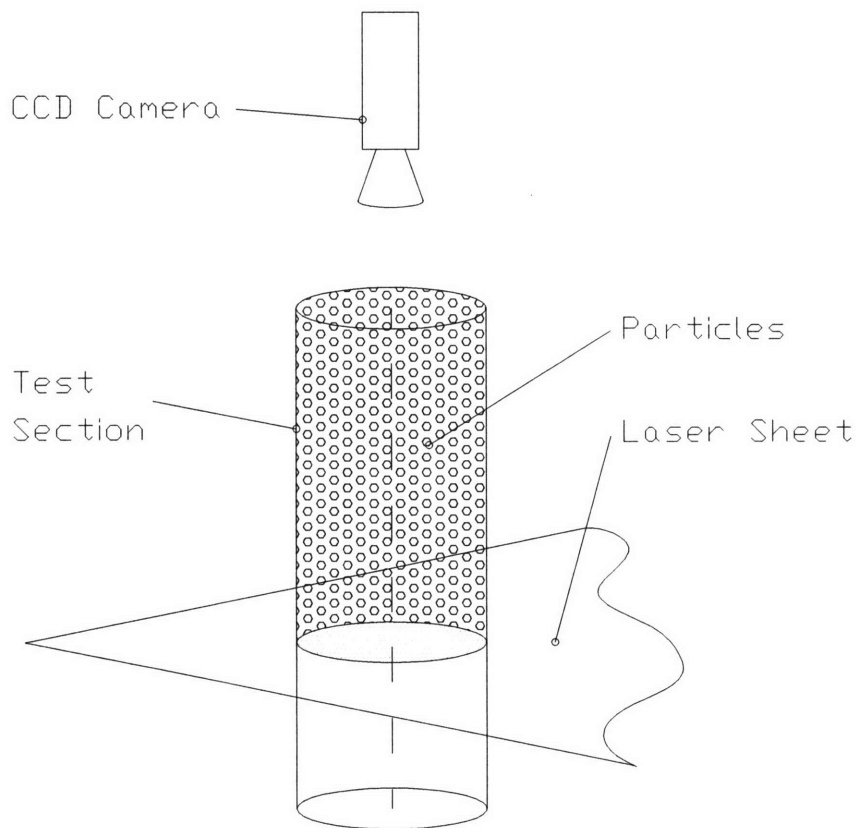
6.1 Analysis of the Azimuthal Cross Section Experiments

The low quality velocity fields obtained from the azimuthal cross section images is most probably due to the flow's high tracer seeding density and to the considerable distance between the CCD camera and the laser light sheet. These two factors combine to make it very difficult for the light reflected by the particles within the light sheet to reach the camera.

The reason for this becomes obvious by looking at Figure 6.1, which shows a schematic of the experimental setup. Clearly, as the tracer seeding density and the distance between the camera and the light plane is increased, a larger fraction of the light emitted by the particles in the light sheet will be absorbed and scattered away by the particles located in between the plane and the camera.

This effect has important implications for the use of DPIVC under these kinds of conditions, since it shows that a given separation distance between the camera and the light sheet has associated with it a maximum particle seeding density. This critical density cannot be surpassed without the loss of optical clarity and, as was explained in Section 2.6, this maximum seeding density also limits the resolution of the flow measurement itself.

Figure 6.1. Schematic of Setup for Azimuthal Imaging.

6.2 Analysis of the Longitudinal Cross Section Experiments

This section is divided into eight major topics: a brief description of the relevant aspects of vorticity theory, an analysis of the features of the baseline flows, a description of the primary jet's effects on the base flow, an investigation of the peculiar aspects of each of the three major flow groups, an analysis of the vortex shedding results and a study of the flow rate calculations. The assumptions and limitations of the utilized techniques are also discussed throughout the chapter.

6.2.1 Vorticity Theory

By definition, the vorticity vector is the curl of the velocity vector, and is therefore divergence free:

$$\nabla \cdot \vec{\omega} = 0 \tag{6.1}$$

One can integrate equation (6.1) over a finite volume, V, and the divergence theorem can then be applied:

$$\int_V \nabla \cdot \vec{\omega} dV = 0$$

$$\Rightarrow \int_S \vec{\omega} \cdot \vec{n} dS = 0 \qquad (6.2)$$

where S is the surface bounding V, and $\vec{n}$ is the outward normal to that surface.

Defining a *vortex line* to be a line which is everywhere tangent to the local vorticity vector, one can imagine a *vortex tube* as a set of vortex lines passing through a connected surface in space.
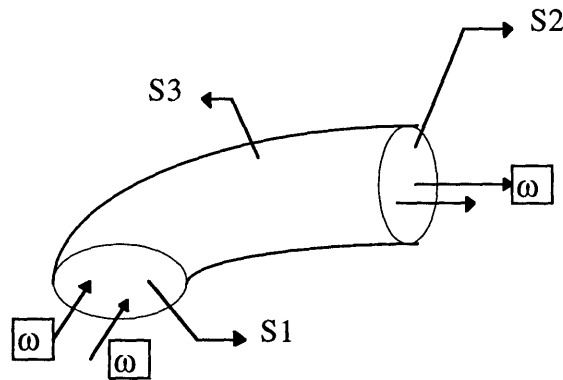
Figure 6.2. Vortex Lines and Vortex Tube.

One can see from Figure 6.2 that the integration of $\vec{\omega} \cdot \vec{n}$ over S3 is equal to zero, and that:

$$\int_{S_1} \vec{\omega} \cdot \vec{n} dS + \int_{S_2} \vec{\omega} \cdot \vec{n} dS = 0 \qquad (6.3)$$

Using the definition of circulation, this leads to:

$$\Gamma_2 - \Gamma_1 = 0$$

$$\Gamma_1 = \Gamma_2 \qquad (6.4)$$

This result is known as Helmholtz's first vortex law. This law states that the circulation around a vortex tube is constant, and implies that vortex tubes cannot terminate within a fluid since this would result in having different circulation values at different locations along the tube. Because of this last fact, vortex tubes are forced to either form loops within the fluid or must terminate either at a wall or at a fluid-fluid interface.

6.2.2 Structural Model of Vortex Breakdown Flows

This section develops two three dimensional models describing the structure of the basic breakdown flows (i.e.: those in which the primary jet is shut off): the first is based on the instantaneous velocity and vorticity plots, and the second is based on the averaged velocity and vorticity plots. It is important to notice that the second model is equivalent to a model that would be developed from and LDA investigation of the flow. Finally, the last part of this section compares and contrasts the two structural models.

6.2.2 A) Model Based on Instantaneous Fields

The baseline flows in which the primary jet did not play a significant role all exhibit the same major features: the step induced recirculation zone (SIRZ) and the central recirculation zone (CRZ). An important aspect of these two features is that they are both somewhat symmetrical about the tube's axis. Looking specifically at the step induced recirculation zones, one can see that the eddies rising above the left step are rotating in a counter-clockwise direction, while the eddies rising above the right step are rotating in a clockwise direction. The central recirculation zone, meanwhile, can be seen to have eddies spinning counter-clockwise on the right side of the tube axis and eddies spinning clockwise on the left side of the tube axis. The vorticity plots reveal that the counter clockwise spinning eddies correspond to regions of positive vorticity while the clockwise spinning eddies correspond to regions of negative vorticity.

The fact that this pattern shows up in every frame of a given DPIVC movie combined with the fact that the flow is swirling suggests that these eddies are located at all angular positions in the tube. Furthermore, the fact that these circulation areas cannot end in the fluid due to Helmholtz's law makes two things very likely: first, that the step induced vorticity islands on one side of the axis are connected in three dimensions to the step induced vorticity islands on the other side of the axis, and second, that the CRZ vorticity islands on one side of the axis are connected in three dimensions to the CRZ vorticity islands on the other side of the axis.

The idea that the CRZ and SIRZ are three dimensional structures is reinforced by looking at the results of the vorticity integration calculations (Appendix A). These calculations show that the positive circulation on the left side of the tube has a very similar absolute value to the negative circulation on the right side of the tube. Since the velocity and vorticity plots for all these flows show that the positive circulation area on the left and

the negative circulation on the right are associated with the step induced recirculation zone, it can be concluded that the two sides of this recirculation zone are indeed connected by some sort of vortex tube. Similarly, the closeness of the absolute values of the negative circulation on the left side of the tube and the positive circulation on the right side of the tube suggest that the left and right sides of the central recirculation zone are also connected in three dimensions.

The integration of the vorticity over the entire area of the tube's cross section, meanwhile, shows that the positive and negative components of the circulation have the same absolute value, implying that the net circulation in the azimuthal direction is zero. This result supports the validity of the data because there should be little net azimuthal vorticity in the flow since no azimuthal vorticity entered the test section at the inlet. Of course, some vorticity is being generated inside the flow near the walls and in the high shear areas of the CRZ, but the flow's near symmetry about the axis insures that these sources' positive and negative components sum to zero.

The most likely three dimensional structures that would satisfy Helmholz's law and the patterns shown by both the SIRZ and the CRZ are a closed toroidal line of vorticity and an open spiral line of vorticity. Unfortunately, the visualization of only one plane of the flow makes it impossible to determine with certainty which of these two structures is present. Careful analysis of the flows' velocity and vorticity plots does point to the most likely structures, however.

By looking closely at the SIRZ in the velocity field plots of any of the investigated flows, evidence can be found that this recirculation zone consists of a line of azimuthal vorticity spiraling up from the backward facing step. In fact, many frame sequences show a strong eddy above one step, and one strong eddy and a weaker one downstream of it above the other step. It can also be seen that these three eddies are often staggered, with an axial distance on the order of one eddy diameter in between them. It might be that these eddies are part of a structure consisting of two or more independent toroids angled to the axis. However, this would imply that the downstream toroid is being unevenly dissipated since only one of its ends is strong enough to be visible. It seems much more likely, therefore, that the eddies are part of a single spiral vortex tube which is rising up from the step annulus and whose strength is being gradually dissipated until the "tail" is so weak that it becomes unobservable.

The flow patterns of the central recirculation zone, meanwhile, suggest that it too is composed of a spiral vortex line. In fact, none of the instantaneous velocity fields point to the simple, clear structure of a breakdown bubble (i.e.: one or two pairs of counter rotating eddies joined together by a toroid of vorticity) described by previous investigations of low and high Re flows. Instead, the central recirculation zones observed in this research always contain more than 3 pairs of vorticity peaks staggered around the axis. This pattern of vorticity traces could be explained by the presence of 3 or more toroids tilted at similar angles to the axis. However, it seems much more likely that these islands of vorticity are threaded together in three dimensions by a single line of vorticity spiraling its way up from the inlet. By the Biot-Savart law, this spiral line of azimuthal vorticity is then responsible for convecting the fluid in the central part of the tube against the main flow direction (as was explained in Section 1.3).

A final argument against the presence of several toroids of vorticity is based on mass conservation arguments. Two vortex rings of equal strength and diameter cannot remain separated by a short distance since the mass flow rate through the upstream ring would have to be larger than in the downstream ring.

6.2.2 B) Model Based on Averaged Fields

Generally speaking, all of the arguments presented in the previous section also apply to the averaged velocity and vorticity fields. For instance, the correlation of the absolute values of circulation of the inner and outer recirculation zones also suggest a three dimensional structure in this second model. However, looking closely at the averaged fields shows that they are visibly different from the instantaneous fields. Indeed, one can see that the average vorticity plots of the first section show that there are only 1-2 pairs of strong vorticity peaks in the CRZ, compared to the 3 or more found in the instantaneous vorticity plots. This small number of vorticity zones therefore suggests the presence of one or two toroids of azimuthal vorticity instead of a spiral line of azimuthal vorticity. The SIRZ, meanwhile, can be seen to have a single large eddy above each step, suggesting that this recirculation zone is also made up of a single toroid of azimuthal vorticity.

6.2.2 C) Comparison of Both Models

The selection of the correct model can only be made after finding out why the number of vorticity peaks falls when the instantaneous fields are averaged. One possible

explanation for this effect is that the extra peaks in the instantaneous fields are just manifestations of random noise and turbulent effects which cancel out when averaged over the 45 frames. If this is the case, then the model based on the averaged fields is probably correct.

However, if the extra vorticity peaks found in the instantaneous fields were truly caused by random effects, they would not show the regular structure described in the Results chapter. For example, the vorticity islands nearest to the axis on the left side of the tube would not all have a negative value if their presence was due only to random velocity fluctuations. This argument suggests that instead of being an effect of noise, the reduction in the number of vorticity zones in the averaged fields is due to the averaging process itself. In fact, it is likely that the latter decreases the influence of those vorticity traces which are highly mobile from frame to frame. These peaks, whose motion could be due to the rotation of the spiral CRZ structure and to the turbulent nature of the flow, therefore disappear in the averaged plot and leave behind only those vorticity zones whose location is more stable.

This explanation implies that the averaging process removes information from the flow, and that any model based on the averaged velocity and vector fields is probably oversimplified. The model based on the instantaneous fields can therefore be considered as the more accurate of the two.

It is important to realize that even though the vorticity peaks found in the instantaneous fields are not caused by random fluctuations, other turbulent effects are occurring within the flow. For example, it is probable that the appearing and disappearing of the counter-flowing column from the frames is due to turbulent effects deforming the vortex core in and out of the light sheet plane.[1] Furthermore, the symmetry of the averaged velocity and vorticity fields shows that these random fluctuations do average out to zero.

6.2.3 Interaction of SIRZ and CRZ
The spiral model of both recirculation zones allows one to explain the observation that the step induced recirculation zone disappears a short distance downstream of the inlet. The values of circulation calculated from the vorticity plots of the flows with negligible

---

[1] It could also be argued that this phenomena is due to the meandering of the vortex core about the tube axis. However, this hypothesis is weakened by the fact that the oscillations occur at frequencies which are very much higher than the azimuthal rotation frequency of the investigated flows.

primary flows all show that the circulation of the CRZ is stronger than the circulation of the SIRZ. It is therefore probable that the latter's line of azimuthal vorticity is gradually nullified by the CRZ's stronger (and opposite) line of vorticity.

Another factor affecting the axial displacement of the step induced eddies is the spreading of the secondary flow. At high swirl numbers, the latter's centrifugal acceleration makes it reattach to the walls very quickly, thereby limiting the movement of the eddies. At low swirl numbers, on the other hand, the lower centrifugal acceleration causes the secondary flow to reattach to the wall at a position further downstream, thereby allowing the eddies to travel further.

6.2.4 Effect of Primary Jet on the Vortex Breakdown

As was described in the Results section, the effect of a strong primary jet is to reduce the size of the CRZ, or to remove it completely. The primary jet accomplishes this in two ways: first, it reduces the adverse pressure gradient along the axis (which was shown to be critical to the formation and strength of a breakdown in Chapter 1), and second, it creates an azimuthal vorticity structure whose sign is opposite to the breakdown's own vorticity structure. Because of this sign difference, the jet's vorticity structure weakens or cancels out that of the CRZ.

The two dimensional vorticity plots show that the jet's vorticity structure is located directly around it and is composed of a positive vorticity region on the left of the jet flow and a negative vorticity region on the right of the jet flow. These two regions are most probably connected in three dimensions by a toroid or by a spiral and are created by the shear layer located in between the high velocity jet and the surrounding secondary flow.

The importance of this jet recirculation zone (JRZ) can be seen in the results of the vorticity integration calculations (Appendix A). These results show that the combination of the JRZ and SIRZ circulation values (represented by the positive circulation on the left side and the negative circulation on the right side) surpasses the value of the circulation caused by the central recirculation zone (CRZ) as ϕ increases. It can be seen from the velocity fields that the counter-flowing region at the axis disappears when this occurs. Furthermore, the results also show that flows with larger values of swirl require a higher ϕ value for the complete disappearance of the CRZ to occur.

Finally, it can be seen that the jet and the secondary flow begin to oscillate about the axis of the tube when ϕ reaches a critical value. The results show that this critical value of

φ decreases as S decreases, suggesting that the confined jet flow is stabilized by high swirl and is destabilized by a high velocity ratio.

With this general description of the structure of the major aspects of the investigated flows, the three major types of flows can be scrutinized individually.

6.2.5 High Reynolds' Number and High Swirl Number Experiments; $Re=34,000$, $S=2.0$
6.2.5 A) Jet Velocity Ratio, $\phi=0.0$

As was described in the results section (section 5.2.1A), this flow field is characterized by a strong central recirculation zone whose axial extent is longer than the 3.0D investigated. This flow can therefore be considered to be the extreme form of vortex breakdown, as described by Harvey [5].

Looking carefully at the SIRZ reveals that the formation and replacement of an eddy occurs every 7-8 frames or so, corresponding to a frequency of about 1-2 Hz.

It is important to realize, however, that this result is contingent on the characteristic time of this flow pattern being longer than 1/15 of a second, since this is the time interval between velocity plots. Since a feature moving at the average speed of the flow would travel about 100 pixels in this time interval, the result is only correct if the eddies above the step move downstream at a much slower velocity than the average flow velocity. The quantification of the shedding is further complicated by the fact that the flow is also moving through the light plane at high speed.

The averaged velocity fields of the second and third sections are particularly interesting. They show the presence of large eddies spinning clockwise on the left of the axis and spinning counter clockwise on the right of the axis. This surprising behavior might be explained if there is a spiral vortex line going in and out of the plane whose rotation frequency is such that its trace lies within a narrow axial range from one frame to the other.

6.2.5 B) Jet Velocity Ratio, $\phi=4.0$

The results from this experiment, (section 5.2.1B), are almost identical to those obtained in the φ=0.0 case, indicating that this low velocity jet has a negligible influence on the structure of the breakdown flow. This is not too surprising since the velocity ratio between the jet and the secondary flow at the inlet is really only 2.0 because of the constriction ratio of two in the converging nozzle. The addition of this jet flow is therefore

akin to simply removing the velocity deficit caused by the central hub from the secondary flow.

The only major difference between this flow and the previous one is that the shedding frequency in this flow is not easily decipherable. This is partly due to the fact that the resolution of the images was reduced by 13% due to an error in the setting up of the camera, so that it is harder to distinguish when eddies are just beginning to form above the step.

6.2.5 C) Jet Velocity Ratio, $\phi=12.0$

Unlike the previous experiment, the jet in this flow has a strong influence on the vortex breakdown. In fact, the results indicate that it pierces through the central recirculation zone and reduces its size considerably (section 5.2.1C).

The central region of the first axial section is dominated by the high velocities caused by the jet. The correlation algorithm has problems with these high velocities and large gradients, so that there are many blank areas and incorrect vectors in this region. This makes it difficult to track the exact whereabouts of the jet, but the entire DPIVC movie strongly suggests that it remains along the axis of the tube.

What is certain is the fact that the counter flowing column at the axis has completely disappeared from the second and third sections of the tube. What is left of the flow reversal region is wrapped around the primary jet and only extends for about 1/4D downstream of the inlet. As was described above, this effect is due to the JRZ becoming as strong as the CRZ.

6.2.5 D) Jet Velocity Ratio, $\phi=20.0$

This flow is dramatically different than the $\phi=0.0$, $\phi=4.0$, and $\phi=12.0$ cases. The results (section 5.2.1D) suggest that the primary jet entrains the secondary flow and that their combined flow oscillates around the axis of the tube at a frequency of about 1 Hz. This behavior suggests that there is some critical ϕ between 12.0 and 20.0 where the primary jet flow becomes unstable and transitions from a straight jet to one which begins to rotate about the axis of the tube.

It is quite obvious that the CRZ of the previous experiments has completely disappeared in this flow. It is interesting, however, that for an axial distance of about 1.5-2.0D downstream of the inlet, the flow has a rotating structure characterized on one side by

81

a violent, high speed flow and characterized on the other side by very low velocities and even some counterflow along the wall.

The axisymmetry of the velocity fields averaged over the entire 45 frame DPIVC movie confirms the idea that the oscillatory behavior of the flow is periodic.

6.2.6 High Reynolds' Number and Low Swirl Number Experiments; $Re=35,000$, $S=0.5$

6.2.6 A) Jet Velocity Ratio, $\phi=0.0$

As was described in the results section 5.2.2A, this flow field is characterized by a central recirculation region whose axial extent is about 1.3D. This flow can therefore be considered to be one of the more classic turbulent bubble-type breakdowns . The velocity and vorticity plots reveal the presence of several eddies driving the flow downwards in the first and second axial sections of the tube.

Interestingly, the location of SIRZ eddies is further downstream then in the high swirl number experiments. As was mentioned earlier, this is probably due to the lower swirl number's two main effects: the reduction of the circulation in the CRZ and the higher secondary flow reattachment point allowed by the lower centrifugal forces.

The movements of the step induced eddies are somewhat enigmatic once again, but many frame sequences do suggest that their shedding frequency is about 2 Hz.

The average velocity plot of the second axial section, meanwhile, looks very much like a wake. A velocity deficit can be seen at and around the centerline, and this can be explained by the fact that the CRZ in the first section acts very much like a bluff body obstructing the flow. The velocity deficit decreases axially because of diffusion, and the flow becomes very uniform by the top of the third section.

6.2.6 B) Jet Velocity Ratio, $\phi=3.9$

The results from this experiment (section 5.2.2B) are almost identical to those obtained in the $\phi=0.0$ case, indicating once again that this low velocity jet has a negligible influence on the structure of the breakdown. Just as in the equivalent experiment with high swirl, this can be explained by the fact the velocity ratio between the jet and the secondary flow at the inlet is really only 1.8. The addition of the jet flow is therefore akin to simply removing the secondary flow's velocity deficit caused by the central hub.

Once again, an exact shedding frequency for the eddies in the SIRZ cannot be calculated due to their erratic displacements from frame to frame.

6.2.6 C) Jet Velocity Ratio, $\phi=11.6$

As was described in the results section 5.2.2C, this flow field is dominated by the effects of the primary jet. Just as in the $\phi=20.0$ case in the high swirl experiment, the vortex breakdown structure is replaced by a rotating structure in which half of the tube is filled with a high velocity flow created by the primary jet's entrainment of the secondary flow, and in which the other half of the tube is filled with a stagnant flow. This structure is most evident in the first section of the axis, but is noticeable in the third section as well. It can be seen, however, that momentum diffusion evens out the overall flow as the distance from the inlet increases.

The whole flow structure rotates around the axis at a frequency of about 0.6 Hz throughout the entire investigated length of the tube. This behavior suggests that there is some critical ϕ value between 3.9 and 11.6 where the jet flow becomes unstable and changes from a straight jet to one which begins to rotate about the axis of the tube. Comparing this interval to the one encountered in the $S=2.0$ case reveals that the critical ϕ number decreases as S decreases.

The averaged velocity and vorticity plots once again show the difficulties encountered when using averaging measurement techniques such as LDA. In fact, both the velocity and vorticity fields are pretty much axisymmetric, and completely hide the asymmetry of the revolving flow structure. This symmetric result is nonetheless quite interesting since it confirms the fact that the structure's rotation is regular.

6.2.6 D) Jet Velocity Ratio, $\phi=19.3$

This flow is substantially the same as the flow with $\phi=11.6$. The most interesting aspect of this flow is the fact that the rotation frequency of the flow structure is the same as in the $\phi=11.6$ case (0.6 Hz), suggesting that once this kind of flow is established, the jet velocity ratio does not affect the oscillation frequency (see section 5.2.2D)

6.2.7 Low Reynolds' Number and Low Swirl Number Experiments; $Re=11,000$, $S=0.5$
6.2.7 A) Jet Velocity Ratio, $\phi=0.0$

As was described in the results section 5.2.3A, this flow field is characterized by a central recirculation region whose axial extent is about 1.1D.

Interestingly, the location of the SIRZ eddies is further downstream then in the high swirl number experiments. As was mentioned earlier, this is probably due to the lower swirl number's two main effects: the reduction of circulation in the CRZ and the higher secondary flow reattachment point allowed by the lower centrifugal forces.

The movements of the SIRZ eddies in between frames are somewhat enigmatic since a shedding frequency can only be calculated for the left side of the flow. The eddies above this step seem to shed every 7-10 frames or so, which corresponds to a shedding frequency of about 1.5 Hz. This value is probably more reliable than those reported for the high Re experiments since the average axial displacement in this set of experiments is only about 30 pixels, and the azimuthal displacements are small as well. Indeed, many sequences in these velocity plots seem to track the shedding eddies very well.

The average velocity fields show that there is little difference between the secondary flow's reattachment point in this case and the reattachment point of the high Re, low S case. This suggests that the dominant influence on this feature is the Swirl number and not the axial momentum of the secondary flow. The average velocity plot of the second axial section, meanwhile, looks very much like a wake since there is a velocity deficit around the centerline. This is explained by the fact that the CRZ in the first section acts very much like a bluff body obstructing the flow. The velocity deficit decreases axially because of momentum diffusion, and the flow becomes very uniform by the top of the third section.

6.2.7 B) Jet Velocity Ratio, $\phi=8.6$

As was described in the results section 5.2.3B, this flow field is dominated by the effects of the primary jet. Just as in the high ϕ cases in the previous Re and S experiments, the vortex breakdown structure is replaced by a rotating structure in which half of the tube is filled with a high velocity flow created by the primary jet's entrainment of the secondary flow, and in which the other half of the tube is filled with a stagnant flow.

This structure is most evident in the first section of the axis, but it is still noticeable in the third section as well despite the fact that momentum diffusion has evened out the overall flow. The whole flow structure rotates around the axis at a frequency of about 0.3 Hz throughout the entire investigated length of the tube. This value is only half as large as the frequencies found in the similar high Reynolds' number cases, but it should be noticed that this frequency is more unreliable than the former since the high velocity flow in this case only oscillates once within the 3 second DPIVC movie.

The jet's behavior suggests that there is some critical ϕ value between 0.0 and 8.6 where it becomes unstable and changes from a straight jet to one which begins to rotate about the axis of the tube. This interval is similar to that found in the Re=35,000 and S=0.5 experiments.

The integrated vorticity values (Appendix B) show that, in the first axial section, the circulation created by the jet and by the SIRZ is about 2 times greater than the circulation driving the CRZ. The latter circulation is therefore too weak to create a counterflow at the axis.

Finally, the symmetry of the averaged velocity and vorticity plots confirms the fact that the structure's rotation is regular.

6.2.8 Step Induced Vortex Shedding

As was shown above, the velocity and vorticity fields obtained from the DPIVC movies do not show a clear pattern when it comes to the shedding frequency of the eddies downstream of the step. Indeed, though all of the experiments clearly showed that shedding was occurring, a consistent shedding frequency could not be calculated for all of them. This is probably due to the slow sampling rate (1/15 second) of the DPIVC system and to the turbulent nature of the flow.

It is interesting that all the cases where a shedding frequency could be discerned had a very similar shedding frequency (about 1.5-2.0 Hz). This odd result highlights the fact that more work needs to be done in improving the DPIVC system so that it can accurately track this phenomena.

6.2.9 Flow Rate Calculations

As was shown in the results section, the volume flow rates calculated from the ensemble averaged velocity fields have the same order of magnitude as the actual flow rates. However, the discrepancies between the calculated values and the actual values are surprisingly large (on the order of 15%-50%). These discrepancies (shown in Table 5.1) are interesting for two main reasons: first, all the calculated flow rates under-estimate the actual flow value, and second, the calculated flow rate is always lowest for the first axial section and is largest in the third axial section. These two facts suggest that the error in the calculation is due to some low velocity bias in the correlation algorithm. It is possible, for example, that the interrogation areas located in regions of high velocity gradients (i.e.: in the

central recirculation zone) find it easier to correlate the lower velocities than the higher velocities. This would then explain why the most downstream axial location, with its more uniform flow field and smaller velocity gradients, tends to show the highest flow rate.

6.3 Sources of Error in the results

Two main categories of error sources are present in the results reported in this thesis. The first category has to do with the swirl chamber itself, and the second category has to do with the DPIVC setup and analysis.

6.3.1 Sources of Error in the Swirl Chamber Setup

The errors caused by the swirl chamber apparatus have to do with the defining parameters of the flow: the Reynolds' number, the swirl number, and the jet velocity ratio. The Reynolds' number for the experiments reported here was calculated from a series of test runs in which the rate of change of the water level in the main tank was measured. Therefore, the estimate for the error in the Reynolds' number is based on an error analysis of all the parameters that were part of that calculation. These parameters were the volume change of the water in the main tank over the course of the calibration run (+-9%), the estimated error in the time measurement (+- 2%), and the uncertainty in the diameter of the acrylic test section (+-3%). All these error estimates result in a *Re* uncertainty of 18% for all the runs.

The swirl numbers reported in this thesis are based on the angle at which the swirl vanes were set. It is difficult to say the exact uncertainty present in the evaluation of this angle, but it is extremely unlikely that an error of more than 5 degrees averaged over all 32 vanes was ever encountered. This uncertainty translates into a worst case scenario error of +- 40% for the S=2.0 experiments and an error of +-18% for the S=0.5 experiments. It should be noted that this difference in the error bars is due to the $tan\phi$ term becoming extremely large as ϕ increases.

The uncertainty in the jet velocity ratio is based on the error in the secondary flow and on the uncertainty associated with the float meter used to measure the volume flow rate through the jet. This float meter was accurate to +- .05 gpm, which combined with the error in the secondary flow velocity, translates to a total error ranging from 19% to 26% in the value of the jet velocity ratio.

86

Finally, a systematic error might be introduced by a misalignment of the swirl chamber components. For instance, a slight misalignment of the converging nozzle and the test section tube might be the reason that the vorticity calculations consistently show higher circulations on the left side of the tube than on the right side of the tube. A slight misalignment in this part of the swirl chamber might also be responsible for some of the asymmetries discovered in the step induced vortex shedding. Finally, any misalignment of the primary jet and the test section could have a strong influence on the value of ϕ which would precipitate the azimuthal instability of the combined primary and secondary flows.

6.3.2 Sources of Error in the DPIVC Setup and Analysis

The sources of error in the DPIVC system can be divided into an optical error group and into a correlation error group. The errors in the optical setup of the data acquisition include possible misalignments between the camera's focal plane and the plane of the light sheet and possible misalignments between the light sheet plane and the axis of the tube. These factors are very difficult to measure, but it can be assumed that any misalignment is probably limited to +- 5 degrees.

The errors involved in the analysis and correlation of the particle images are more precisely quantifiable. One problem that became obvious during the course of these experiments is that particle displacements of about 5 pixels or more are very difficult to correlate. This can be noticed in the Re=11,000 , S=0.5 experiments, where the inlet zone of the flow shows many erroneous vectors and blank spaces. This is in contrast to the Re=35,000, S=0.5 experiments where the maximum displacements of 2 pixels allow this same region to be very well correlated. Since DPIVC's maximum displacement resolution is about 0.1 pixels, the small displacements which correlate well have an uncertainty of about 5-10% in their values, and this error is even larger for some of the very low velocity vectors which are encountered in the stagnant regions of the flow.

Since the vorticity field is calculated from the velocity field, the errors in the latter are transmitted to the former. The most egregious errors in the vorticity field occur when a grid point with a non correlated vector (whose value is therefore zero) is next to a high velocity vector. This situation obviously causes the local vorticity value to increase substantially. Fortunately, the velocity plots show that only the low Re flows (which have a longer pulse interval) and the flows with high velocity primary jets have any blank or erroneous vectors.

CHAPTER 7

Conclusions and Recommendations

7.1 Conclusions

The flow fields of jets confined to swirling flows having a Reynolds' number ranging from 10,000 to 36,000 and having a swirl number ranging from 0.5 to 2.0 have been investigated using DPIVC. Primary jet velocity ratios ranging from 0.0 to 20.0 have been examined for each of these Reynolds' and swirl number settings. The velocity field images which have been obtained using DPIVC display significant flow detail. Flow features such as the step induced eddies, the central recirculation zone, the oscillation of the jet flow about the axis and the reattachment point of the secondary flow to the tube walls can easily be seen in each frame. DPIVC has also allowed the temporal development of these features to be characterized.

7.1.1 Structure of the Recirculation Zones

The instantaneous two dimensional velocity and vorticity fields obtained from the experiments have been used to develop a three dimensional model of the vortex breakdowns. The basic flows (in which no primary jet is present) consist of a central recirculation zone (CRZ) located along the axis of the tube and of a step induced recirculation zone (SIRZ) located above the backward facing step. The presence of a large number of peaks in the vorticity isocontour plots and the strong correlation between the absolute values of circulation on either side of the axis indicate that both these recirculation zones are driven by a line of azimuthal vorticity spiraling up from the inlet of the test section, so that the overall flow structure can be described as a spiral within a spiral. The line of vorticity driving the CRZ has been found to be stronger and of opposite sign to that driving the SIRZ.

In the case of the CRZ, this spiral model contradicts the results of the laser Doppler anemometry (LDA) investigations reported in the literature. In fact, all previous investigations of turbulent swirling flows have concluded that the CRZ is driven by one closed toroid of azimuthal vorticity. In order to gain more insight into which of these two models is correct, a simulated LDA analysis has been performed on the instantaneous

88

velocity fields obtained in the present investigation. The results of this analysis also show the presence of a toroidal vorticity structure and strongly suggest that the averaging process in LDA reduces the number of vorticity peaks in the field by removing those peaks which move considerably from one frame to the next. This fact illuminates a major weakness of the LDA technique and emphatically supports the idea that the spiral model of the CRZ is correct.

7.1.2 Effect of the Secondary Flow's Swirl Number On the Breakdown

The effect of the secondary flow's swirl number on the breakdown structure can be seen by comparing the results of the basic flows in the first and second set of experiments (Re=34,000, S=2.0 and Re=35,000, S=0.5). Both these flows contain a CRZ driven by a spiral line of vorticity, but the recirculation zone in the S=2.0 case exists along the entire length of the axis while the CRZ in the S=0.5 case is limited to an axial extent of only 1.3 tube diameters. Since the spiral line of azimuthal vorticity is generated by the bending of the incoming axial vorticity, any increase in the strength of the latter (through an increase in the swirl number) will also increase the strength of the former. Therefore, the dramatic difference in the axial extent of the CRZs is due to the fact that the stronger line of azimuthal vorticity present in the high swirl case is more resistant to dissipation and persists farther downstream than the spiral line of vorticity present in the low swirl case.

The swirl number has also been shown to influence the reattachment point of the secondary flow to the tube walls. The lower centrifugal forces present in the low swirl cases cause the flow to reattach to the walls at a point further downstream of the inlet.

7.1.3 Effect of the Secondary Flow's Reynolds' Number On the Breakdown

It can be seen from the results of the second and third set of experiments (Re=35,000, S=0.5 and Re=10,000, S=0.5) that there is very little difference in the CRZ of the Re=35,000 flow and the Re=10,000 flow. This result suggests that the spiral model applies to a large range of turbulent swirling flows.

7.1.4 Effect of the Primary Jet on the Breakdown

The addition of a primary jet to the basic breakdown flow has revealed that the jet creates its own recirculation zone which has an opposite sign to that of the central recirculation zone. It has been found that the counter flow along the axis disappears when

the strength of these two zones becomes equal, and that the combination of the primary and secondary flows becomes unstable at high jet velocity ratios and begins to oscillate about the axis of the tube. The frequency of this oscillation has been measured to be very close to the solid body rotation frequency of the flow.

7.2 Recommendations for Future Work

The work presented in this thesis has clearly shown the benefits of using DPIVC to characterize swirling turbulent flows. The general features of the flow have been described, and a new model for the structure of the central recirculation zone has been proposed. Future experiments should concentrate on examining the structure of the CRZ in more detail. Higher resolution images of this region should be recorded by running experiments in which the camera's field of view is limited to the CRZ.

Experiments should also be performed on laminar swirling flows to emulate the conditions investigated by Leibovich and Brücker et. al. These researchers (who used LDA and particle tracking velocimetry techniques) concluded that the bubble type recirculation zone is driven by one or two toroids of vorticity, and it would be interesting to see if a different kind of flow structure is revealed by the use of DPIVC.

Further attempts should be made to record images of azimuthal cross sections of the flow. The particle seeding density in future experiments should be reduced from the levels used in the present ones so as to improve the optical clarity of the images.

Finally, there is room to make structural improvements to the swirl apparatus itself. A new flow rate measurement technique should be used to measure the secondary flow, since the present 18% error is too large to make a very detailed investigation of the *Re* parameter space. An improvement in the swirl vane alignment should also be made if a detailed investigation of higher swirl numbers is to be performed.

References

[1]   Takagi, T., and Okamoto, T., 1981, "Characteristics of Combustion and Pollutant Formation in Swirling Flames," *Comb. and Flame,* Vol. 43, pp. 69-79.

[2]   Gupta A.K., Ramavajjala M., and Taha M.R., 1992, "The Effect of Swirl and Nozzle Geometry on the Structure of Flames and NOx Emission," *AIAA 30th Aerospace Sciences Meeting.*

[3]   Peckham, D.H., and Atkinson, S.A., 1957, "Preliminary Results of Low Speed Wind Tunnel Tests on a Gothic Wing of Aspect Ratio 1.0," *British Aeronaut. Res. Council,* CP 508.

[4]   Althaus, W., Brücker, CH., and Weimer, M., "Breakdown of Slender Vortices", from *Fluid Vortices,* 1995, Kluwer Academic Publishers, Dordrecht, The Netherlands,   pp. 373-426

[5]   Harvey, J.K., 1962, "Some Observations of the Vortex Breakdown Phenomena," *J. Fluid Mech.,* Vol. 14, pp. 585.

[6]   Brown, G.L., and Lopez, J.M., 1990, "Axisymmetric Vortex Breakdown. Part 2. Physical Mechanisms", *J. Fluid Mech.,* Vol. 221, pp. 553

[7]   Sarpkaya, T., 1971, "On Stationary and Travelling Vortex Breakdowns," *J. Fluid Mech.,* Vol. 45, part 3, pp. 545-559.

[8]   Sarpkaya, T., 1974, "Effect of the Adverse Pressure Gradient on Vortex Breakdown", *AIAA J.,* 12, pp. 602.

[9]   Faler, J.H., and Leibovich, S., 1978, "An Experimental map of the Internal Structure of a Vortex Breakdown," *J. Fluid Mech.,* Vol. 86, pp. 313

[10]   Brücker, Ch. and Althaus, W., 1992, "Study of vortex breakdown by particle tracking velocimetry (PTV). Part 1: Bubble-type vortex breakdown," *Exp. Fluids,* Vol. 13, pp. 339-349.

[11]   Habib, M.A., and Whitelaw, J.H., 1980, "Velocity Characteristics of Confined Coaxial Jets With and Without Swirl," *Journal of Fluids Engr.,* Vol.102, pp.47-53.

[12]   Vu, B.T., and Gouldin, F.C., 1982, "Flow Measurements in a Model Swirl Combustor", *AIAA J.,* Vol. 20, NO. 5, pp. 642-651.

[13]   Gouldin, F.C., Depsky, J.S., and Lee, S-L., "Velocity Field Characteristics of a Swirling Flow Combustor," *AIAA Journal,* Vol. 23, NO. 1, pp. 95-102.

[14]   Ramos, J.I., and Somer, H.T., 1985, "Swirling Flow in a Research Combustor," *AIAA Journal,* Vol. 23, NO. 2, pp. 241-248.

[15]   So, R.M.C., Ahmed, S.A., and Mongia, H.C., 1985, "Jet Characteristics in Confined Swirling Flow", *Exp. Fluids*, Vol. 3, pp.221-230,

[16]   Grabowski, W.J., and Berger, S.A., 1967, "Solutions of the Navier-Stokes Equations for Vortex Breakdown", *J. Fluid Mech.*, Vol. 75, pp. 525-544.

[17]   Spall, R.E., and Gatski, T.B., 1987, "A Numerical Simulation of Vortex Breakdown", *ASME Forum on Unsteady Flow Separation*, FED 52, 25-33.

[18]   Breuer, M., and Hänel, D., 1989, "Solution of the 3-D Incompressible Navier-Stokes Equations for the Simulation of Vortex Breakdown", *Proc. of the 8th GAMMM-Conf. on Numerical Methods in Fluid Mechanics.*

[19]   Spall, R.E., Gatski, T.B., and Ash, R.L., 1990, "The Structure and Dynamics of Bubble-Type Vortex Breakdown", *Proc. R. Soc. Lond.* A.429, 613-637

[20]   Haynes, J.M., 1990, "Aerodynamic Design of Low NOx Oil Diffusion Flames Using the Radially Stratified Flame Core Burner", Ph.D. Thesis, Massachusetts Institute of Technology.

[21]   Adrian, R.J., 1991, "Particle-Imaging Techniques for Experimental Fluid Mechanics", *Annu. Rev. Fluid Mech.* 23: pp. 261-304.

[22]   Willert, C.E., and Gharib, M., 1991, "Digital Particle Image Velocimetry", *Experiments in Fluids*, Vol. 10, pp. 181-193

[23]   Danitz, D.J., 1995, "Experimental Investigation of the Mixing of an Axial Jet Within a Swirling Flow, Utilizing Laser Doppler Velocimetry and Particle Image Velocimetry", Masters Thesis, Massachusetts Institute of Technology.

[24]   Faler, J.H., 1976, "Some Experiments in Swirling Flows: Detailed Velocity Measurements of a Vortex Breakdown Using a Laser Doppler Anemometer", Ph.D. Thesis, Cornell University.

[25]   Marzouk, Y., 1997, "High-Speed Particle Image Velocimetry Correlation for Unsteady and Time-Dependent Flows", B.S. Thesis, Massachusetts Institute of Technology

[26]   Hart, D., 1996, "Example of Sparse Array Image Autocorrelation", unpublished, Massachusetts Institute of Technology.

[27]   Crowe, C.T., Troutt, T.R., and Chung, J.N., "Particle Interactions", from *Fluid Vortices*, 1995, Kluwer Academic Publishers, Dordrecht, The Netherlands, pp. 829-861.

[28]   Frish, M.B., and Webb, W.W., 1981, "Direct Measurement of Vorticity by Optical Probe", *J. Fluid Mech.*, Vol. 107, pp.173-200
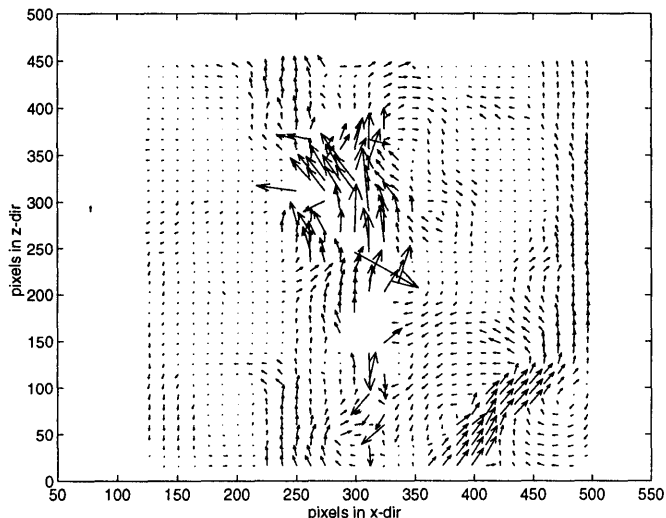
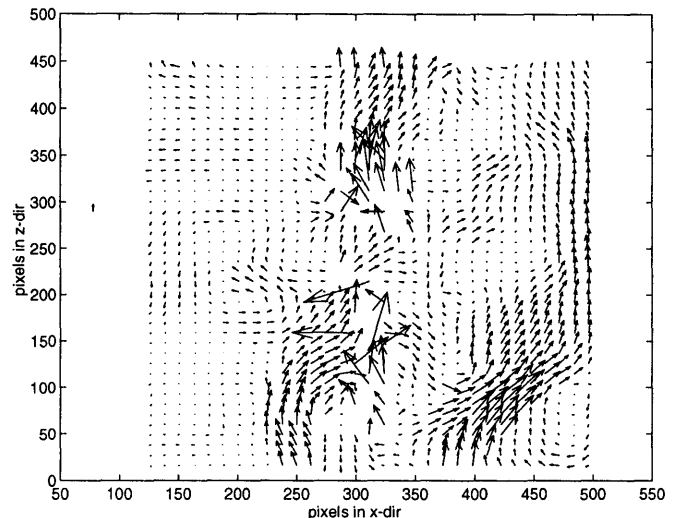# Appendix A
DPIVC Frame Sequences
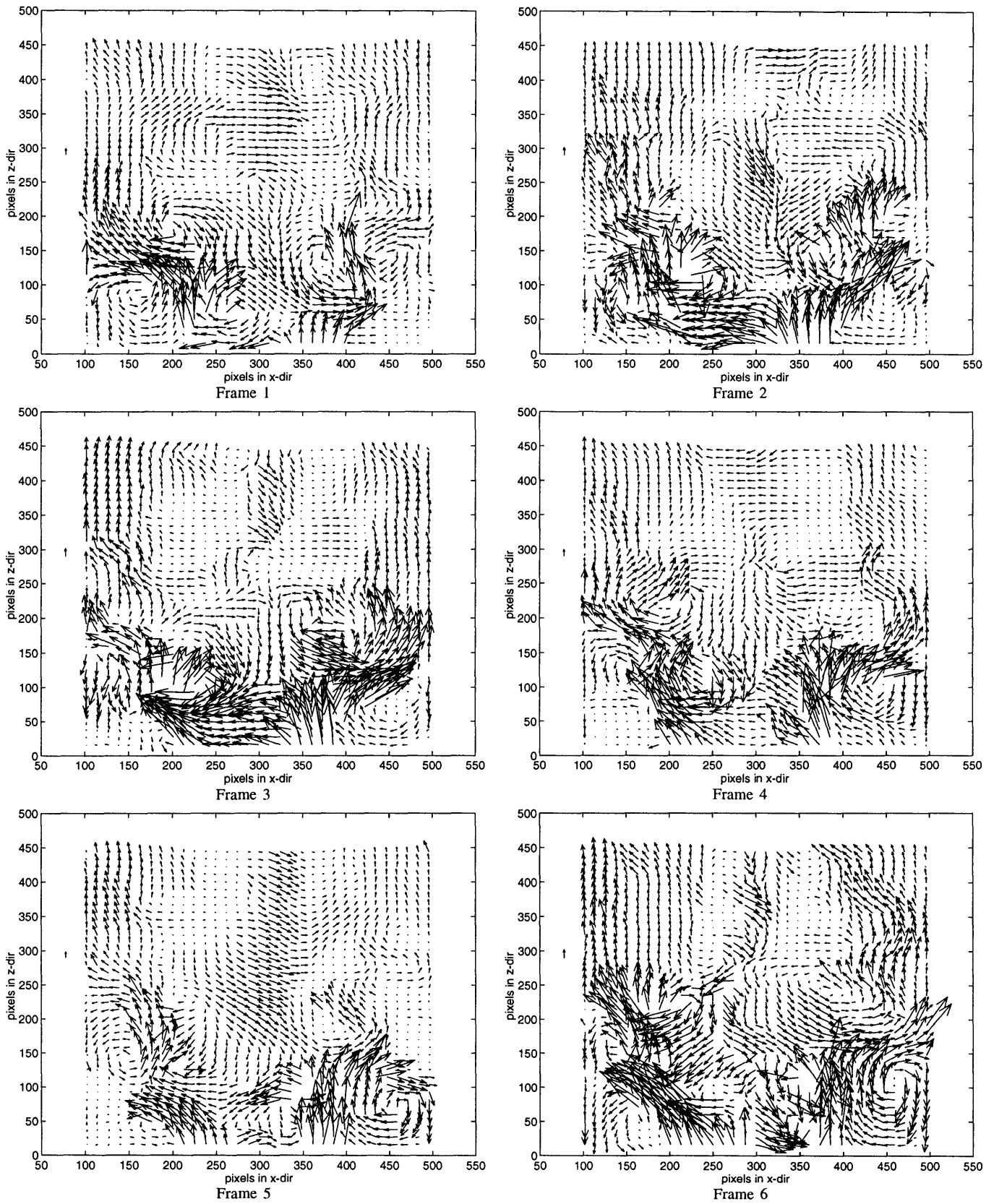
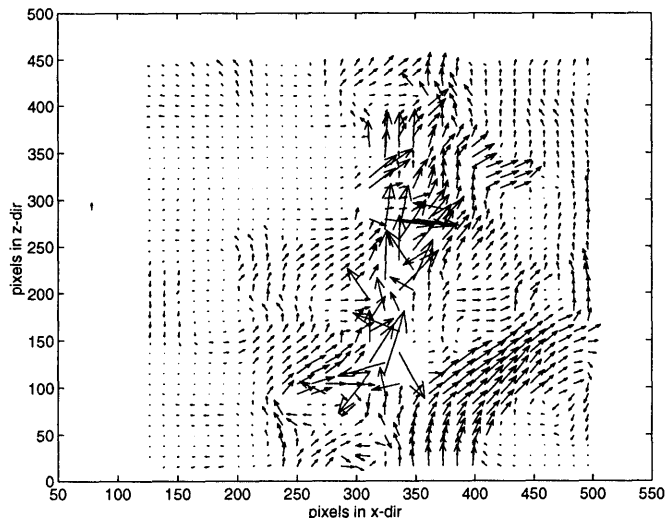**Figure A1.** Frame Sequence from DPIVC Movie of $Re=34,000$, $S=2.0$, $\phi=0.0$ Case.

94

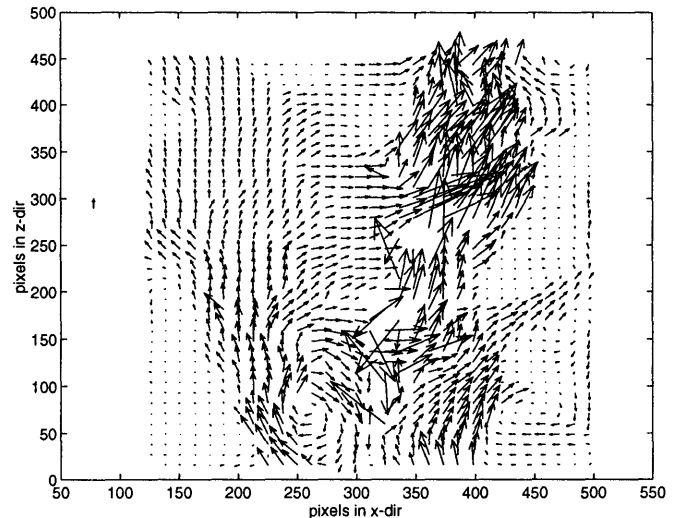**Figure A1.** Frame Sequence From DPIVC Movie of *Re=34,000*, *S=2.0*, *φ=0.0* Case (*Continued*).

95

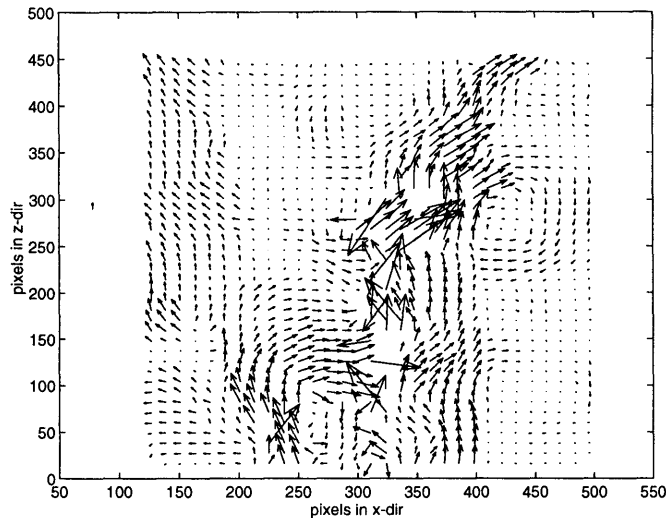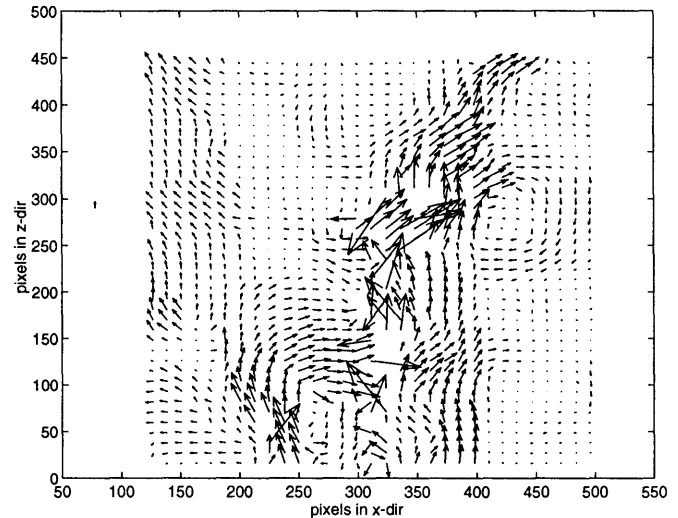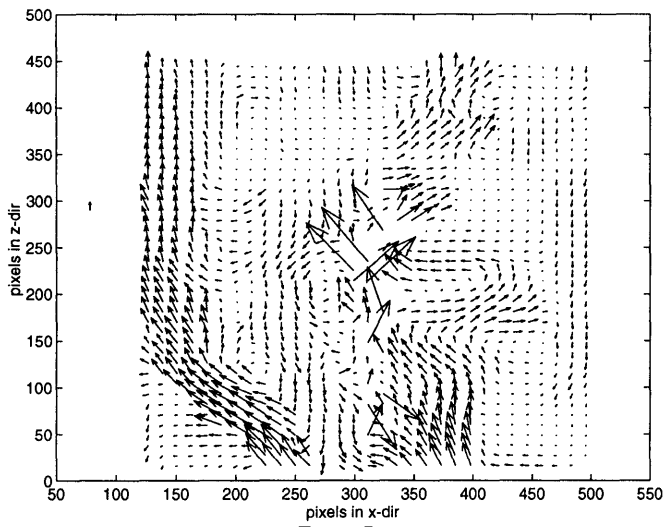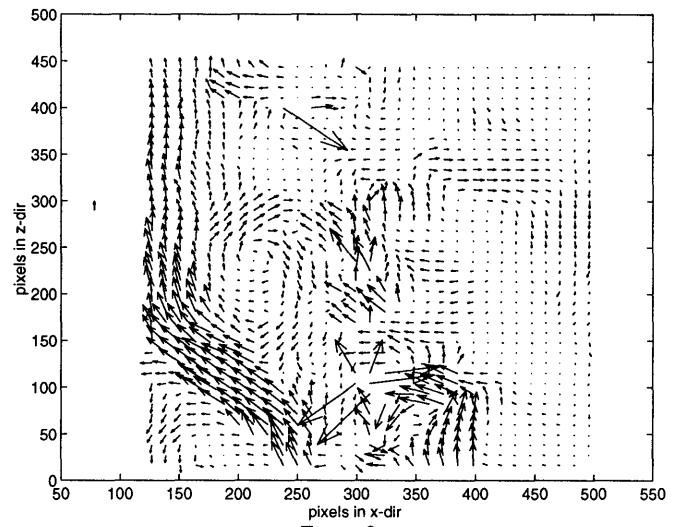**Figure A2.** Frame Sequence From DPIVC Movie of *Re=34,000*, *S=2.0 φ=20.0* Case.

96

Figure A2. Frame Sequence From DPIVC Movie of *Re=34,000*, *S=2.0, φ=20.0* Case (*Continued*).

97
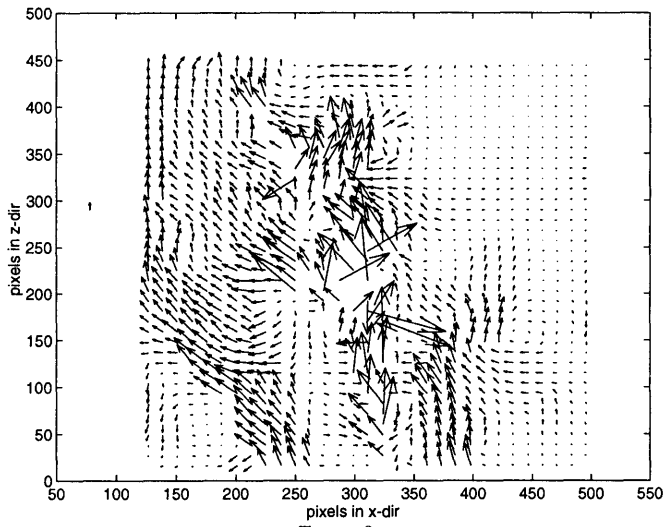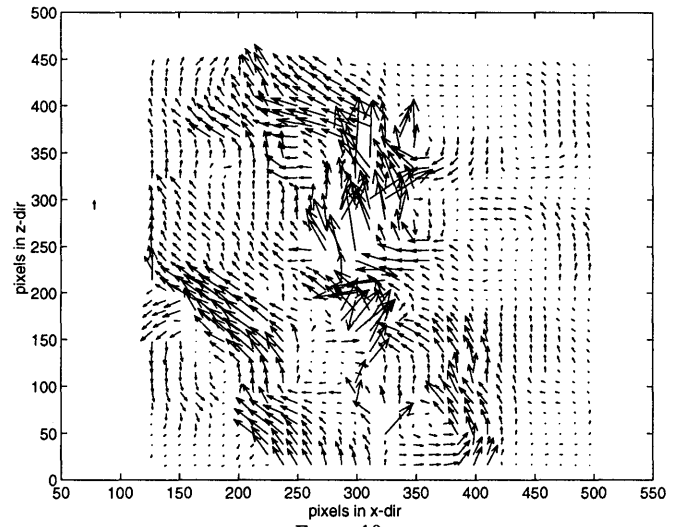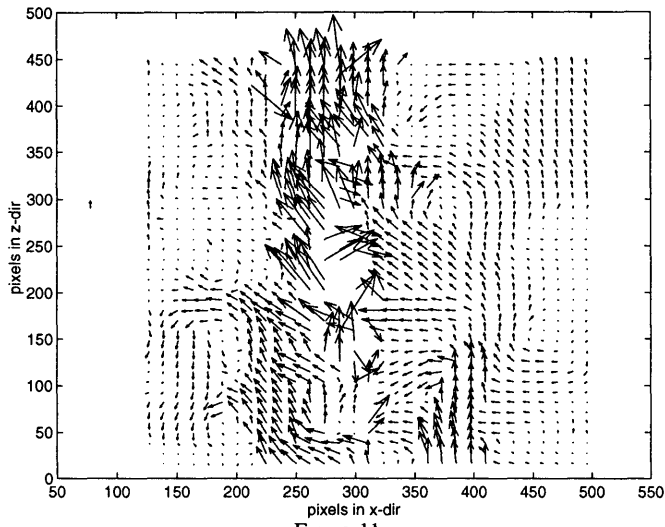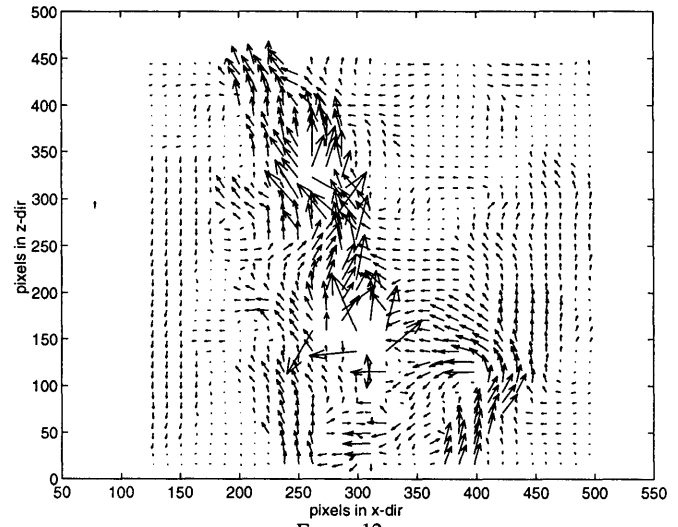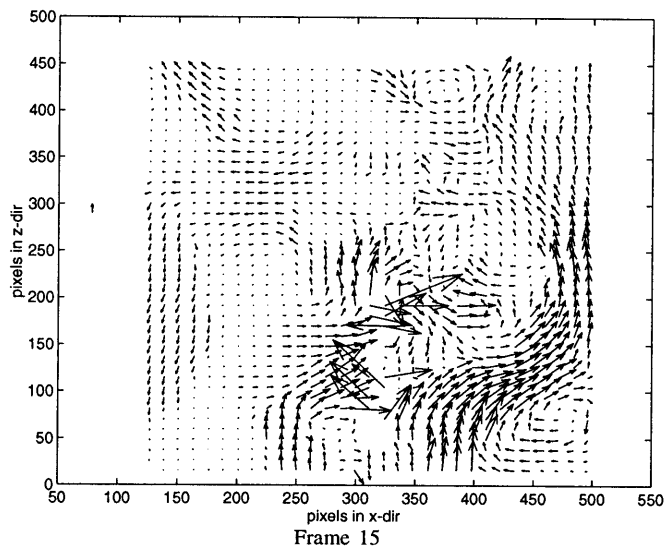
Figure A2. Frame Sequence From DPIVC Movie of *Re=34,000*, *S=2.0, φ=20.0* Case (*Continued*).

Figure A3. Frame Sequence From DPIVC Movie of *Re=35,000,*
S=0.5, φ=11.6 Case.

99
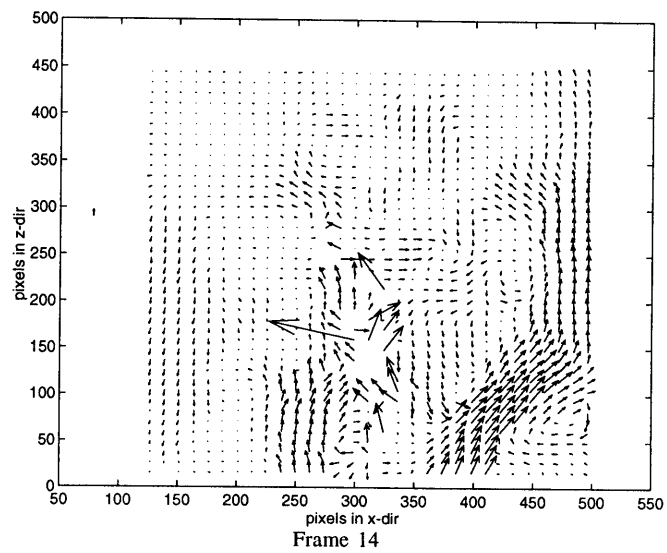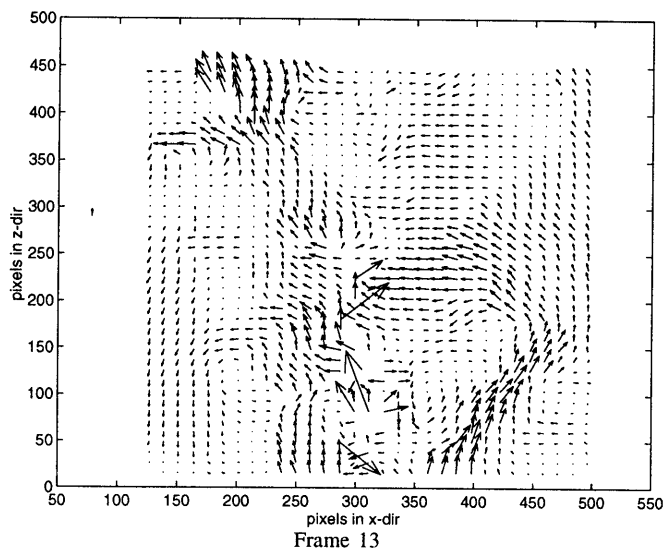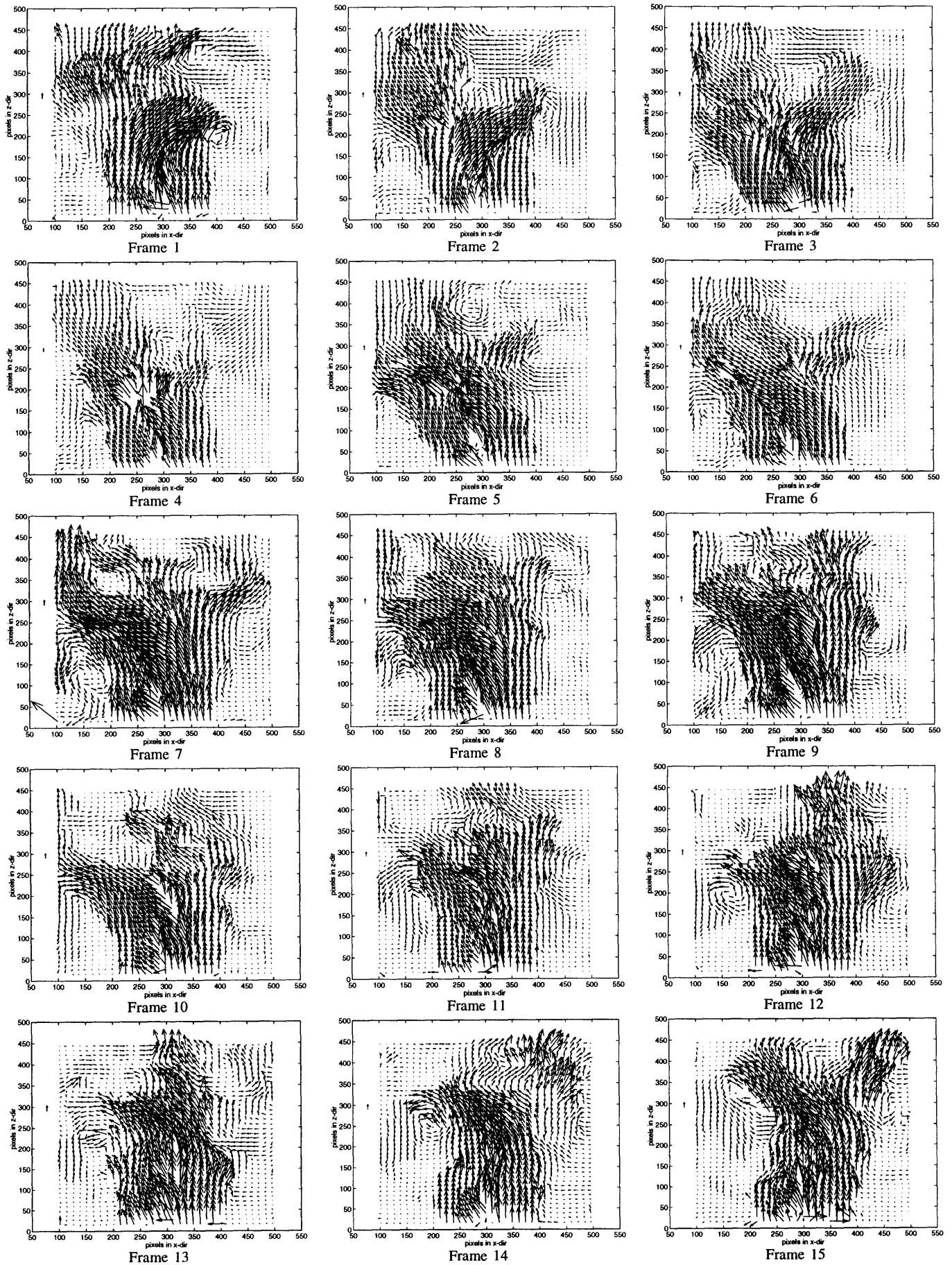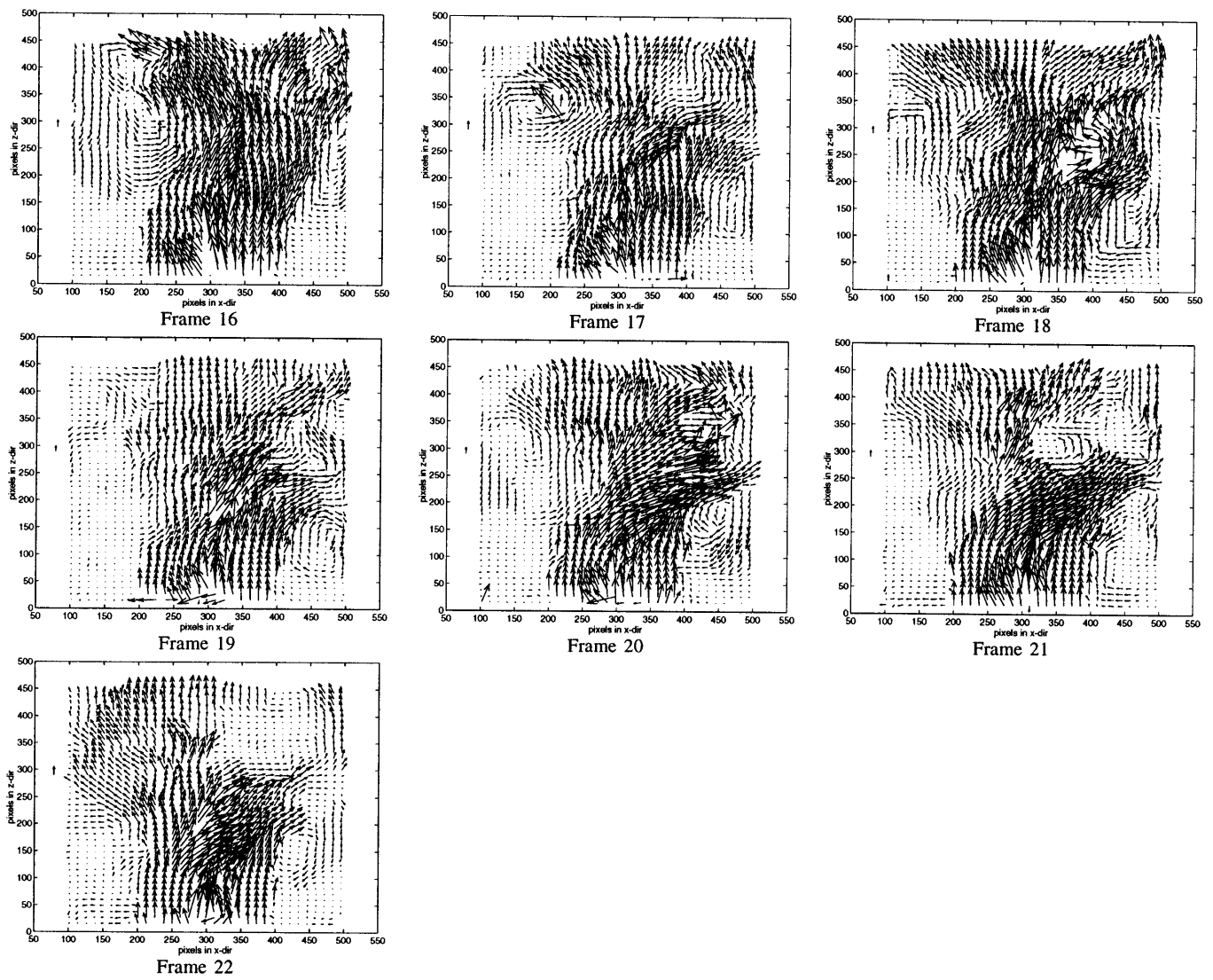
Frame 16

Frame 17

Frame 18

Frame 19

Frame 20

Frame 21

Frame 22

Figure A3. Frame Sequence From DPIVC Movie of *Re=35,000,*
S=0.5, φ=11.6 Case (*Continued*)

100

APPENDIX B

Tabulated Circulation Calculations

This appendix presents the results of the azimuthal circulation calculations performed on the vorticity fields investigated in this thesis. The azimuthal circulation of a given area is calculated by first finding the average positive and negative vorticities of that area; these vorticities are then multiplied by the given area to give that region's positive and negative components of azimuthal circulation.

The positive and negative azimuthal circulations are calculated over three distinct areas: the left side of the image, the right side of the image, and the complete image. The reasoning behind this can be seen in Figure B.1, which illustrates the flow model developed in Chapter 5. This figure shows that the left side's positive circulation and the right side's negative circulation correspond to the step induced recirculation zone (SIRZ), and that the left side's negative circulation and the right side's positive circulation correspond to the central recirculation zone (CRZ). The calculation of the circulation over the entire area of the image is performed to make sure that the net azimuthal circulation is zero.
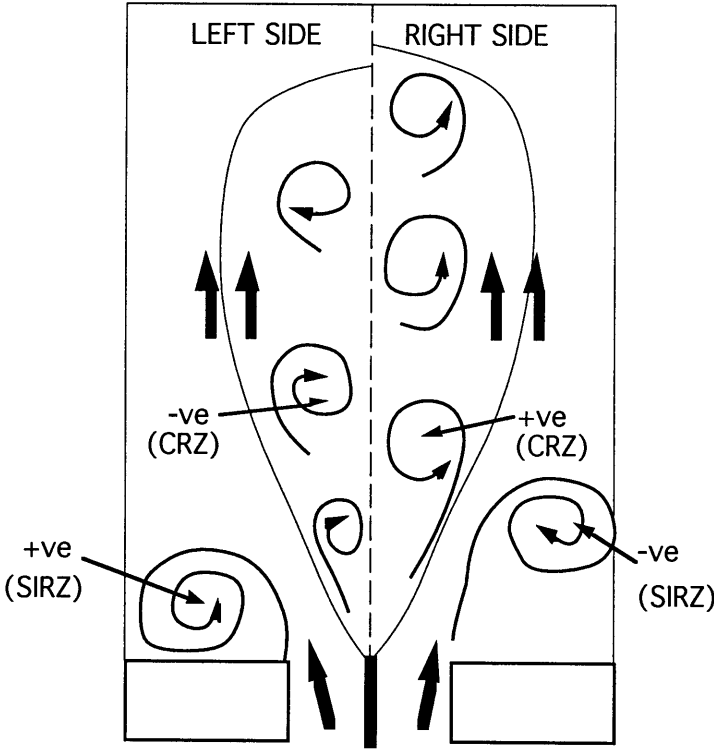
Figure B.1. Illustration of Flow Model.

The tabulated values of the azimuthal circualtions are presented in the following pages. *(NB: Section 1 refers to a region spanning from the inlet to a distance 1.1D downstream of it; Section 2 refers to a region spanning from 0.9D to 2.0D downstream of the inlet; Section 3 refers to a region spanning from 1.9D to 3.0D downstream of the inlet)*

Re=34,000, S=2.0 ϕ=0.0	TOTAL Positive (m²/s x10³)	TOTAL Negative (m²/s x10³)	LEFT SIDE Positive (m²/s x10³)	LEFT SIDE Negative (m²/s x10³)	RIGHT SIDE Positive (m²/s x10³)	RIGHT SIDE Negative (m²/s x10³)
Section 1	275	-288	126	-177	149	-112
Section 2	116	-129	40.0	-106	76.2	-22.9
Section 3	118	112	44.2	-79.0	73.5	-32.6

Table B.1. Circulation for *Re=34,000, S=2.0, ϕ=0.0*

Re=34,000, S=2.0 ϕ=4.0	TOTAL Positive (m²/s x10³)	TOTAL Negative (m²/s x10³)	LEFT SIDE Positive (m²/s x10³)	LEFT SIDE Negative (m²/s x10³)	RIGHT SIDE Positive (m²/s x10³)	RIGHT SIDE Negative (m²/s x10³)
Section 1	212	-221	90.5	-133	121	-88.4
Section 2	95.7	-87.4	34.5	-70.1	61.2	-17.4
Section 3	71.4	-82.0	15.9	-64.2	55.4	-17.7

Table B.2. Circulation for *Re=34,000, S=2.0, ϕ=4.0*

Re=34,000, S=2.0 ϕ=12.0	TOTAL Positive (m²/s x10³)	TOTAL Negative (m²/s x10³)	LEFT SIDE Positive (m²/s x10³)	LEFT SIDE Negative (m²/s x10³)	RIGHT SIDE Positive (m²/s x10³)	RIGHT SIDE Negative (m²/s x10³)
Section 1	218	-229	123	-120	94.4	-109
Section 2	85.2	-80.3	47.0	-47.6	38.2	-32.8
Section 3	55.6	-59.8	21.6	-38.2	34.0	-21.5

Table B.3. Circulation for *Re*=34,000, *S*=2.0, ϕ=12.0

Re=34,000, S=2.0 φ=20.0	TOTAL Positive (m²/s x10³)	TOTAL Negative (m²/s x10³)	LEFT SIDE Positive (m²/s x10³)	LEFT SIDE Negative (m²/s x10³)	RIGHT SIDE Positive (m²/s x10³)	RIGHT SIDE Negative (m²/s x10³)
Section 1	243	-253	151	-135	93	-119
Section 2	140	-140	80.0	-78.2	60.3	-61.2
Section 3	91.3	-93.7	45.2	-53.6	46.0	-40.2

Table B.4. Circulation for Re=34,000, S=2.0, φ=20.0

Re=35,000, S=0.5 φ=0.0	TOTAL Positive (m²/s x10³)	TOTAL Negative (m²/s x10³)	LEFT SIDE Positive (m²/s x10³)	LEFT SIDE Negative (m²/s x10³)	RIGHT SIDE Positive (m²/s x10³)	RIGHT SIDE Negative (m²/s x10³)
Section 1	267	-252	128	-147	139	-105
Section 2	125	-120	51.3	-88.9	73.4	-31.4
Section 3	79.4	-75.4	39.4	-55.6	40.0	-19.8

Table B.5. Circulation for Re=35,000, S=0.5, φ=0.0

Re=35,000, S=0.5 φ=3.9	TOTAL Positive (m²/s x10³)	TOTAL Negative (m²/s x10³)	LEFT SIDE Positive (m²/s x10³)	LEFT SIDE Negative (m²/s x10³)	RIGHT SIDE Positive (m²/s x10³)	RIGHT SIDE Negative (m²/s x10³)
Section 1	263	-250	130	-156	133	-94.5
Section 2	128	-117	53.2	-90.0	74.6	-26.6
Section 3	77.2	-89.5	28.5	-68.0	48.7	-21.6

Table B.6. Circulation for Re=35,000, S=0.5, φ=3.9

Re=35,000, S=0.5 φ=11.6	TOTAL Positive (m²/s x10³)	TOTAL Negative (m²/s x10³)	LEFT SIDE Positive (m²/s x10³)	LEFT SIDE Negative (m²/s x10³)	RIGHT SIDE Positive (m²/s x10³)	RIGHT SIDE Negative (m²/s x10³)
Section 1	205	-212	158	-64.9	48.0	-147
Section 2	145	-166	85.2	-92.2	60.0	-73.8
Section 3	122	-102	61.6	-60.9	60.4	-41.8

Table B.7. Circulation for Re=35,000, S=0.5, φ=11.6

Re=35,000, S=0.5 φ=19.3	TOTAL Positive (m²/s x10³)	TOTAL Negative (m²/s x10³)	LEFT SIDE Positive (m²/s x10³)	LEFT SIDE Negative (m²/s x10³)	RIGHT SIDE Positive (m²/s x10³)	RIGHT SIDE Negative (m²/s x10³)
Section 1	229	-233	174	-94.5	55.4	-139
Section 2	188	-203	122	-102	66.7	-101.2
Section 3	165	-131	75.7	-81.9	89.3	-48.6

Table B.8. Circulation for Re=35,000, S=0.5, φ=19.3

Re=11,000, S=0.5 φ=0.0	TOTAL Positive (m²/s x10³)	TOTAL Negative (m²/s x10³)	LEFT SIDE Positive (m²/s x10³)	LEFT SIDE Negative (m²/s x10³)	RIGHT SIDE Positive (m²/s x10³)	RIGHT SIDE Negative (m²/s x10³)
Section 1	80.6	-75.6	38.9	-45.5	41.6	-30.0
Section 2	33.3	-32.5	13.5	-23.6	19.9	-8.95
Section 3	17.9	-20.2	7.97	-14.1	9.88	-6.08

Table B.9. Circulation for Re=11,000, S=0.5, φ=0.0

Re=11,000, *S*=0.5 ϕ=8.6	TOTAL Positive (m²/s x10³)	TOTAL Negative (m²/s x10³)	LEFT SIDE Positive (m²/s x10³)	LEFT SIDE Negative (m²/s x10³)	RIGHT SIDE Positive (m²/s x10³)	RIGHT SIDE Negative (m²/s x10³)
Section 1	66.7	-71.1	47.7	-21.6	19.0	-49.5
Section 2	53.8	-39.0	28.7	-20.9	25.1	-18.2
Section 3	32.4	-31.3	19.3	-18.3	13.0	-13.0

Table B.10. Circulation for *Re*=11,000, *S*=0.5, ϕ=8.6